A Sensitivity Analysis Approach to Identifying Drivers of Streamflow Hysteresis

E. House[1], E. Meselhe[1], M. Muste[2], K. Kim[2], and I. Demir[1]

[1] River Coastal Science and Engineering, Tulane University, New Orleans, Louisiana, USA. 6823 St Charles Ave, New Orleans, LA 70118, U.S.A., ehouse@tulane.edu, emeselhe@tulane.edu, idemir@tulane.edu.

[2] IIHR-Hydroscience and Engineering, University of Iowa, Iowa City, Iowa, USA. University of Iowa: IIHR-Hydroscience & Engineering, C. Maxwell Stanley Hydraulics Laboratory, Iowa City, IA 52245, U.S.A., marian-muste@uiowa.edu, kyeongdong-kim@uiowa.edu.

Corresponding Author: Emma House ehouse@tulane.edu

This manuscript is an EarthArXiv preprint whichhas been submitted for publication in JOURNAL OF THE AMERICAN WATER RESOURCES ASSOCIATION. Please note that, despite having undergone peer-review, the manuscript has yet to be formally accepted for publication. Subsequent versions of this manuscript may have slightly different content. If accepted, the final version of this manuscript will be available via the 'Peer-reviewed Publication DOI' link on the right-hand side of this webpage. Please feel free to contact the corresponding author; we welcome feedback.

Abstract

We study the critical interplay between streamflow hysteresis and local hydro-morphologic conditions. Hysteresis strength, which can lead to over 60% errors in discharge estimation with widely accepted monitoring methods, is primarily influenced by local characteristics such as bed slope, roughness, and event wave intensity. Our study used a 1D numerical model to highlight the hysteresis response to local hydro-morphological changes acting in isolation or combination. The sensitivity study entails gradual variation of the hydrograph intensity, backwater condition, bed slope ($0.0001<S_0<0.0001$), and Manning's roughness ($0.02<n<0.2$) in simple and compound channels. A statistical analysis revealed hysteresis is controlled 28% by hydrograph intensity, 23% bed slope, 16% roughness, and 15% backwater condition. In examining all permutations, we found that the bed slope dominates other parameters as the most persistent control on the expression of hysteresis, with mild bed slopes consistently generating strong hysteresis signals. Finally, we demonstrate how upstream discharge boundary conditions that account for hysteresis produce a realistic response in the modeled reach compared to those provided by conventional methods like the stage-discharge rating. In understanding the sensitivity of streamflow hysteresis to its drivers, we narrow the gap between our evolving knowledge of flow dynamics and strategies for monitoring, modeling, and forecasting rivers under unsteady conditions.

1. Introduction

Hysteretic conditions, which present a non-unique relationship between flow variables throughout the cycle of a flood event, are present in the unsteady flow regime of 67% of rivers gaged by the United States Geological Survey (USGS; Holmes, 2016). Therefore, river monitors must use caution when making river management decisions based on discharge such as the operation of reservoirs and flood structures. The differences in flow variables between the rising and falling phases of a flood wave have a strong impact on the flux of particulate and dissolved components of rivers, so hysteresis must be considered in sediment budget and water quality applications as well, or risk significant errors in crucial morphological and environmental health decisions. Hysteresis effects have been known to cause up to 65% error in measurement with traditional rating curve techniques (namely the steady-flow-based stage-discharge relationship HQRC, Muste et al., 2022b). This significant impact is acknowledged in monitoring practice as epistemic uncertainties even though they can well exceed the accepted 5% error threshold (Schmidt, 2002; Baldassarre & Montanari, 2009). More advanced, yet still relatively simple to implement in today's age of technology, discharge estimation methods have been developed but are not yet widely accepted or implemented (Rantz et al., 1982; Fenton, 2001; Schmidt & Garcia, 2003; Cheng et al., 2019; Lee et al., 2017; Muste et al., 2022a). It is imperative that water resource monitors are aware of the significance of hysteresis, under which conditions it develops, and how it may be accurately estimated and modeled. The significance and worldwide prevalence of the stage-discharge rating curve that overlooks hysteresis justifies the need to further investigate the drivers of this intricate and understudied dynamic process.

Key characteristics of hysteresis have been noted in the literature for hundreds of years, starting with the ahead-of-its-time Hungarian study in the 1800s (Rátky, 2000). Researchers have provided evidence to solidify findings that hold true for the streamflow hysteresis phenomenon, particularly differences between the rising and falling limbs of a river flood wave (Faye and

Cherry, 1980; Fread, 1975; Dottori et al., 2009; Mishra & Singh, 1999; Muste et al., 2019). Hysteresis is associated with low Froude numbers, or gravity driven subcritical flows (Muste et al., 2024). Despite the strong motivational evidence, observational endeavors are limited by monitoring resources and time, so researchers often turn to numerical methods for in-depth exploration of complex physical processes.

If a river station exhibits hysteresis, that does not imply that the entire river can be classified as hysteretic. Nor if a given flood event at a station exhibits hysteresis, the entire period of record of flood events at that station will be hysteretic. So, what determines if the flow will be hysteretic or not (Muste et al., 2025b)? Diagnostic formulas are used in the context of streamflow hysteresis to assess a river monitoring station for the degree of hysteresis strength (Dottori et al., 2009; Lee, 2013; Zuecco et al., 2016; Muste et al., 2020a). These formulas are often based on channel and flow characteristics and provide a guide as to which type of flow is expected, and thus the appropriate monitoring method. For example, in the Fread diagnostic, monitoring locations with $S_o < 0.0001$ and $dh/dt > 0.015$ m/h are classified as significantly hysteretic-prone and should use dynamic-based discharge estimation techniques such as the Index-Velocity Rating Curve (IVRC) and Continuous Slope Area (CSA) methods (Fread, 1975). The sensitivity analysis applied herein is supportive of the diagnostic formula approach as we investigated the ranges of important channel and flow characteristics under which hysteresis can develop. In identifying and characterizing the dominant physical drivers of streamflow hysteresis through a series of idealized simulations and momentum-based analyses, the broader significance of this study lies in its potential to inform more accurate and physics-based discharge monitoring strategies. This study offers a robust framework for understanding the interactions between channel and flow variables that drive hysteretic behavior.

1.1. Manifestation of Fluvial Hysteresis

During the hysteretic cycle, flow variables and underlying momentum terms in the St. Venant equation (Supplementary Eq. 2) exhibit a looped relationship and peak-phasing, and waves are classified as diffusive or dynamic with active pressure gradient and convective acceleration forces (House et al., 2025a). As shown by numerical methods (Figure 1), there is a loop shape in the relationship between flow variables, Froude number, and momentum terms throughout the hysteretic cycle during a flood wave or seasonal vegetation growth (Muste et al., 2020a; House et al., 2025a). Accordingly, there is a peak-phasing effect where the lag between peaks increases with the strengthening of hysteretic severity.

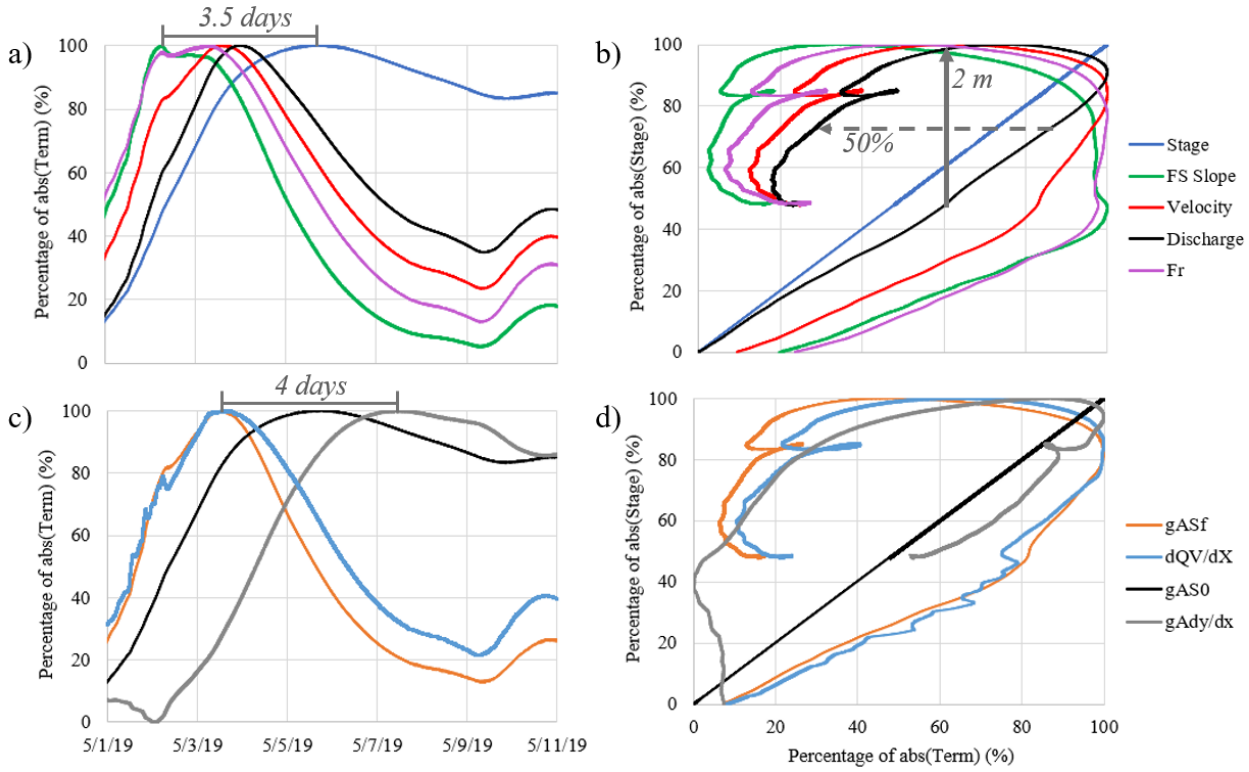

Figure 1: *The characteristics of hysteretic streamflow from numerical simulations of the Illinois River flow at Henry, IL #05558300: a) the "lag" peak-phasing effect of streamflow variables and Froude number, b) the "loop" shape of the stage-streamflow variable and Froude number relationships, c) the "lag" peak-phasing effect of momentum forces, and d) the "loop" shape of the stage-momentum force relationships.*

In Figure 1, panels a-b, the rising and falling limbs of the stage hydrograph show the approximately 3.5-day lag between peaks of free-surface slope and stage, 50% decrease in flow for a given stage (dashed arrow), and 2-meter increase in stage for a given flow (plain arrow), between the rising and recession limbs of the stage-discharge loop in black. In c-d), a 4-day lag between peaks of friction slope/convective acceleration and pressure gradient is observed, with significantly large loops for several non-kinematic forces.

1.2. Drivers of Fluvial Hysteresis

Hysteresis is known to be caused by the rate of change of discharge or variable backwater (i.e., unsteady flow or storage occurring in the stream reach, respectively; Henderson, 1966; Rantz et al, 1982; Fenton & Keller, 2001; Muste et al., 2020a). Friction is important for all flow conditions, but pressure gradient and inertia terms are significant only under certain conditions (Meselhe et al., 2021). Kinematic waves do not typically develop hysteresis (Arico et al., 2009; House et al., 2025a). Understanding under what physical conditions hysteresis is likely to occur is the next logical step to enhancing monitoring protocol. Several studies give insight into what we may observe when we vary the flow and channel attributes for a naturally hysteretic flow condition. One of the most remarked qualities of a hysteretic river from the literature is a relatively low *channel bed slope* (Holmes, 2016; Muste et al., 2020a). Mishra & Singh (1999) suggest that reducing the channel bed slope has the greatest impact on hysteresis, quantifying this with the area of the hysteresis loop. Channel bed slopes that are steeper tend to convey gravity-driven flow,

while gentler bed slopes are more friction dominated, allowing for hysteresis to develop. In a similar numerical modeling study of two contrasting locations using observed data, a non-hysteretic site with a bed slope of 0.002 and strong hysteresis site has a bed slope of 0.00027, supporting this point (House et al., 2025a). A second parameter which may impact the hysteresis signal is the *channel roughness* which varies in vegetated streams throughout the year. Muste et al. (2020a) note that hysteresis is a process dominated by friction (or channel control). Their study estimates Manning's roughness changing from 0.02 to 0.035 from April to July due to riparian vegetation growth (Figure 2), a range which is included in the sensitivity analysis in Table 1 to support this study. Heldmyer et al. (2022) utilized numerical methods to focus on channel parameterization and highlighted roughness as a major factor in the National Water Model providing further motivation to explore its impacts with streamflow hysteresis. Finally, in a study by Crago et al. (2000), flow and roughness conditions are varied in a numerical model, and the wave is seen to attenuate with increasing non-kinematic effects.

Figure 2: *Riparian vegetation height for a Manning's roughness study of Clear Creek, IA #05454220 with fixed cameras: a) webcam views of the site.*

The *flood wave's severity* (intensity vs. duration) has also been described as a driver of the hysteresis signal within that flood wave. More intense precipitation events (short duration, large magnitude hydrographs) have been observed to exhibit strong hysteresis, with high flows during the rising limb and slower flows during the falling limb for a given stage (Muste et al., 2020a). Larger hysteresis loops are noted in several studies to pertain to larger flood wave attenuation and diffusive forces (Henderson, 1966; Mishra & Singh, 1999). Similarly, in a sensitivity analysis, event duration and peak discharge timing are noted as contributing parameters (Lee et al., 2012). More dynamic waves exhibit more hysteresis as they are located in areas of great energy loss, according to Mishra & Singh (1999). *Backwater effect* at a monitoring station is known to cause hysteresis, since according to Holmes (2016), 65% of the gaging stations in the United States are known to be located in areas of extensive backwater and exhibit hysteresis (Fenton & Keller, 2001; Holmes, 2016). Backwater effects can be caused by downstream structures, lakes, or changes in channel bed slope, shape, or roughness (Henderson, 1966). Similarly, the profile and cross-section *channel shape* may have hysteretic implications since they modify the river flow over space.

This study aims to examine the implications of practical discharge estimation techniques for hydraulic modeling. To do so, different *discharge (Q) estimation methods* are employed as boundary conditions of a model for testing hysteresis sensitivity. The goal is also to explore how

the imposed discharge propagates through the reach. If an HQRC-estimated discharge which is inherently kinematic/uniform is imposed, what is the resulting behavior in the modeled reach, and will hysteresis develop? Similarly, for the *normal depth (ND)* scenarios, what are the implications of using ND at the downstream hydraulic boundary, a standard practice by many modelers. Muste et al. (2020a) discuss the difference between using ND and imposing a downstream water level boundary condition, and the present study aims to provide more insight into how exactly downstream conditions such as backwater or imposed rating curves, affect the simulated streamflow. Testing the sensitivity of these parameters quantifies their impact on the hysteresis signal and underlying flow variables. In turn, these trials inform riverine monitoring and modeling protocol through the development of parameter range guidelines.

2. Methods

2.1. Numerical Modeling

Numerical models such as the Hydrologic Engineering Center's River Analysis System (HEC-RAS) allow researchers to examine river dynamics by outputting fine spatial-temporal time series of any hydraulic variable. This produces hydraulic variable time series to accurately calculate the ingredients of the St. Venant momentum terms as in House et al. (2025a). We use a geometrically reduced-complexity 1D HEC-RAS model to gain control over the analysis. Using a simple cross-section and a long, extended channel, characteristics such as bed slope, roughness, and boundary condition stage-flow time series are applied to reduced complexity models to represent a river reach. Three benefits of this modeling strategy are (1) a clear interpretation of the results in the absence of complex river variability, (2) use of geomorphic and hydraulic specifications of a site with severe hysteresis (Muste et al., 2025a), and (3) an increased capacity for more detailed simulations with shorter runtimes.

As a case study to ground the analysis, the present study focuses on a stream gage location along the Illinois River (USGS #05558300 at Henry, IL). The flow at this station can be characterized by a large loop rating curve with rising discharge larger than falling discharge for a given stage (Figure 1). A description of the site's characteristics and the May-June 2019 event, as well as more information on modeling techniques and momentum term calculations, can be found in House et al. (2025a). The average base parameters of the site, relevant to the sensitivity analysis, are a constant bed slope of 0.00027, a Manning roughness coefficient of 0.03, and a rectangular/prismatic channel shape 450 m width. The base event, of which is modified in shape and intensity to explore hysteresis sensitivity to flow conditions, is an April-May 2019 storm event which exceeds the major flood line defined at the site (3,000 vs. 2,300 cms; Figure 3a).

There are characteristic signals for hysteretic streamflow in the St Venant momentum term budget which we note (de Saint-Venant, 1871; Meselhe et al., 1997; Knight, 2005). For the Illinois River at Henry, the friction and gravity terms are unequal and out of phase, while there is an active pressure gradient and convective acceleration term, indicating diffusive-dynamic flow waves (House et al., 2025a). There is also a clear phasing of the bulk terms, dynamic terms, and flow variables with hysteretic streamflow. During the rising limb, kinematic forces dominate, and during the falling limb, pressure gradient forces take over. In less hysteretic streamflow, kinematic forces dominate, and flow is more steady and uniform in character. We note the momentum term characteristics for each parameter permutation of the sensitivity analysis to characterize hysteresis.

2.2. Sensitivity Permutation Matrix

A sensitivity analysis was performed using the reduced complexity HEC-RAS model to explore the effects of different model geometries and boundary conditions (Table 1) on the strength of streamflow hysteresis. A wide range of realistic parameter values were explored utilizing hydromorphic conditions at the Illinois River at Henry, IL gage as a reference point. From there, model scenarios were introduced with varied bed slope, roughness, and hydrographs, both those observed at the *in-situ* gage and through extended scenarios designed to test system and process limits. Nearly every combination of channel geometries (bed slope, roughness, cross section shape, contractions and expansions), and boundary conditions (wave shape, intensity, and backwater effect) from the Table 1 were tested to encompass a wide range of conditions that are possible in natural channels except (1) the channel shape parameter, which was tested for all flow scenarios but only the base condition of other geometry parameters (i.e., bed slope and roughness), and (2) the Q estimation methods, which were only tested as a case study for the base hydrograph and the two prismatic case studies. In total, 274 permutations for the sensitivity analysis were tested.

Table 1: *Simulation scenarios for the streamflow hysteresis sensitivity analysis with reduced-complexity models.*

Parameter	Scenarios			
Bed Slope	Mild ($S_0 = 0.0001$)	Base ($S_0 = 0.00027$)	Steep ($S_0 = 0.0005$)	Steepest ($S_0 = 0.001$)
Roughness	Smoother (n = 0.02)	Base (n = 0.03)	Rough (n = 0.1)	Rougher (n = 0.2)
Wave Shape	T_F/T_R = 8.6 (Skewed)	T_F/T_R = 3.7 (Base)	T_F/T_R = 4.3 (Multi-pulse)	T_F/T_R = 3.4 (Long Multi-pulse)
Wave Intensity	Minor (Q ≈ 1,000 cms)	Low (Q ≈ 2,000 cms)	Base (Q ≈ 3,000 cms)	Intense (Q ≈ 4,500 cms)
Backwater Effect	Low (0.5x)	Medium (0.75x)	None (ND)	High (1.25x)
Channel shape	Rectangular	Rectangular & 50% expansion	Rectangular & 50% contraction	Composite
Q Estimation	HQRC	IVRC	Jones	Fenton

The ranges of modeled parameters encompass a wide range of conditions, as detailed in Table 1 and illustrated in Figures 3-5. Channel *bed slope* S_0 was varied from 0.0001 to 0.001, from relatively low bed slopes to an order of magnitude steeper, values that approach the steepness limit of what HEC-RAS can computationally carry out. Channel *roughness* was also varied by an order of magnitude, from a Manning's n of 0.02 (smooth, clean earthen channel) to 0.2 (a channel with dense willow trees; Chow, 1959).

The wave shape and intensity together define the wave severity. To explore different *wave shapes*, a variety of hydrographs were simulated, including those with differently skewed (Figure

3a) and multi-pulse (Figure 3c-d) waveforms, and then passed through the modeled channel. The downstream boundary condition was modified to reflect each scenario, using a stage time-series that matches the corresponding hydrograph shape. Wave shape in Table 1 was quantified based on the flow hydrograph recession ratio (T_F/T_R), where the first peak serves as the turning point for the multi-pulse scenarios (McCuen, 1989; Lee & Granato, 2012). *Wave intensity* was varied based on the flood warning lines at the Henry, IL gage. In this way, the simulations are representative of every type of historical event at the site. The minor event scenario falls below the action line, low scenario is above moderate flood line, base scenario is above the major flood line, and the intense flood scenario is greater than any flood in the historical record (NOAA, 2022). However, the downstream boundary was not varied accordingly for the wave intensity scenarios, instead, the base stage time series was used for all intensities.

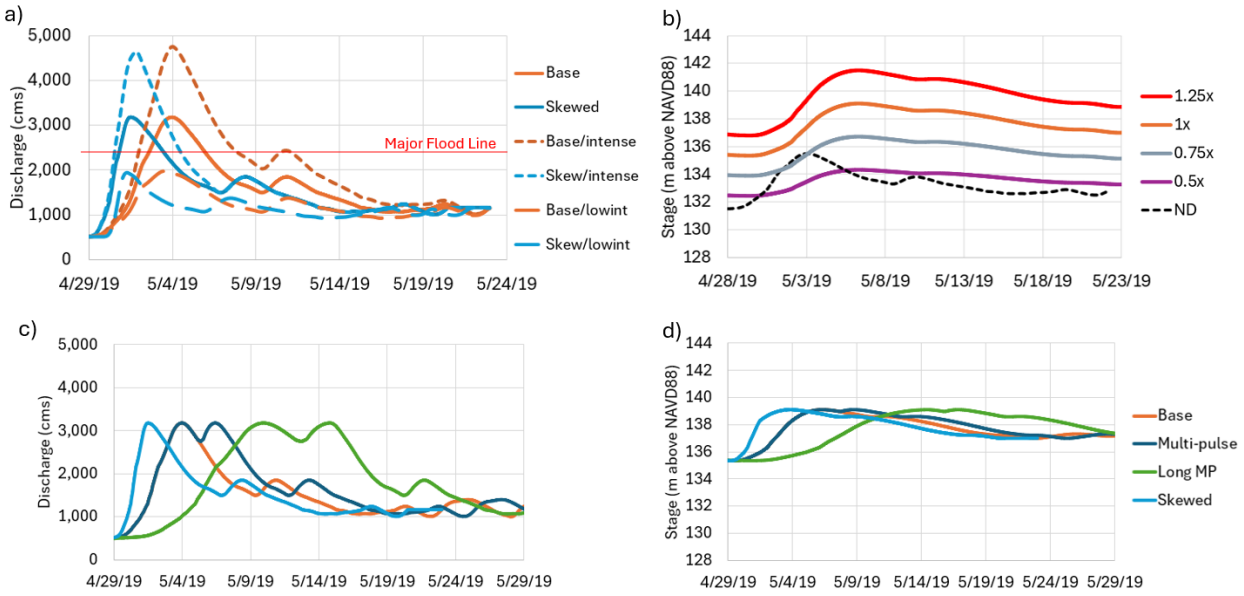

Figure 3: *Input hydrographs for the sensitivity scenarios: a) event wave intensity and shape (base and skewed) scenarios varied discharge hydrographs supplied at the upstream boundary, b) backwater scenarios varied stage hydrographs supplied at the downstream boundary, c) hydrograph shape scenarios varied discharge hydrographs supplied at the upstream boundary, and d) hydrograph shape scenarios varied stage hydrographs supplied at the downstream boundary.*

The *backwater effect* was varied by multiplying the depth time series at the downstream boundary by different coefficients: 0.5, 0.75, and 1.25 (Figure 3b). The base scenario (coefficient of 1) was included in this parameter range for comparison. The *normal depth* condition is somewhat of its own case but is included in Figure 3b as it is a downstream boundary option specified in HEC-RAS. The *channel shape* was modified for the sensitivity analysis as shown in Figure 4, prismatic, contracting, and expanding (a-c, respectively) plan views of the reduced complexity channel were permuted with the base rectangular cross-section shape (Figure 4d, dashed line). There was also the exploration of the compound channel cross-section shape (Figure 4d, solid line) which was permuted for all scenarios, especially for exploring the Q-estimation parameter.

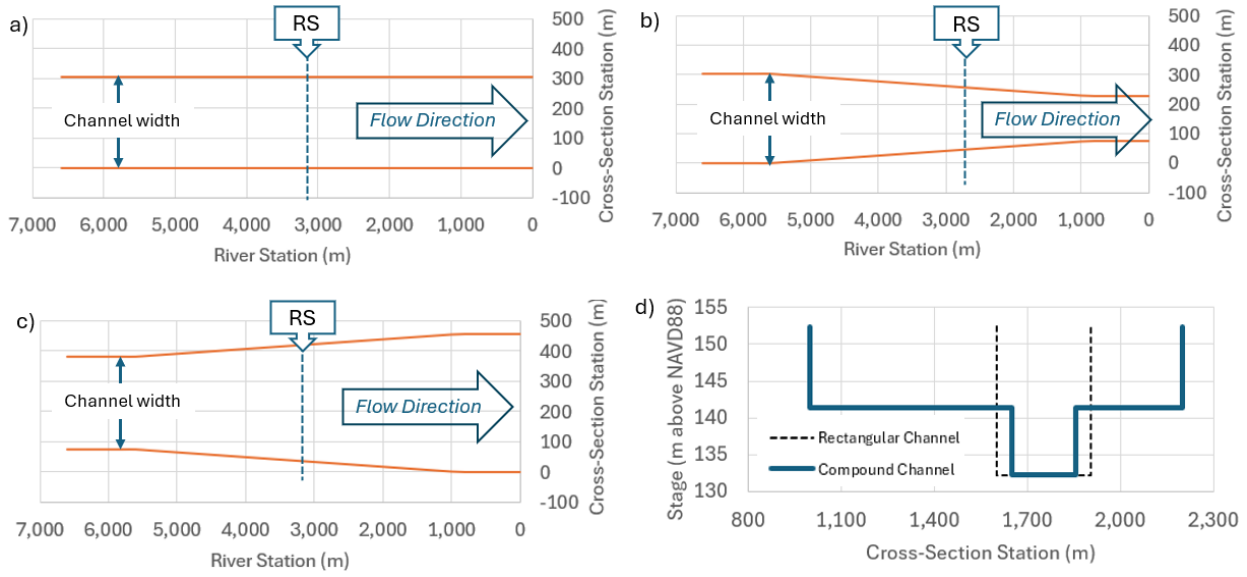

Figure 4: *Channel shape scenarios in plan view: a) prismatic, b) contracting, and c) expanding; in cross-section view: d) rectangular vs. compound channel geometries.*

Finally, as detailed in the last row of Table 1 and illustrated in Figure 5, the impact on the modeled reach was explored by employing various *Q-estimation methods* to calculate the upstream flow boundary as in Muste et al., (2025a). Each of these methods, namely the stage-discharge HQRC and index-velocity IVRC methods, produce different timing, magnitude, and loop shape properties, which may have an impact on the modeled reach.

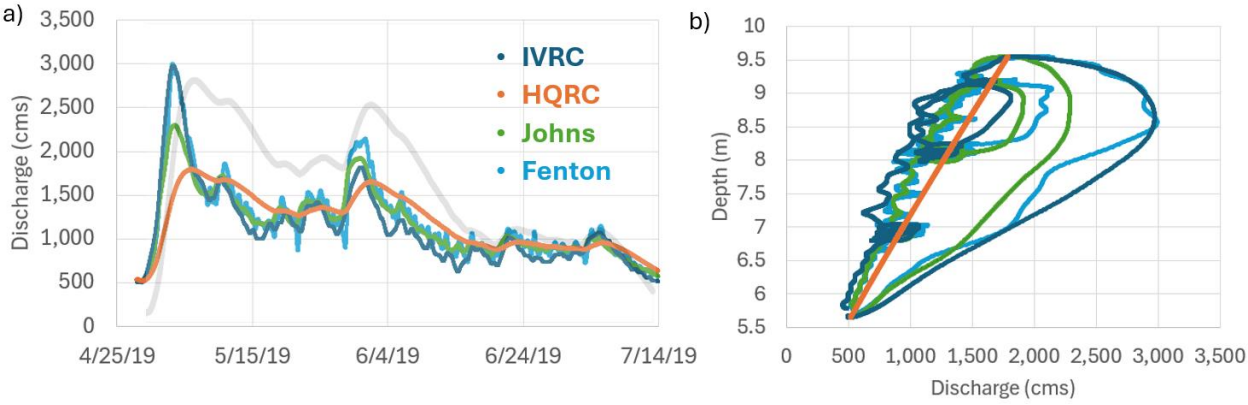

Figure 5: *Discharge (Q) estimation method scenarios input as a) varied upstream discharge boundary time series; the light gray line in this plot is the time series for stage (used to compute these discharges at the upstream boundary), for reference. The panel b) is the stage-discharge rating curve for the upstream boundary cross-section.*

To explore more complex retrieval techniques, the River Analysis System (RAS) Controller tool was utilized to efficiently run this extensive series of simulations (Goodell, 2014). A Visual Basic for Applications (VBA) script seamlessly set up RAS plans, ran HEC-RAS, and extracted the desired data from them in a user-efficient loop. Detailed model output was examined to assess the severity of hysteresis in relation to flow and channel characteristics, thereby

expanding upon factors noted in the literature. The attribution of hysteresis loop thickness to its underlying flow regime and physics was made via this comprehensive range of conditions.

To examine the flow dynamics throughout the streamflow hysteresis cycle, the individual terms of the St. Venant equation (Supplementary Eq. 2) were calculated using outputs from the reduced-complexity models at a detailed time step. With the output time series (flow, velocity, cross-sectional area, water surface, and friction slopes, etc.) of an unsteady simulation, the different terms (local acceleration, convective acceleration, pressure gradient, and friction forces) were examined. The magnitude of the momentum terms varies during the wave propagation with the dispersion and subsidence of the wave, and with varied scenarios (Henderson, 1966; Ferrick, 1985; House et al., 2025a). As a rule of thumb, if any of the uncovered momentum forces are an order of magnitude smaller than the others, the term can be discarded, and the flow may be characterized by those remaining dominant forces (Eames & Hunt, 1997; Muste et al., 2020a). Drawing correlations between channel characteristics, boundary conditions, hysteresis loop thickness, and the relative magnitude of the momentum terms forms the results of this study.

Previous studies have focused on the separation of these forces within the exploration of wave types and flow routing to identify the applicability of various forms of the St Venant equations (Ferrick et al., 1985; Meselhe et al., 2021; House et al., 2025a). To further classify the dominant driver of hysteresis evolution, whether it is controlled locally or influenced by downstream conditions, we utilized the Froude number (Supplementary Eq. 3). Offering a response variable that blends velocity and depth and is sensitive to changing flow conditions, this dimensionless diagnostic characterizes the relative importance of gravitational and inertial forces in open channel flow and provides insight into the flow regime and wave propagation behavior (Meselhe et al., 2021).

2.3. Statistical Data Analysis and Visualization

Variable importance ANOVA and Random Forest (RF) analyses were employed to initially identify the most influential contributors to streamflow hysteresis within the large dataset (Brown et al., 2014; Zhang et al., 2024). These methods are well-suited for sensitivity analyses because ANOVA can quantify the significance of individual predictors, while RF can rank their relative contributions and capture nonlinear and interaction effects among variables (Graham & Edwards, 2001; Simon et al., 2023). The assessed driving factors include channel shape, event wave shape, channel bed slope, Manning's roughness, and backwater effect, excluding special-case multi-pulse and compound scenarios. The selected dependent variable is the phasing time between peaks of velocity (V) and water surface elevation (WSE), an indicator of hysteresis. This metric was chosen because V is typically more sensitive and exhibits clearer phasing than discharge (Q) in hysteretic rivers (as illustrated by the greater loop thickness of the red line relative to the black line in Figure 1b). The free-surface slope (FSS), though most sensitive, was too noisy to be employed (also, FSS indicates an incoming wave in general, not necessarily a hysteretic one).

We employed visualization techniques to study the momentum forces for the sensitivity analysis. Scatter plots highlight the most crucial information across many batches by summarizing each time series (i.e., each line in the gradient plots) with two values: (1) the absolute value peak pressure gradient magnitude and (2) the time difference between the V-WSE peaks. These metrics captured the most critical attributes of each scenario simulation, acting as proxies for streamflow

hysteresis, respectively: the relative strength and dominance of the diffusive term, and the timing "lag" (or lack thereof) in V-WSE relationships. This approach enabled large datasets to be viewed clearly as clouds of points. Summary figures also include gradient plots, which dive deeper, presenting full time series for momentum terms and flow variables from a given batch of scenarios. Plotted in time (variable hydrographs) and with stage (stage-variable ratings), these revealed peak-phasing and lag aspects of hysteretic streamflow within the St Venant momentum terms and were used to evaluate hysteresis drivers. The sketch in Figure 6 (panel a) demonstrates the concept and how to interpret the peak magnitude timing scatter plots (Figures 8-11), while panels b-g demonstrate the gradient plots (Figures 12-15).

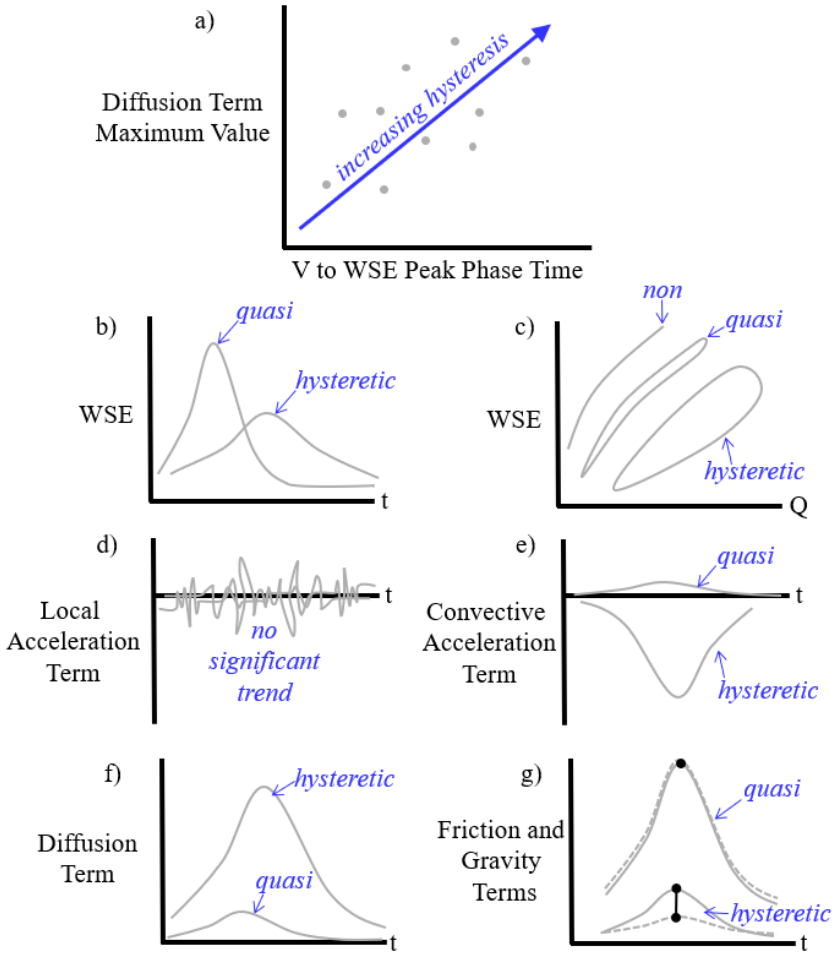

Figure 6: *Conceptual sketches to guide interpretation of the summary figures: a) peak magnitude timing scatter plots, and b-g) full time series gradient plots, with the blue arrow indicating the direction of increasing hysteresis strength.*

Finally, in a case study of Q-estimation methods, we demonstrated the impact of imposing differently calculated upstream flow boundary conditions (i.e., HQRC vs. IVRC, as in Muste et al., 2025a) on the representation of hysteretic streamflow. We present a breakdown of the flow variables in matrix form for rectangular and compound channels.

3. Results

The findings of this study include a range of results from various hydraulic model setups, previewed in the resulting stage-discharge rating curves, in Figure 7. The results are presented in several forms. Common statistical summary techniques (ANOVA and RF) are utilized to analyze sensitivity for determining the most important hysteresis drivers. Scatter plots of all scenarios highlight these drivers and patterns, as sketched in Figure 6a. The main results are in the form of gradient plots focused on the range of conditions for each parameter as time series to further compare the hysteresis sensitivity, as sketched in Figure 6b-g. Discharge estimation permutation results are presented as a breakdown of the momentum terms time series for the base event and prismatic channel conditions in matrix form. All matrices of channel and flow characteristics for stage-discharge time series and rating curves may be found in Supplementary Figures 1-34.

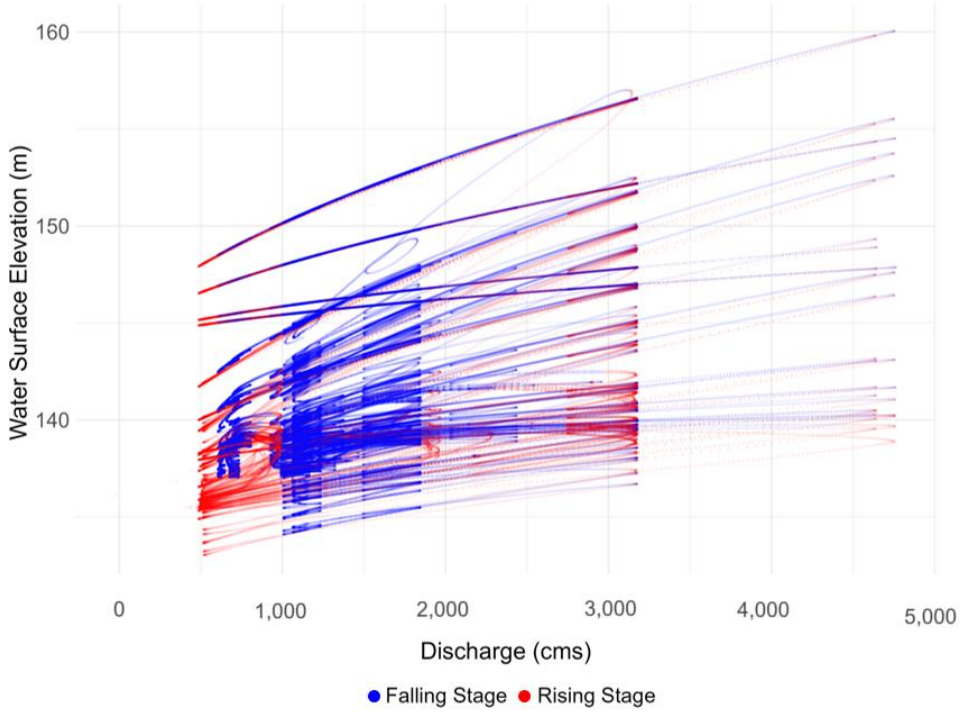

Figure 7: *Stage-discharge rating curve "cloud" for all scenarios run in this analysis, showing the range of permutations covered and phases of the stage hydrograph distinguished with color.*

3.1. Variable Contribution Assessment

Variable contribution assessment techniques were used to evaluate the most important drivers of streamflow hysteresis, effectively calculating sensitivity metrics. This includes key driving factors (channel shape, event wave shape, channel bed slope, Manning's roughness, and backwater effect) with a hysteresis indicator as the dependent variable (the phasing time between V and WSE peaks). The resulting tables are shown in Supplementary Tables 1-5.

The Analysis of Variance or ANOVA linear model had an R^2 of 0.69, which is reasonably good considering the difficulty in capturing nonlinear effects related to hysteresis. The variance was explained by all parameters (all with $p < 0.05$): validation that the selected parameters are significant drivers of hysteresis. To determine the most important drivers of hysteresis, if the RF model was examined without each of the driver variables, the Mean Squared Error (MSE) increased significantly: event wave shape by 45%, event wave intensity by 28%, bed slope condition by 23%, roughness condition by 16%, and backwater condition by 15%. The Q-Est

method and channel shape only increased the MSE by 0-7%. This analysis allowed a focus on the four most influential groups: roughness, bed slope, event wave intensity, and backwater conditions.

3.2. Peak Magnitude Timing

The peak pressure gradient magnitude and V-WSE timing for 234 out of the 274 total scenarios (excluding compound channels, multi-pulse, or Q-estimation) were summarized and presented in magnitude-timing plots as introduced in Figure 6a. Scatter plot points were colored according to the specific condition of interest (i.e., roughness values in Figure 8), highlighting the base scenarios for each condition with a circle around the point. Linear regression curves were fit to compare the magnitude-timing trends commensurate with hysteresis.

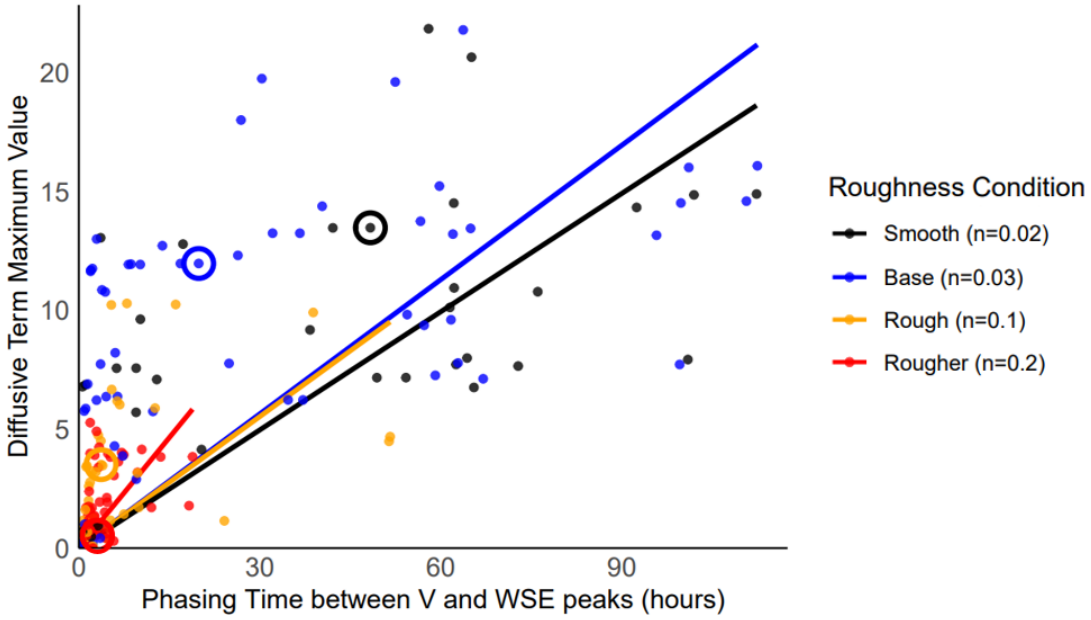

Figure 8: *The pressure gradient, or diffusive force, gA(dy/dx), summarized by peak magnitude and V-WSE peak phasing time, and colored according to roughness condition, for all scenarios. A local regression curve was employed for scenarios that fall within each roughness condition.*

With the pressure gradient force in Figure 8, there is a disparity between rougher and smoother scenarios, with the rougher scenarios having a small pressure gradient and range of phasing, and the smoother scenarios having large pressure gradients and peak phasing. In turn, the hysteresis is smaller with increasing roughness.

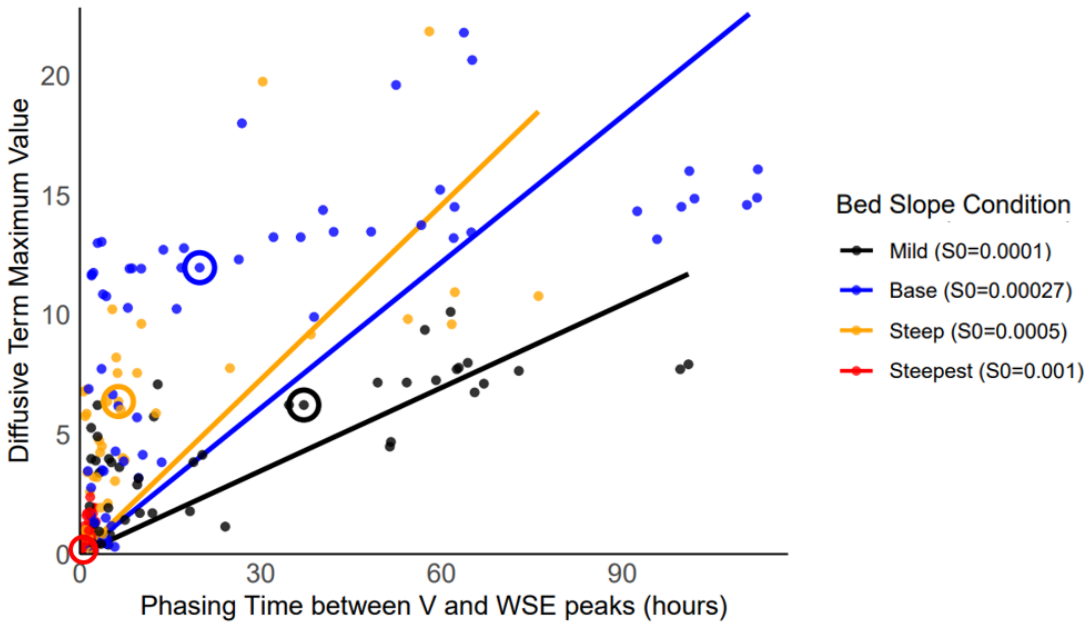

Figure 9: *The pressure gradient, or diffusive force, gA(dy/dx), summarized by peak magnitude and V-WSE peak phasing time, and colored according to bed slope condition, for all scenarios. A local regression curve was employed for scenarios that fall within each bed slope condition.*

Figure 9 reveals how extreme the impact of bed slope, particularly the steepest channels, was on the peak phasing characteristic of hysteresis. The steepest scenario fell consistently on the y-axis, indicating kinematic, non-hysteretic streamflow. With gentler slope channels, velocities naturally decreased, and the phasing increased.

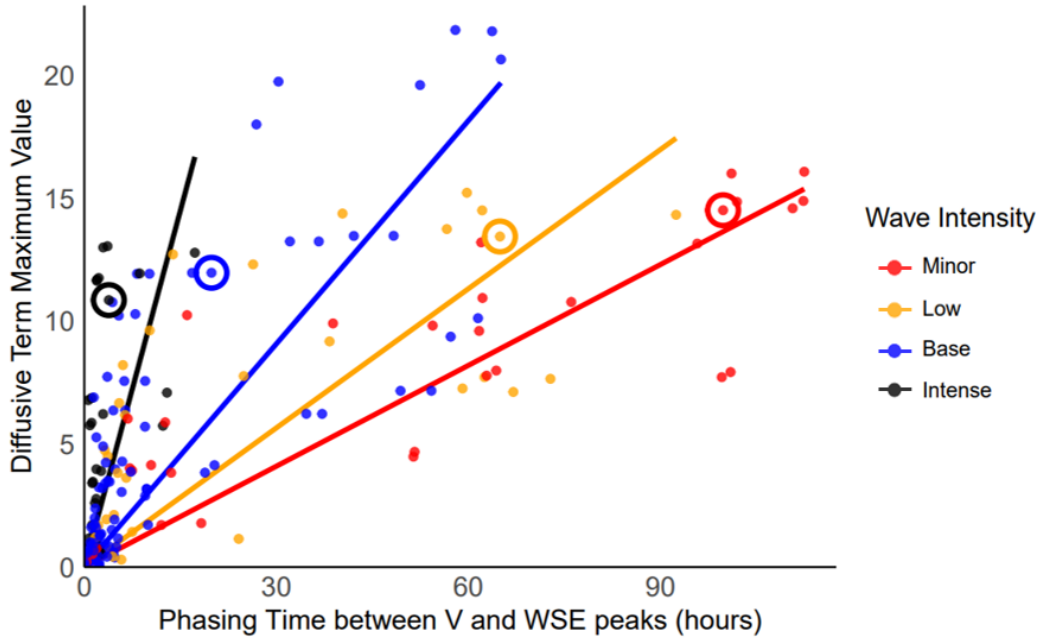

Figure 10: *The pressure gradient, or diffusive force, gA(dy/dx), summarized by peak magnitude and V-WSE peak phasing time, and colored according to event wave intensity, for all scenarios. A local regression curve was employed for scenarios that fall within each event wave intensity.*

In Figure 10, the pressure gradient remained in a similar range while there was a decrease in the peak phase timing with the event wave intensity.

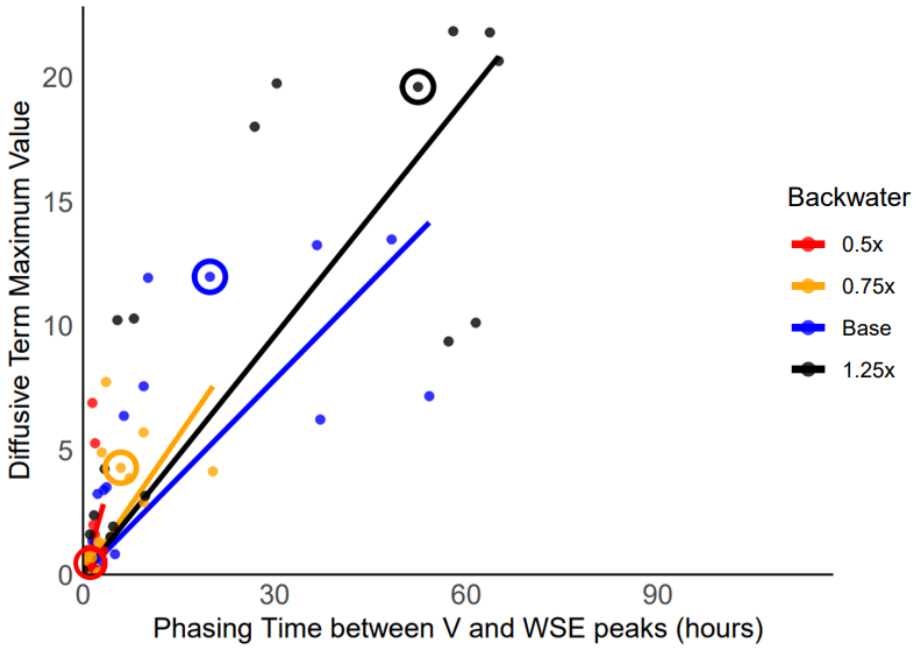

Figure 11: *The pressure gradient, or diffusive force, gA(dy/dx), summarized by peak magnitude and V-WSE peak phasing time, and colored according to backwater condition, for all base scenarios. A local regression curve was employed for scenarios that fall within each backwater condition.*

In Figure 11, the backwater condition is distinct between the higher and lower backwater scenarios. There was an increasing trend in pressure gradient magnitude and V-WSE peak phase timing with higher backwater.

3.3. Time Series Gradient Plots

The most significant parameters in our streamflow hysteresis simulations are plotted as gradients (introduced in Figure 6b-g) for further exploration and visualization in Figures 12-15, along with channel shape in Supplementary Figure 35. Dimensionless Froude number is explored as gradient plots for all parameter ranges in Figure 16 to provide insight into the relevant hydraulic mechanisms.

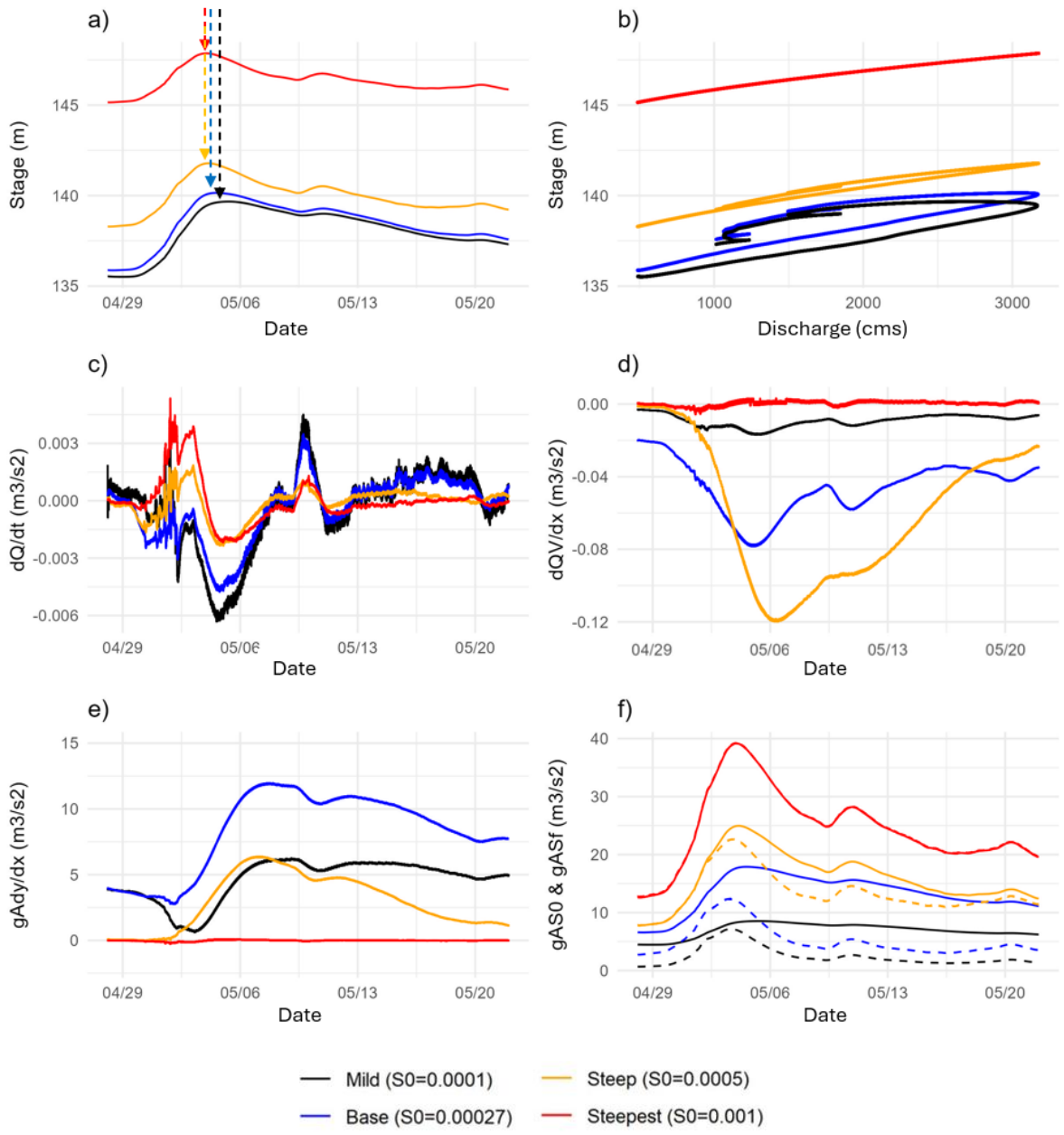

Figure 12: *Gradient plots for varied bed slope permutations under base conditions for other parameters: a) stage hydrographs, b) stage-discharge rating curves, c) local acceleration term, d) convective acceleration, e) pressure gradient, and f) kinetic forces: gAS_0 shown with a solid line and gASf with a dashed line.*

As Figure 12 illustrates, lower slope channels facilitate attenuation in the stage hydrograph (panel a), and a corresponding opening of the stage-discharge hysteresis loop (panel b). All of the hysteretic rating curves had active convective acceleration (panel d) and pressure gradient (panel e) forces. Steeper bed slopes became increasingly kinematic, losing convective acceleration (panel d) and pressure gradient forces (panel e), with the kinematic terms (panel f) becoming increasingly large and in-sync. The local acceleration term (panel c) remained comparable in (negligible) magnitude and behavior, pertaining only to the discharge, progressing the wave in time.

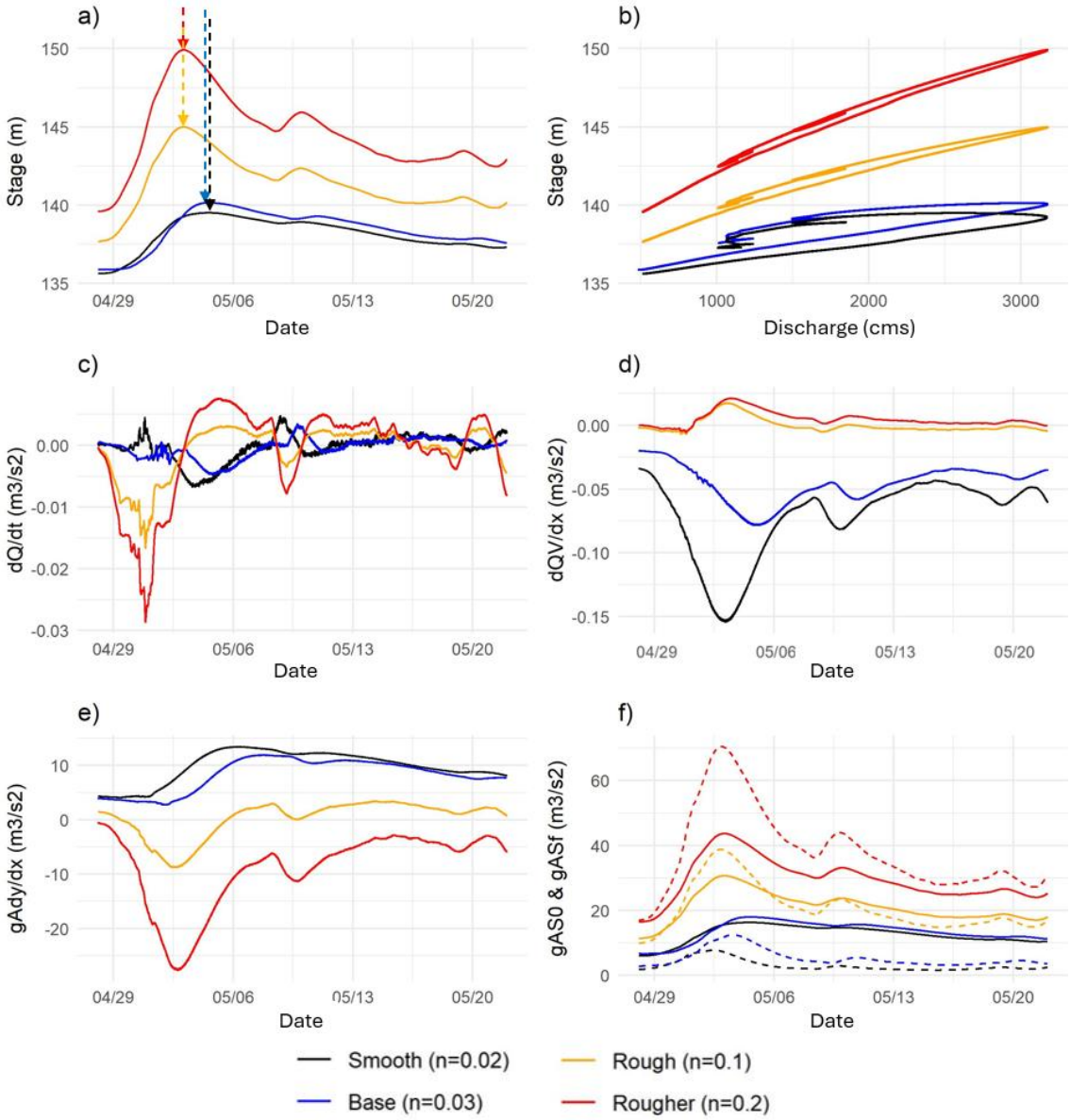

Figure 13: *Gradient plots for varied roughness permutations under base conditions for other parameters: a) stage hydrographs, b) stage-discharge rating curves, c) local acceleration term, d) convective acceleration, e) pressure gradient, and f) kinetic forces: gAS_0 shown with a solid line and gASf with a dashed line.*

As Figure 13 illustrates, smoother channels showed a peak attenuation in the stage hydrograph (panel a), and an enlargement of the stage-discharge hysteresis loop (panel b). Smoother channels also had negative convective acceleration forces (panel d), as did all of the hysteretic bed slope condition scenarios in Figure 12, but the rougher channels depicted the presence of a slightly positive force. Balancing this, the smoother channels had positive pressure gradient forces, while the rougher channels had negative (panel e). The kinematic terms (panel f) increased with roughness, with peak phasing diminishing along with the hysteresis.

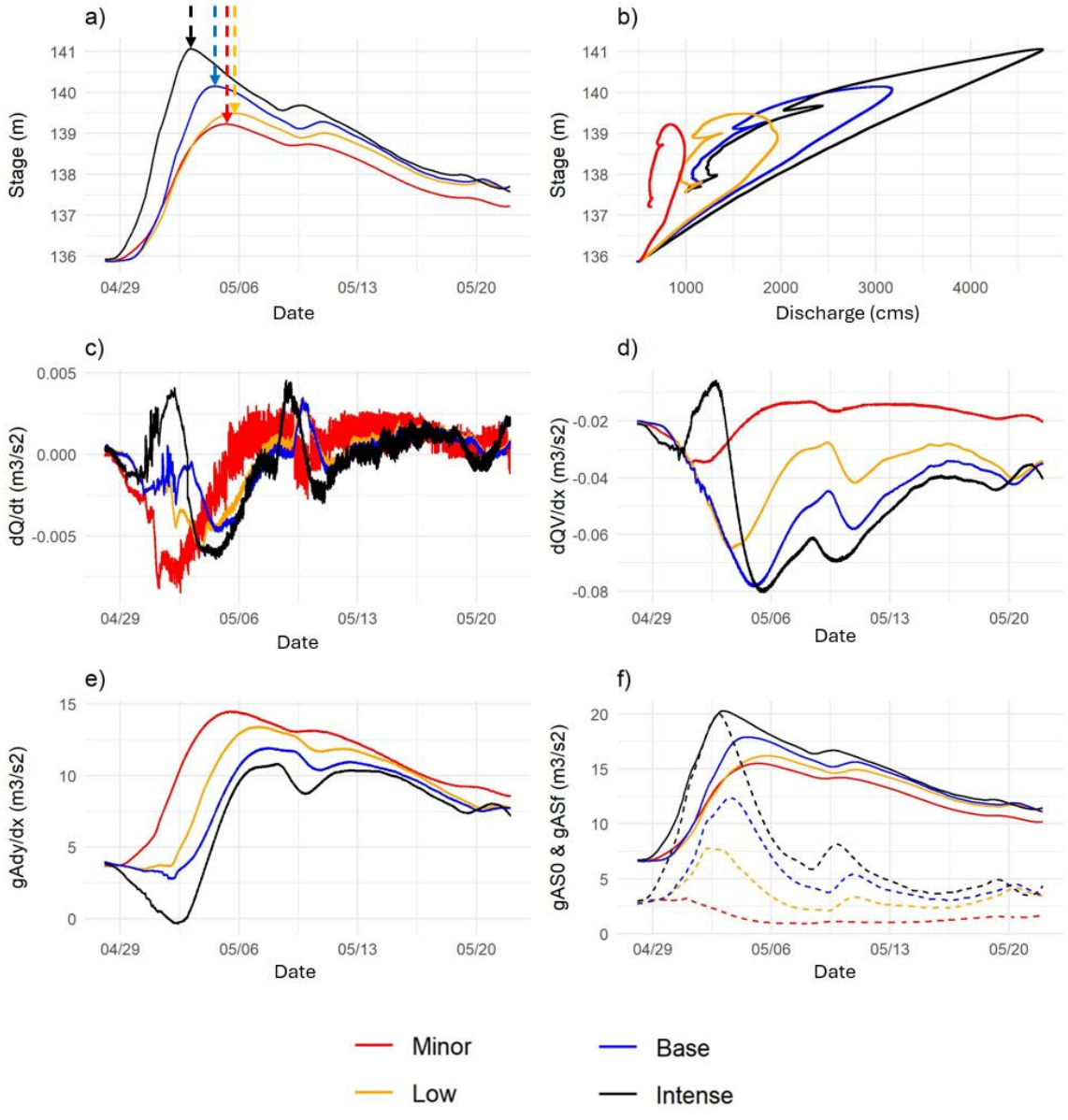

Figure 14: *Gradient plots for varied event wave intensity permutations under base conditions for other parameters: a) stage hydrographs, b) stage-discharge rating curves, c) local acceleration term, d) convective acceleration, e) pressure gradient, and f) kinetic forces: gAS_0 shown with a solid line and gASf with a dashed line.*

As Figure 14 illustrates, all of the wave intensity scenarios exhibit significant hysteresis effects. The more intense fluvial waves naturally caused higher stages (panel a) with flashier peaks, yielding pointy hysteresis loops (panel b). This may be associated with the large convective acceleration (panel d) forces. In turn, smaller events had a greater peak attenuation in the stage hydrograph (panel a), and rounder stage-discharge hysteresis loops (panel b). They exhibited greater pressure gradient (panel e) forces. Additionally, large magnitude and timing differences in the kinematic terms (panel f) signaled hysteresis with the two lowest event wave scenarios, while the most intense event had near-equal gravity and friction forces during the rising limb and peak (panel f).

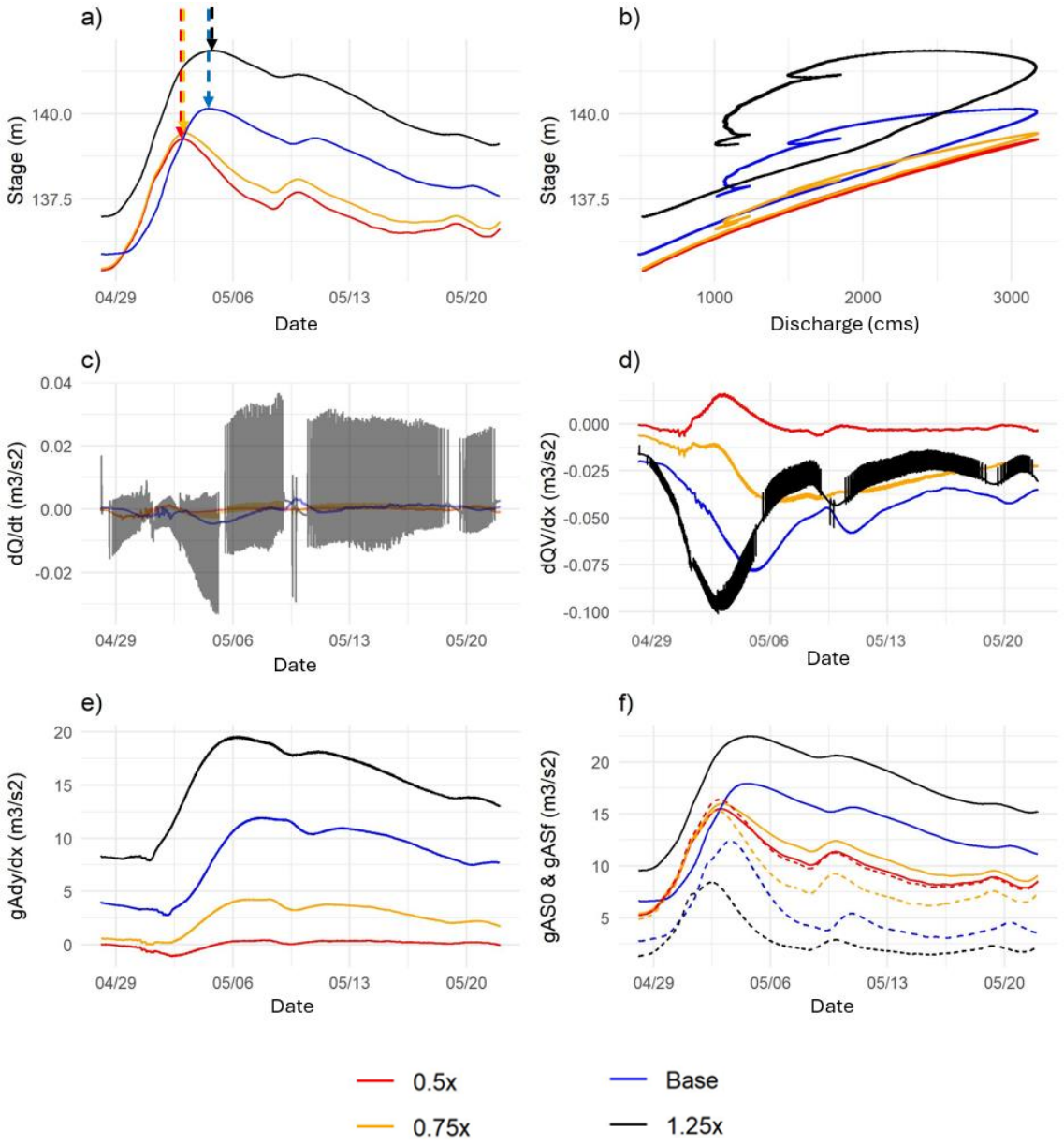

Figure 15: *Gradient plots for varied backwater permutations under base conditions for other parameters: a) stage hydrographs, b) stage-discharge rating curves, c) local acceleration term, d) convective acceleration, e) pressure gradient, and f) kinetic forces: gAS_0 shown with a solid line and gASf with a dashed line.*

As Figure 15 illustrates, higher backwater naturally caused higher stages, a peak attenuation in the stage hydrograph (panel a), and an extremely exaggerated stage-discharge hysteresis loop (panel b). This is associated with the large convective acceleration (panel d) and pressure gradient (panel e) forces. Additionally, large magnitude and timing differences in the kinematic terms (panel f) signaled hysteresis in the two highest backwater scenarios. Meanwhile, decreased backwater effect caused stage peaks to occur earlier (panel a), the loop to flatten (panel b), and momentum forces (if considering the kinematic term as a whole) to be near-zero (panels d-f). The local acceleration term (panel c) remained comparable in (negligible) magnitude and behavior, excluding the noise within the highest backwater scenario.

In Figure 16, the time series and rating curves for stage-Froude number varied drastically within the parameter ranges: bed slope, roughness, event wave intensity, backwater condition, event wave shape, and channel shape.

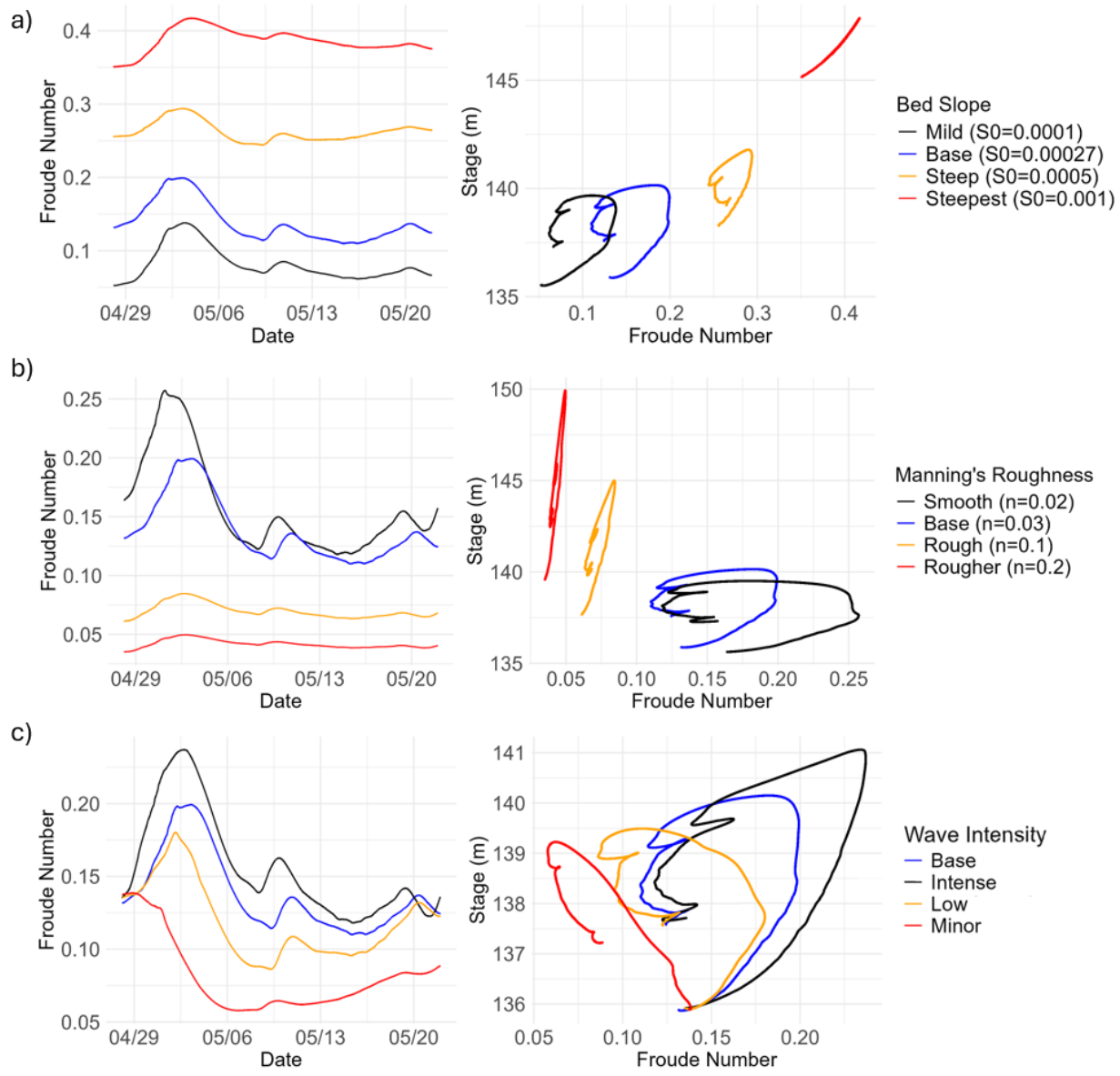

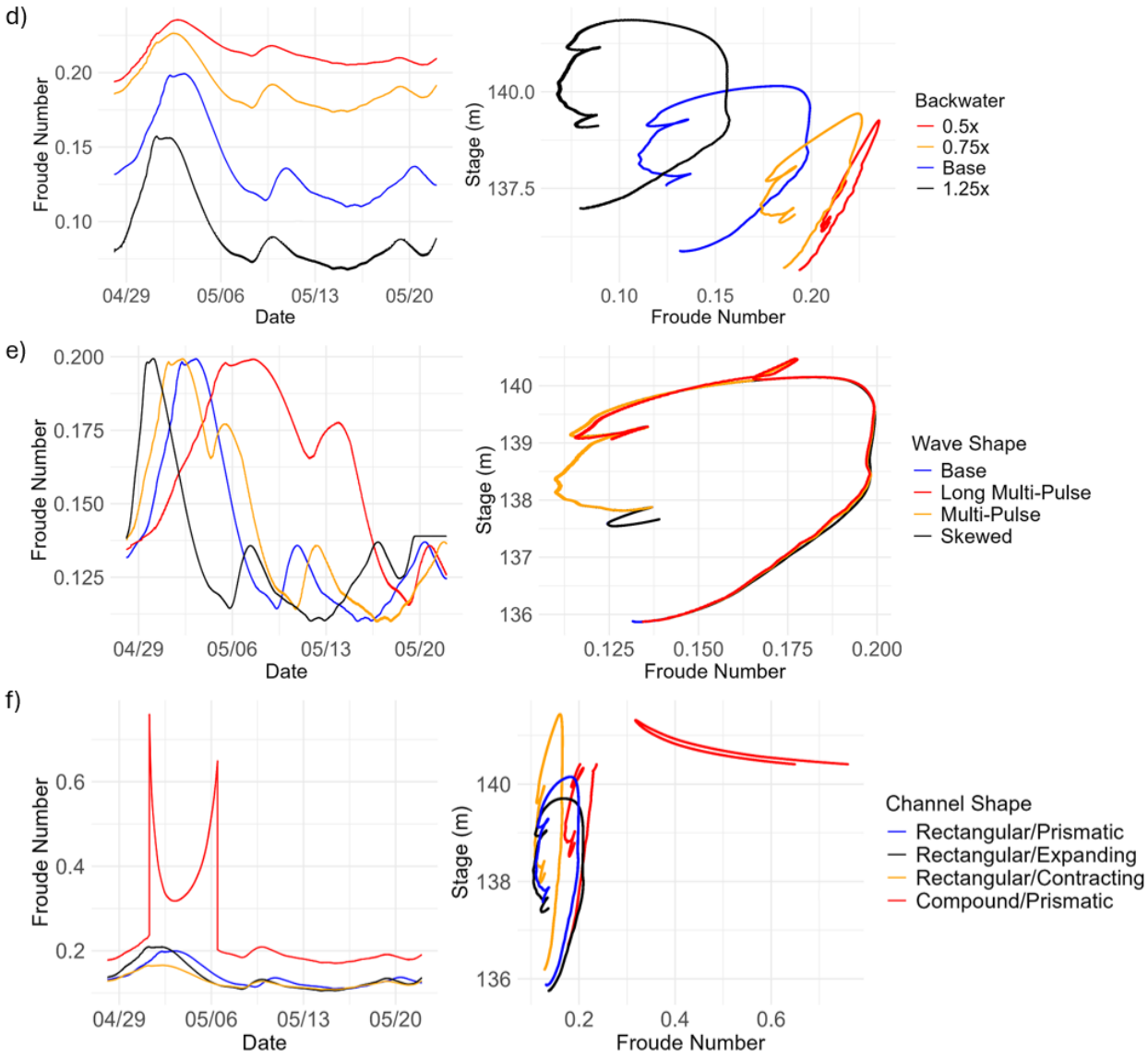

Figure 16: *Froude number gradient plots, with Fr time series on the left and stage-Fr rating curves on the right, for all parameter permutations: a) bed slope, b) roughness, c) event wave intensity, d) backwater condition, e) event wave shape, and f) channel shape, under base conditions for other parameters.*

In Figure 16, patterns in Froude number behavior are apparent throughout each of the parameter ranges. All Fr values were below 0.8 (most are below 0.3) as HEC-RAS only supports subcritical flow simulations. For a) steeper bed slopes, Fr increased, peaked later, and hysteresis decreased; b) greater roughness values decreased Fr and collapsed hysteresis; c) intensifying flood waves increased Fr and formed larger, pointier loops; d) higher backwater conditions decreased Fr and increased hysteresis; e) event wave shape had minimal effects on the stage-Fr rating curve; and f) expanding channel widths increased Fr while increasing hysteresis. The variant trends in Fr and hysteresis development revealed classifications of flow control.

3.4. Discharge Estimation Methods

The impact of Q-estimation methods on streamflow hysteresis development and representation in a 1D modeled river channel was explored by comparing results from the HQRC and IVRC methods following the formulations from Muste et al., (2025a). We found that the Fread method, although more grounded in true theory than the others, produced data that was too noisy to be included in the model permutations. Additionally, the flow representation from the Jones and Fenton methods, each based on different assumptions, yielded similar streamflow representation to the IVRC, a more realistic and currently implemented method (Levesque & Oberg, 2012; Muste et al., 2020b). Thus, we only compared results from the HQRC and IVRC methods in Figures 17-18, and the remainder may be found in Supplementary Figures 1-2.

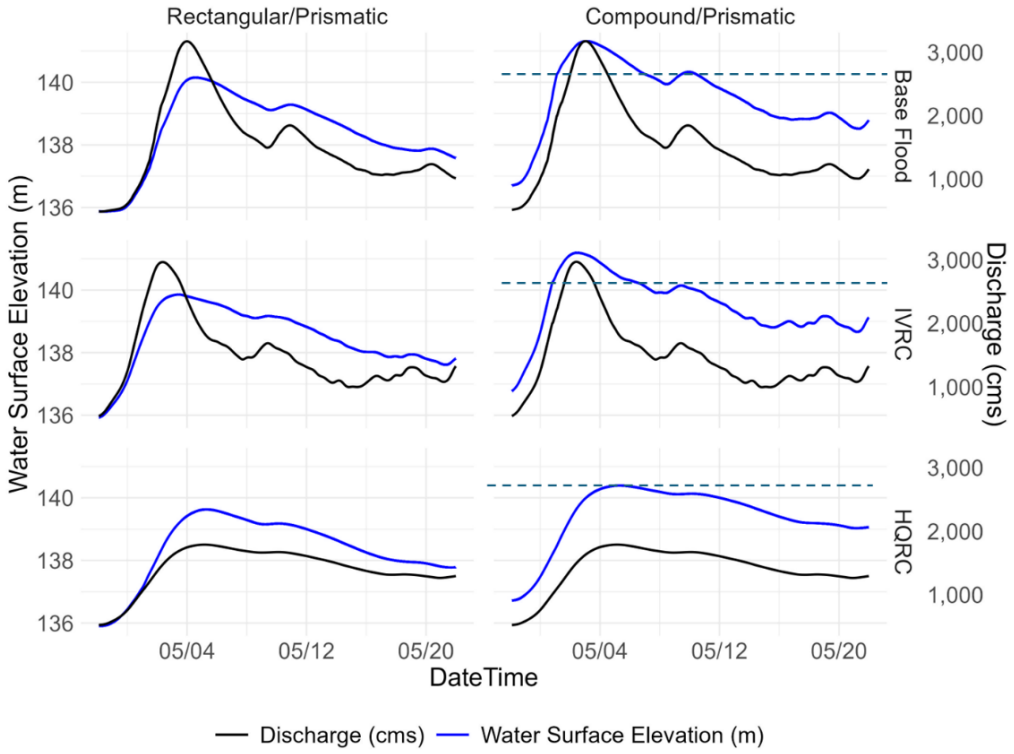

Figure 17: *Stage and discharge hydrograph matrix by channel cross-section shape (columns) and discharge estimation methods for supplying the model upstream flow boundary (rows).*

In Figure 17, it is apparent that the Q-estimation method affected hydrograph timing, magnitude, and noisiness. Across both channel types, there was a noticeable distinction in Q hydrograph shape between the two monitoring methods. The IVRC more closely matched the base scenario in terms of flow magnitude and timing (hysteresis), though its hydrograph was slightly noisier than the base and HQRC results.

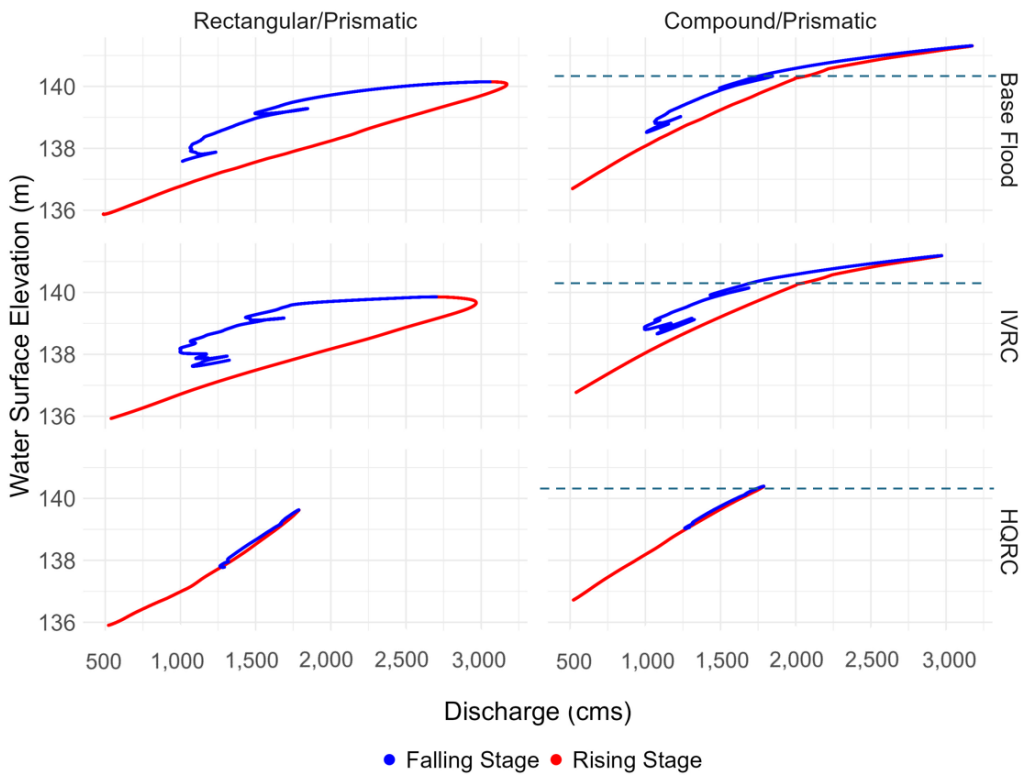

Figure 18: *Stage-discharge rating curve matrix by channel cross-section shape (columns) and discharge estimation methods for supplying the model upstream flow boundary (rows).*

In Figure 18, it is apparent that the HQRC method collapsed the hysteresis loop entirely and underestimated both peak discharge and stage. Since the hysteresis was not represented, there were significant magnitude and timing errors with the HQRC-driven sensitivity scenarios. The IVRC method more accurately represented peak streamflow, closely capturing the true peak and resolving the hysteresis loop shape and (phased) timing. Overall, this experiment highlights how the method used to estimate the upstream discharge boundary condition can significantly impact the development and representation of streamflow hysteresis in a modeled river channel.

Likewise, using a normal depth condition at the downstream of the hydraulic model dramatically impacted the streamflow hysteresis representation in the reach: completely collapsing the phasing and loop. This parameter was varied with the two prismatic channel shapes and with every other geometry scenario (different bed slopes, roughness, etc.; Supplementary Figures 7-8, 16-17, and 26-27).

4. Discussion

With detailed model-simulated data, the present study adds evidence-based support to the scientific understanding of streamflow hysteresis development. In our 274 scenarios, we explored typical flow variables and channel characteristics and analyzed the underlying momentum terms. Table 1 was designed to address the relevance of varying channel and flow parameters to the behavior of streamflow hysteresis, and the sensitivity analysis through HEC-RAS Controller provides the capability to assess this wide range of scenarios in detail.

Hysteresis has several defining characteristics: the "lag" between variables in time, the corresponding "loop" in variable relationships (Figure 1), and key momentum forces whose activity are relevant in hysteretic streamflow. Ferrick (1985) proposed that diffusive-type waves contribute the most to hysteresis development. Additionally, House et al., (2025a) identified convective acceleration forces arising alongside this pressure gradient, as disparities between the kinematic terms (gravity and friction) increase in hysteretic streamflow. With these underlying hysteresis characteristics in mind, streamflow hysteresis signals were observed in several scenarios: low bed slopes (Figures 9, 12 and 16), smooth river channels (Figures 8, 13 and 16), and high backwater conditions (Figures 11, 15 and 16). Figure 19 summarizes the impacts of each tested parameter range on the hysteresis severity indicator (V-WSE peak phase timing).

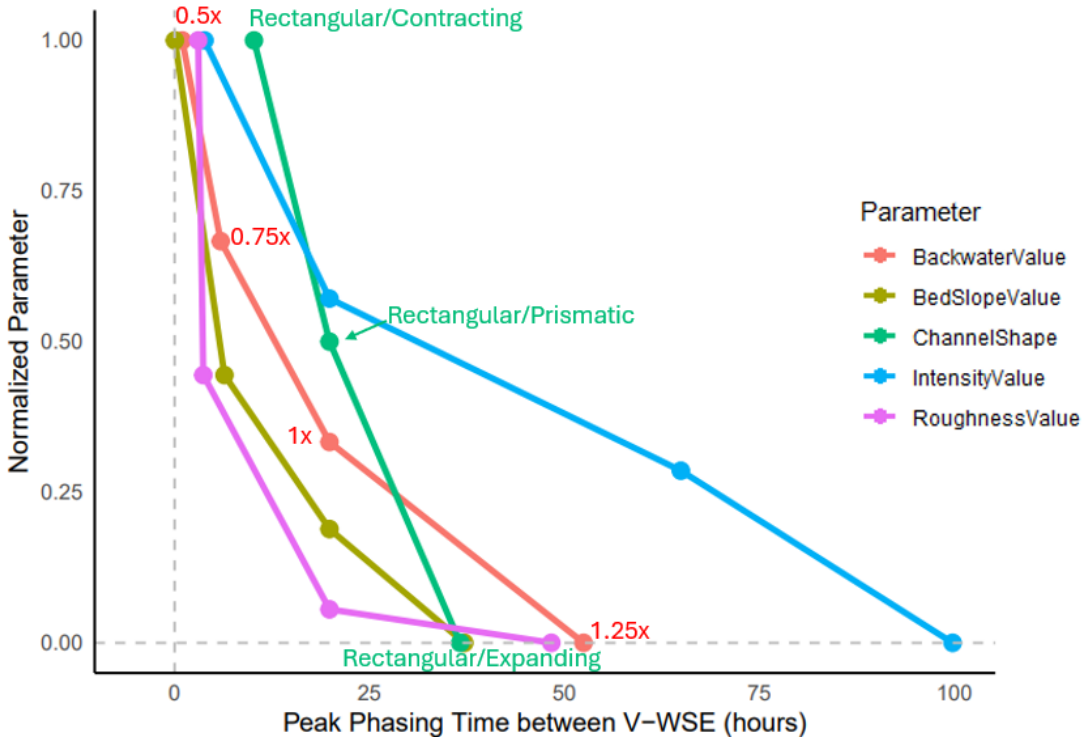

Figure 19: *Summary of impacts to streamflow hysteresis (represented by the peak phase timing between V-WSE) by each of the driving parameters.*

Figure 19 shows the parameters in order of monotonically increasing hysteretic strength: with decreasing bed slope, roughness, and event wave intensity, increasing backwater and expanding river widths, providing insight into the general trends of these parameters. Additionally, the RF analysis (Section 3.1.) pointed specifically to four influential parameters, highlighted in Figure 19 and scatter plots (Section 3.2.): bed slope, roughness, event wave intensity, and backwater condition. A useful companion to Figure 19, a descriptive summary of impacts table, detailing the Froude number, flow variables, and momentum term magnitude-timing relationships with parameter ranges, is presented in the Supplementary Table 6.

As stated earlier and reflected in much of the relevant literature (e.g. Mishra & Singh, 1999; Holmes, 2016; Muste et al., 2020a; Meselhe et al, 2021), the present analysis supports that gentle *bed slope* river channels are natural conduits for streamflow hysteresis. In channels with

low bed slopes, we observed attenuation in the stage hydrograph and a wider hysteresis loop. The behavior exhibits active diffusive and dynamic forces alongside large peak phasing, key factors in sustaining hysteresis. As bed slopes became steeper, pressure gradient and convective acceleration forces diminished, and the hysteresis loop flattened, remaining parallel to the larger, lower, stage-discharge rating curves. Steeper bed slopes were observed to dampen hysteresis signals, with only a very slight signal simulated beyond S_0=0.0005, and the steepest scenario fell consistently on the y-axis of the scatter plots (Figure 9), demonstrating kinematic flow. The local acceleration terms were unchanged between scenarios, since this force only represents progression of the wave in time, but the other momentum terms displayed interesting patterns. These patterns highlighted how bed slope-driven shifts in momentum forces control the strength of hysteresis.

Smoother channels were another strong driver facilitating streamflow hysteresis, exhibited in the positive pressure gradient, negative convective acceleration, and overall peak phasing. There was a rotation and collapsing of the rating curves with increasing roughness. In turn, increasing Manning's *roughness* reduced hysteretic signals in both flow variables and momentum terms, exhibiting lower velocities, opposite pressure gradient and convective acceleration forces, with less peak phasing. This has practical implications for monitoring, suggesting that hysteresis-informed techniques may be especially critical in smoother rivers where roughness plays a smaller role in mitigating hysteresis, or in rivers with significant seasonal vegetation change (which induces a longer-term, temporally-changing hysteresis trend). Since there was a disparity between the two smoother and two rougher scenarios (with a gap from n=0.03 to n=0.1), we observed drastic differences in behavior between them. All of the stage-discharge rating curves remained hysteretic in nature, but they had different shapes: the rougher scenarios were collapsed, flattened loops, and the smoother were robust and rounded loops.

An interesting contrast to note between geometric drivers, illustrated in Figure 20, is how increasing the bed slope can completely collapse the hysteresis signal, while increasing the roughness to a near-maximum value retains some hysteretic signal, unless the slope is steep. Therefore, bed slope may be the more dominant process. Nevertheless, it can be generally concluded that low slope, smooth channels encourage streamflow hysteresis while steep, rough channels behave similarly according to the kinematic conditions.

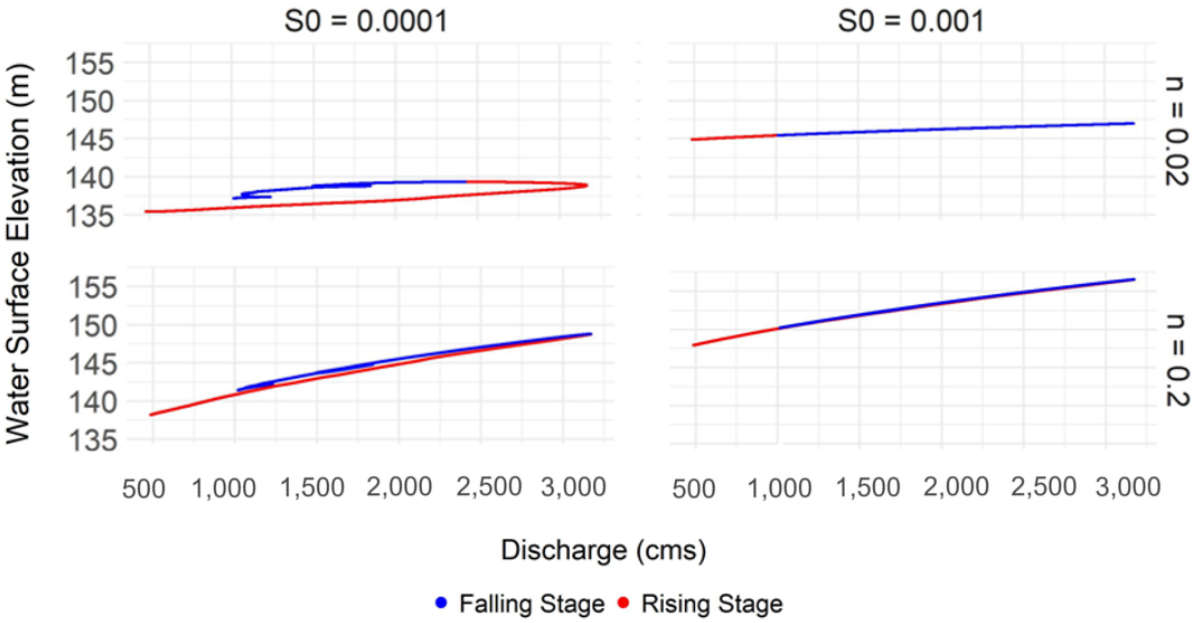

Figure 20: *Matrix of stage-discharge loops for the base flow condition under varied (maximum and minimum values) bed slope and roughness conditions.*

The *event wave intensity* condition, which was revealed to be one of the most important drivers of hysteresis, revealed a hysteresis development direction which at first, seemed to contrast previously reported results in the literature (Mishra & Singh, 1999; Muste et al., 2020a). Commonly, it is stated that intense flows induce hysteresis, but this evidence showed a collapse in the loop shape. With increasing intensity, velocities, kinematic forces, and flow uniformity increased, and there was a rotation (though no translation) and sharpening, particularly at the peak of the hysteresis loop (Figure 14). Notably, the most intense event scenario exhibited very little V-WSE peak phasing, and minor events exhibited a rounder rating curve, thus a greater peak phasing. Furthermore, the hysteretic minor event had a small convective acceleration force, yet a wide range of peak phase timing, and the most intense event scenario was observed with a wide loop, larger convective acceleration magnitude, yet small peak phase timing. With a different approach, using the hysteresis loop area as a hysteresis indicator is another option for developing diagnostics (Mishra & Singh, 1999). By this metric, the most intense event would develop the most hysteresis, aligning with previous studies. Nonetheless, the reduced peak phasing cannot be ignored in the scenarios of intense event waves herein. As we will discuss shortly, this could be due to the nature of the wave or the downstream boundary held constant at the base condition for all of the event intensity scenarios.

The second component of event wave severity, the *event wave shape* condition, had a negligible impact on the hysteresis signal from varied skewness (T_R/T_F). The lack of response in the hysteresis signal with changing event wave shapes may also be because the downstream boundary was changed accordingly (Figure 3c-d), a setup which translates to similar behavior in the simulated wave (Figure 16e). If, instead, the base downstream stage time series was utilized as the boundary condition, there may be more of a change in the loop with differently skewed wave forcing from the upstream flow boundary. The multi-pulse difference in hysteretic signal is an interesting takeaway from the wave shape permutations. As demonstrated in Figure 21 and

further in the Supplementary Material multi-pulse scenarios (Supplementary Figures 11-12, 20-21, and 30-31), it appears that the first pulse was hysteretic, exhibiting phasing in the variables, forming loop shapes, but the second was not. Contrasting hysteretic signals in the momentum terms phasing, and magnitudes were observed between the two pulses as well. Observational evidence supports these initial findings, as in ongoing work by collaborators (Muste, 2025).

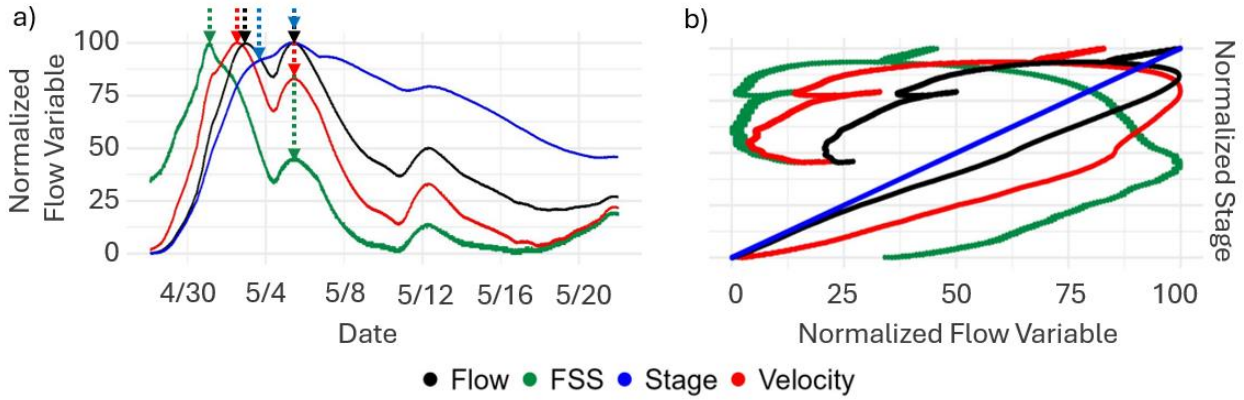

Figure 21: *Model output demonstrating the multi-pulse hysteresis differences: a) normalized flow variable hydrograph time series, and b) normalized stage-flow variable rating curves for the multi-pulse, smooth bed slope scenario.*

All of the findings of the present study may relate to the *backwater conditions* at a river monitoring location. Since the second pulse of the wave was taking place under different backwater conditions than the first, the system had a memory of a prior pulse, and the hysteresis behaved differently (e.g., it became virtually nonexistent). As shown in Figure 21, there was a collapse in the a) peak phasing, and b) stage-flow variable loop. Since the same stage time series was imposed at the downstream of the model, gentle bed slope and smooth channels were forced to slow in water velocity during the recession, forming a hysteresis loop. Similarly, with the event wave intensity relationship to streamflow hysteresis development, the same backwater condition at the downstream for all event wave intensities was imposed, so that more intense events dominate the imposed backwater, misleadingly creating a smaller hysteresis signal in the modeled reach. Effectively, those conditions that produce a water surface lower than the base condition inherently had a backwater effect when the base stage time series was imposed at the downstream boundary of the model. By this fact, the backwater conditions at a site may be the most important driver of streamflow hysteresis. The explicit backwater permutation model results indicate how, with increased backwater conditions, the river channel developed a larger (non-rotated) loop. Lower backwater conditions exhibited little-to-no hysteresis looping and very little peak phase timing, while base and higher backwater conditions had significant phasing. Increasing backwater conditions developed large, positive pressure gradients and large, negative convective acceleration forces, while kinematic terms increased in disparity, as seen in Figure 15. Figure 22 elaborates on this backwater concept and its interaction with dominant geometric parameters by showing a subset of the bed slope-backwater condition permutation scenarios in a profile view.

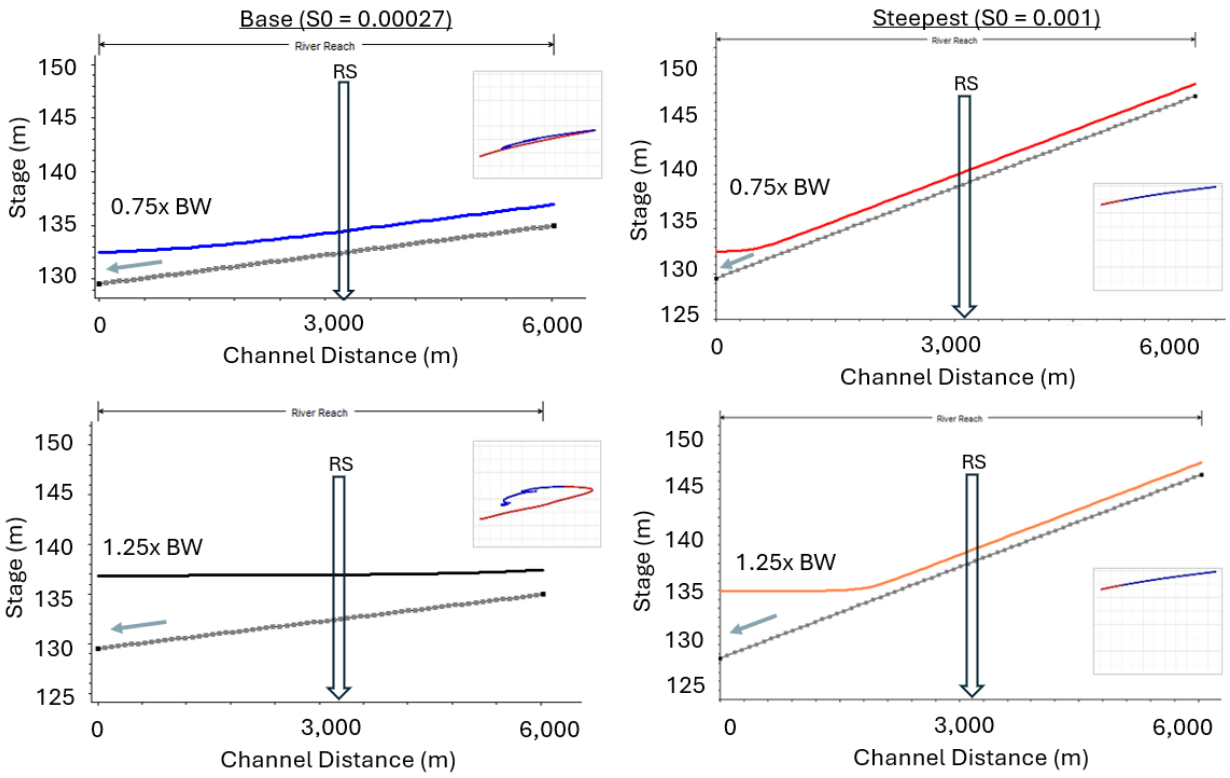

Figure 22: *Profile views for four bed slope-backwater condition permutations taken at time = 0 of the numerical simulations, with "RS" denoting the river station at which the momentum terms are calculated, and current sensitivity analysis is performed, and the corresponding stage-discharge rating curve to the right.*

Increasing the backwater effect did accentuate the loop, as seen most clearly in Figure 22, but if the steep bed slope condition in this example or other factors do not allow, the backwater condition could not develop hysteresis. This finding emphasizes the importance of reach/memory-informed monitoring techniques and using sound boundary conditions for modeling. The *Q-estimation* parameter is a unique case study as it focused more on monitoring and modeling than the explicit physical drivers of streamflow hysteresis (which is why its scenarios were not included in the variable contribution analysis or summary plots). Examined independently in Section 3.4., it was evident that the methods for estimating model boundary conditions are extremely important to hysteresis representation. The HQRC method creates an upstream flow boundary that, when imposed, destroyed the loop throughout the simulation, and even underestimated the peak flow, a critical error in many applications. Meanwhile, the IVRC, Jones and Fenton discharge estimation methods yielded comparable results for both rectangular and compound channels, preserving the loop shape. Furthermore, the IVRC and Fenton accurately estimated the peak flow. The more accurate capture of the flow dynamics can be attributed to the IVRC's inclusion of index velocity in its discharge estimation technique (Muste et al., 2025a). Experiments like this provide useful information and guidance for adopting new streamflow monitoring, modeling, and forecasting methods. Model results indicated that the phasing in the flow variables was persistent under the hysteretic backwater condition imposed, which may offer forecasting opportunities. The phasing that was retained when the model is driven by HQRC, where a small loop does form in the velocity and FSS is phased, was potentially due to the backwater condition employed. Despite this, the IVRC was demonstrated

to be far superior for representing hysteresis in a modeled reach, consistently producing more accurate peak timing, magnitude, and underlying hysteresis momentum characteristics, supporting its use as a more reliable method for driving hydraulic models.

The *normal depth* scenario completely flattened the hysteresis signal, as it used uniform flow assumptions in its calculations (Brunner, 2016). Normal depth creates a flow that is uniform by definition, collapsing any potential hysteresis and rendering the flow kinematic. This evidence may be considered as a warning to hydraulic modelers of how important the backwater condition is to the accurate representation of hysteretic flows. Stage is one of the easiest hydraulic variables to measure and is widely available to those modeling hysteresis; it is also possible to employ its phasing attribute to enhance forecasting rather than defaulting to the normal depth assumption.

The RF analysis indicated that streamflow hysteresis is relatively insensitive to the *channel shape,* yet there were patterns in the momentum terms for expanding and contracting channels. There was an opposite sign behavior in the convective acceleration term, with a contracting channels' positive signal leading to a thinner hysteresis loop and an expanding channels' negative signal leading to a thicker and rotated loop (Supplementary Figure 35). Additionally, as floods involve the floodplains, one must be aware of how hysteretic flow looks like in them, and compound channel impact was found to be an important control on hysteresis. In the compound scenario numerical simulation output, there was a disruption in the momentum terms during the transition from in-channel to floodplain river flow, which manifested as a kinked hysteresis loop. A collapsing and sharpening of the loop were also observed, which may be attributed to the decreased main channel width and phasing in the floodplain, respectively. As consistent Manning n values were utilized to simplify the analysis, natural variation would likely impact the hysteresis further. Rougher floodplains may increase the friction forces and dampen the hysteretic signal, as seen with the roughness scenarios. Nevertheless, this initial analysis on channel shapes confirmed previous studies on expanding/contrasting channels and warrants further exploration of streamflow hysteresis in the floodplains.

The model Froude number analysis for all the sensitivity scenarios demonstrated how hysteresis loops strengthened in opposite directions for various parameter ranges. Fr reflects the combined behavior of hydraulic depth and velocity, two variables that respond differently in hysteretic rivers, reflecting the balance of gravity and inertia. The flow regime where hysteresis manifests can help identify the parameters which develop hysteresis via divergent hydraulic control mechanisms: local or downstream controls. Figure 16 showed that hysteresis forms with smaller Fr, indicating gravity-dominated downstream control with the gradient plots of bed slope, event intensity, and backwater condition parameters. Hysteresis forms with larger Fr in the ranges of roughness and channel shape parameters, indicating inertia-dominated local control. The Fr metric is useful with large batches of simulations, or even experimental data, providing a universal, relatively easily measurable, dimensionless metric for diagnosing the streamflow.

5. Conclusions

A detailed exploration of the St Venant terms during a hysteretic cycle for a range of river conditions revealed the important drivers of streamflow hysteresis by uncovering system physics. Streamflow hysteresis developed in both low and medium Froude number ranges, as it

is controlled by both local and backwater effects, depending on the driving parameter (i.e., roughness is a local mechanism and bed slope is a downstream control). Through the scenarios in Table 1, hysteresis was parameterized for a broad range of flow conditions. The detailed analysis of the momentum terms represents a novel diagnostic approach to understanding hysteresis. Unlike traditional empirical descriptors, this method provides a multi-dimensional, time-varying insight into the physical forces at play, offering a more quantitative view of hysteresis mechanisms.

A statistical analysis revealed that hysteresis is controlled 28% by event wave intensity, 23% bed slope, 16% Manning's roughness, and 15% backwater condition. This study examined hysteresis developing in conditions with gentle bed slopes (S_0<0.0005), smooth roughness values (n<0.1), expanding channels, the first peak of some multi-pulse waves, and generally higher backwater conditions (FSS<S_0). Results indicate that *bed slope* is the most persistent and perhaps strongest control on the expression of hysteresis, with gentle bed slopes consistently generating strong hysteretic signals, characterized by wide loop shapes and significant lags in the peak timing. Under these low slope conditions, pressure gradient and convective acceleration forces became active and imbalanced, consistent with diffusive wave behavior. As bed slope increased, these forces diminished, hysteresis loops collapsed, and flow behavior shifted toward the kinematic wave regime. Steep-sloped scenarios showed minimal or no discernible hysteresis, indicating that slope alone can regulate the presence or absence of these dynamics. Channel *roughness* also played a critical role, with smooth channels amplifying hysteresis, supporting strong momentum terms and clear peak phasing, while rough channels suppressed it. Rougher conditions produce flatter loop shapes, slower velocities, and reversed momentum signals, which point to the importance of temporal and spatial variations in roughness (e.g., due to vegetation) in shaping hysteretic behavior.

Event *wave intensity* had more nuanced effects, as high-intensity floods produced large hysteresis loops but did not necessarily amplify hysteresis at the event peaks. Instead, low-intensity events generated longer peak lags, likely because high-intensity flows overwhelmed the backwater influence that supports hysteresis development. *Backwater effects*, influenced by downstream boundary conditions, emerged as another critical driver. When backwater conditions were strong, whether in the specific backwater scenario permutations or as a result of other parameter setups, hysteresis was more pronounced. This highlights the sensitivity of hysteresis to boundary conditions and supports the idea that rivers can retain a form of hydraulic memory over the course of an event with backwater presence. For *channel shape*, increasing river width slightly enhanced hysteresis severity, likely by increasing storage capacity and temporal lag of flow variables. Compound cross sections caused a bend in the looped rating curves when hysteresis was present. For the event *wave shape*, the skewness (i.e., differing time to rise and fall) had little impact on hysteresis under constant downstream conditions. However, scenarios with multi-pulse waves showed that hysteresis can vary between pulses: the first pulse often produced strong hysteresis, while the second pulse did not. This suggests that the backwater context and hydraulic conditions set by previous flow events can govern whether hysteresis appears during subsequent peaks.

This diagnostic framework can serve as a foundation for further studies and to guide the development of enhanced monitoring and forecasting tools. The ability to identify the wave type under specific site and flow conditions is critical for determining the appropriate monitoring

method. For example, with the present analysis analyzing the hydro-morphological characteristics and historical records at a monitoring station, we can determine the type of flow and obtain this guidance for monitoring sites. If hysteretic conditions are present, discharge estimation alternatives to the traditional HQRC methods should be considered. It is increasingly feasible to measure the diffusive and dynamic variables that are active in hysteretic streamflow with new monitoring technology. For example, low-cost pressure transducers can continuously monitor dynamic water surface slopes to capture FSS for the CSA method (Lee et al., 2017). Using *Q estimation methods* such as the IVRC and avoiding the ND model setup are suggestions from the results of this study, as they allow for the accurate representation of hysteresis. In turn, this can improve models by implementing physics learned through more accurate model input data and methods.

The results of this study and previous observational studies also can reveal future directions for exploration and further understanding of hysteresis drivers. Other trials that could be run to expand this set of permutations include a multi-pulse storm with the first pulse occurring on the rising limb so that the second is the main peak. This is a more naturally occurring hydrograph shape as seen in the Henry, IL gage historical record and may reveal different hysteresis patterns for multi-pulse storms. It would also be interesting to explore further the31ffectts of channel cross-section shape scenarios, particularly compound channels with floodplains, variations in channel aspect ratio, and differential roughness between the main channel and floodplains. It is in the best interest of the hydraulic monitoring community to fully explore a range of multi-pulse storms and compound channels, as these are the realistic conditions that need to be monitored. For example, exploring flood intensities with a more realistic backwater, rather than maintaining the base backwater condition, would be a significant expansion of this study.

Notably, the in-depth parameterization of streamflow hysteresis may also open the door to more physics-based forecasting strategies. For example, the water free-surface slope (FSS) and local acceleration terms peaking first in hysteretic reaches can be great predictors for Machine Learning (ML) streamflow forecasting algorithms, having the potential to be used as a "flag" to predict the flood crest arrival time and magnitude. As explored in House et al., (2025c) and demonstrated with actual data by Muste et al (2022), the FSS can be accurately monitored quite easily. Since many streams are hysteretic, they inherently present an additional monitoring challenge as well as a potential hidden forecasting benefit.

Data Availability Statement

The code and supporting data can be found at https://github.com/ehouse25.

Acknowledgements

- This paper is based upon work supported by the National Science Foundation under Grant No. 2139663
- We would like to thank Chris Goodell for the foundational work with the development of the HEC-RAS Controller and guidance in adapting it for our application.

References

Aricò, C., Nasello, C., & Tucciarelli, T. (2009). Using unsteady-state water level data to estimate channel roughness and discharge hydrograph. *Advances in Water Resources*, *32*(8), 1223-1240. https://doi.org/10.1016/j.advwatres.2009.05.001

Baldassarre G Di, Montanari A (2009) Uncertainty in river discharge observations: a quantitative analysis. Hydrology and Earth System Sciences, 13(6):913–921. https://doi.org/10.5194/hess-13-913-2009

Brown, S. C., Lester, R. E., Versace, V. L., Fawcett, J., & Laurenson, L. (2014). Hydrologic landscape regionalisation using deductive classification and random forests. PLoS One, 9(11), e112856.

Brunner, G. W. (2016). HEC-RAS river analysis system: hydraulic reference manual, version 5.0. US Army Corps of Engineers–Hydrologic Engineering Center, 547.

Cheng, Z., Lee, K., Kim, D., Muste, M., Vidmar, P., & Hulme, J. (2019). Experimental evidence on the performance of rating curves for continuous discharge estimation in complex flow situations. *Journal of Hydrology*, 568, 959-971. doi:10.1016/j.jhydrol.2018.11.021

Chow, V. T. (1959). Open channel flow. London: McGRAW-HILL, 11(95), 99,136-140.

Crago, R. D., & Richards, S. M. (2000). Nonkinematic effects in storm hydrograph routing. Journal of Hydrologic engineering, 5(3), 323-326.

De Saint-Venant, B. (1871). Theorie du mouvement non-permanent des eaux avec application aux crues des rivers et a l'introduntion des Marees dans leur lit. Academic de Sci. Comptes Redus, 73(99), 148-154.

Dottori, F., Martina, M. L. V., and Todini, E. (2009). A dynamic rating curve approach to indirect discharge measurement, Hydrol. Earth Syst. Sci., 13, 847–863, https://doi.org/10.5194/hess-13, pp. 847-2009.

Eames, I., & Hunt, J. C. R. (1997). Inviscid flow around bodies moving in weak density gradients without buoyancy effects. Journal of Fluid Mechanics, 353, 331-355.

Faye, R. E., & Cherry, R. N. (1980). Channel and dynamic flow characteristics of the Chattahoochee River, Buford Dam to Georgia Highway 141 (No. 2063). US Govt. Print. Off.

Fenton, J. D., & Keller, R. J. (2001). The calculation of streamflow from measurements of stage: CRC for Catchment Hydrology.

Fenton, J. D. (2001). Rating curves: Part 1 - Correction for surface slope, in Proc. Conf. on Hydraulics in Civil Engng, 28-30 Nov., Inst. Engnrs, Aust., Hobart, pp. 309-317.

Ferrick, M. G. (1985). Analysis of river wave types. *Water Resources Research*, 21(2), 209-220. doi:10.1029/WR021i002p00209

Fread, D. L. (1975). Computation of Stage-Discharge Relationships Affected by Unsteady Flow. *Journal of the American Water Resources Association*, 11(2), 213-228. doi:10.1111/j.1752-1688.1975.tb00674.

Goodell, C. (2014). Breaking the Hec-Ras Code: A User's Guide to Automating Hec-Ras. H21s.

Graham, M. H., & Edwards, M. S. (2001). Statistical significance versus fit: estimating the importance of individual factors in ecological analysis of variance. *Oikos*, *93*(3), 505-513.

Heldmyer, A., Livneh, B. McCreight, J., Read, L. Kasprzyk, J. Minear T. (2022). Evaluation of ne observationally based channel parameterization for the Nation Water Model, Hydrol. Earth Syst. Sci, 26, pp 6121-6136, https://doi.org/10.5194/hess-26-6121-2022

Henderson, F.M. (1966). Open Channel Flow. Macmillan Series in Civil Engineering; Macmillan Company: New York, NY, USA, p. 522

Holmes R (2016) River rating complexity. River Flow 2016, :679–686. https://doi.org/10.1201/9781315644479-107

House, E., Meselhe, E., Muste, M., and Demir, I. (2025a). Streamflow Hysteresis Analysis through a Deep Dive Budget of the St Venant Momentum Terms. arXiv preprint arXiv: https://doi.org/10.31223/X5W44C.

House, E., Kim, K., Muste, M., Meselhe, E., and Demir, I. (2025b). Back to Basics: On the Proper Determination of Free-Surface Slope (FSS) in Gradually Varied Open Channel Flows. arXiv preprint arXiv: https://doi.org/10.31223/X50X5M.

Knight, D.W. (2005). River flood hydraulics: validation issues in one-dimensional flood routing models.

Lee, Patricia, & Gregory E. Granato. (2012). Prepared in cooperation with the Department of Transportation Federal Highway Administration Office of Project Development and Environmental Review Estimating Basin Lagtime and Hydrograph-Timing Indexes Used to Characterize Stormflows for Runoff-Quality A. https://pubs.usgs.gov/sir/2012/5110/pdf/sir2012-5110_text.pdf

Lee K (2013) Evaluation of methodologies for continuous discharge monitoring in unsteady open-channel flows. Ph. D. Dissertation, The Univesity of Iowa, Iowa City, Iowa. http://ir.uiowa.edu/etd/5012

Lee, K., Firoozfar, A. R., and Muste, M (2017) Technical Note: Monitoring of unsteady open channel flows using the continuous slope-area method, Hydrol. Earth Syst. Sci., 21, 1863–1874, https://doi.org/10.5194/hess-21-1863-2017

Levesque, V. A. and Oberg, K. A. (2012). Computing discharge using the index velocity method: US Department of the Interior, US Geological Survey.

McCuen, R. H. (1989). Hydrologic analysis and design (pp. 143-147). Englewood Cliffs, NJ: Prentice-Hall.

Meselhe, E.A. and Holly, F.M. Jr. (1997) "Invalidity of the Preissmann Scheme for Transcritical Flow," Journal of Hydraulic Engineering, ASCE, vol. 123(7). doi:10.1061/(ASCE)0733-9429(1997)123:7(652)

Meselhe, E., Lamjiri, M. A., Flint, K., Matus, S., White, E. D., & Mandli, K. (2021). Continental scale heterogeneous channel flow routing strategy for operational forecasting models. *Journal of the American Water Resources Association*, 57(2), 209-221. doi:10.1111/1752-1688.12847

Mishra, S. K., & Singh, V. P. (1999). Hysteresis-based flood wave analysis. Journal of Hydrologic Engineering, 4(4), 358-365.

Muste, M., Bacotiu, C., & Thomas, D. (2019). Evaluation of the slope-area method for continuous streamflow monitoring. In Proceedings of the 38th IAHR World Congress (pp. 121-130). doi:10.3850/38WC092019-1860

Muste, M., Kim, D. and Kim, K. (2022). A flood-crest forecast prototype for river floods using only in-stream measurements, Communications Earth & Environment, https://doi.org/10.1038/s43247-022-00402-z

Muste, M. and Demir, I, (2024). Developing a Novel Hybrid Streamflow Monitoring System (HyGage), Partnership for Innovation, National Science Foundation call NSF-23-538, (proposal submitted to NSF in May, 2024)

Muste, M., Lee, K., Kim, D., Bacotiu, C., Rojas Oliveros, M., Cheng, Z. and Quintero, F. (2020a). "Revisiting Hysteresis of Flow Variables in Monitoring Unsteady Streamflows" State-of-the-art Paper Series, Journal of Hydraulic Research; 58(6), pp. 867-887, https://doi.org/10.1080/00221686.2020.1786742

Muste, M., Kim, K., Kim, D., and Demir, I. (2025a). Comparative Analysis of the Stage-Discharge Rating Operated in Gradual Varied Flows with Alternative Streamflow Monitoring Approaches. arXiv preprint arXiv: https://doi.org/10.31223/X52Q7X.

Muste, M., & Kim, D. (2020b). Augmenting the Operational Capabilities of SonTek/YSI Streamflow Measurement Probes. Sontek/YSI-IIHR Collaborative Research Report. Available online: https://info.xylem.com/rs/240-UTB- 46/images/augmentingcapabilities-sontek-probe.pdf.

Muste, M., Kim, D. and Kim, K. (2022a). A flood-crest forecast prototype for river floods using only in-stream measurements, Communications Earth & Environment, https://doi.org/10.1038/s43247-022-00402-z

Muste, M., Kim, D., & Kim, K. (2022b). Insights into flood wave propagation in natural streams as captured with Acoustic Profilers at an index-velocity gaging station. *Water*, 14(9), 1380. doi:10.3390/w14091380

Muste, M., Kim, D., & Kim, K. (2025b). Where and when should we be concerned about flow hysteresis?. In River Flow 2024 (pp. 804-808). CRC Press.

NOAA. (2022). Illinois River near Henry. Noaa.gov. https://water.noaa.gov/gauges/05558300

Rantz, S.E., et al., (1982). Measurement and Computation of Streamflow: Volume 2. Computation of Discharge," Water-Supply Paper 2175, U.S. Geological Survey, pp. 285-631

Rátky, I. (2000). Árvízi hurokgörbék közelítő számítása, Vízügyi Közlemények 82(2), pp. 232-261. (in Hungarian)

Schmidt, A.R., (2002). Analysis of stage-discharge relations for open-channel flows and their associated uncertainties, Ph.D. Thesis, University of Illinois at Urbana-Champaign, Department of Civil and Environmental Engineering, 349 p.

Schmidt, A. R. and Garcia, M. H. (2003). Theoretical Examination of Historical Shifts and Adjustments to Stage-Discharge Rating Curves. In P. Bizier, & P. DeBarry (Eds.), World Water and Environmental Resources Congress (pp. 1089-1098). (World Water and Environmental Resources Congress), DOI:10.1061/40685(2003)233.

Simon, S.M., Glaum, P. & Valdovinos, F.S. (2023). Interpreting random forest analysis of ecological models to move from prediction to explanation. *Sci Rep* **13**, 3881. https://doi.org/10.1038/s41598-023-30313-8.

Zhang, Q., Li, Y. P., Huang, G. H., Wang, H., & Shen, Z. Y. (2024). Bayesian analysis of variance for quantifying multi-factor effects on drought propagation. Journal of Hydrology, 632, 130911.

Zuecco, G., Penna, D., Borga, M. A. R. C. O., & van Meerveld, H. J. (2016). A versatile index to characterize hysteresis between hydrological variables at the runoff event timescale. Hydrological Processes, 30(9), 1449-1466.

Supplementary Materials for Sensitivity Analysis

Supplementary Equations

$$\frac{\partial Q}{\partial x} + \frac{\partial A}{\partial t} = 0 \tag{1}$$

$$\frac{\partial Q}{\partial t} + \frac{\partial}{\partial x}\left(\frac{Q^2}{A}\right) + gA\frac{\partial y}{\partial x} - gA\left(S_0 - S_f\right) = 0 \tag{2}$$

where Q is discharge, A is cross-sectional area, V is average velocity, x is distance along the channel, y is water depth, t is time, g is the gravity constant, S_0 is bed slope, and S_f is friction slope.

$$Fr = \frac{V}{\sqrt{gy}} \tag{3}$$

where Fr is the Froude number, V is average velocity, g is the gravity constant, and y is water depth.

Supplementary Results

This section contains the results of all the sensitivity analysis scenarios. Along with the variable importance analysis results and summary of impacts table, included herein are the flow variable and momentum term time series, normalized time series, and bivariate loop plots for all parameter permutations. These results are grouped in matrices to visualize the impacts of all the different parameter ranges and combinations.

Tables 1-5: Variable Importance analysis supporting tables
- a. ANOVA Residual error statistics
- b. Analysis of Variance Table
- c. ANOVA coefficients
- d. Random Forest performance table
- e. Random Forest variable importance table

Table 6: Summary of impacts table

Figs 1-2: Discharge Estimation Method Permutations (all)
- a. Flow and Stage hydrographs
- b. Stage-discharge rating curves

Figs 3-4: Roughness x Event Intensity Permutations

Figs 5-6: Roughness x Skewed Event Intensity Permutations

Figs 7-8: Roughness x Normal Depth Permutations

Figs 9-10: Roughness x Backwater Permutations

Figs 11-12: Roughness x Hydrograph Shape Permutations

Figs 13-24: Bed Slope x Event Intensity Permutations

Figs 15-16: Bed Slope x Skewed Event Intensity Permutations
Figs 17-18: Bed Slope x Normal Depth Permutations
Figs 19-20: Bed Slope x Backwater Permutations
Figs 21-22: Bed Slope x Hydrograph Shape Permutations
Figs 23-24: Channel Shape x Event Intensity Permutations
Figs 25-26: Channel Shape x Skewed Event Intensity Permutations
Figs 27-28: Channel Shape x Normal Depth Permutations
Figs 29-30: Channel Shape x Backwater Permutations
Figs 31-32: Channel Shape x Hydrograph Shape Permutations
Figs 33-34: Roughness x Bed Slope combinations for base event scenario
Figure 35: Gradient plot for the channel shape permutations

Table 1: Residual error statistics for the ANOVA analysis for most of the driver parameters with V-WSE as the response variable.

```
Residual standard error: 17.69 on 198 degrees of freedom
Multiple R-squared:  0.6173,    Adjusted R-squared:  0.5844
F-statistic: 18.78 on 17 and 198 DF,  p-value: < 2.2e-16
```

Table 2: Sequential Analysis of Variance table for most of the driver parameters with V-WSE as the response variable, indicating the significance of each driver.

```
Analysis of Variance Table

Response: Time_V
                    Df Sum Sq Mean Sq F value    Pr(>F)
BedSlopeCondition    4  24871  6217.8 19.8762 8.992e-14 ***
RoughnessCondition   3  24200  8066.7 25.7864 3.995e-14 ***
Floodwaveshape       1    397   396.6  1.2677 0.2615698
FloodwaveIntensity   3  40813 13604.5 43.4887 < 2.2e-16 ***
BackwaterCondition   4   7729  1932.3  6.1767 0.0001054 ***
Channelshape         2   1885   942.3  3.0120 0.0514509 .
Residuals          198  61940   312.8
---
Signif. codes:  0 '***' 0.001 '**' 0.01 '*' 0.05 '.' 0.1 ' ' 1
```

Table 3: ANOVA coefficients for values of the driver parameters with V-WSE as the response variable, indicating the most significant parameter values.

```
Coefficients:
                                  Estimate Std. Error t value Pr(>|t|)
(Intercept)                          5.337      6.481   0.823 0.411243
BedSlopeConditionMild (S0=0.0001)    2.565      3.610   0.710 0.478266
BedSlopeConditionSteep (S0=0.0005) -12.603      3.610  -3.491 0.000594 ***
BedSlopeConditionSteep (S0=0.001)   -7.055      6.253  -1.128 0.260614
BedSlopeConditionSteepest (S0=0.001) -28.971    3.991  -7.258 8.71e-12 ***
RoughnessConditionRough (n=0.1)     -15.764     3.610  -4.366 2.03e-05 ***
RoughnessConditionRougher (n=0.2)   -23.413     3.991  -5.866 1.85e-08 ***
RoughnessConditionSmooth (n=0.02)    6.426      3.610   1.780 0.076610 .
FloodwaveShapeSkewed                -4.864      2.948  -1.650 0.100546
FloodwaveIntensityIntense Flood     -8.307      4.169  -1.993 0.047664 *
FloodwaveIntensityLow Intensity     10.444      4.169   2.505 0.013039 *
FloodwaveIntensityMinor Flood       32.224      4.169   7.730 5.31e-13 ***
BackwaterCondition0.75x BW           2.914      5.896   0.494 0.621682
BackwaterCondition1.25x BW          24.018      5.896   4.074 6.69e-05 ***
BackwaterConditionBase Flood        14.239      5.314   2.679 0.007995 **
BackwaterConditionNormal Depth       2.482      5.896   0.421 0.674170
ChannelShapeRectangular/Expanding   17.478      7.221   2.421 0.016401 *
ChannelShapeRectangular/Prismatic   10.755      6.136   1.753 0.081198 .
---
Signif. codes:  0 '***' 0.001 '**' 0.01 '*' 0.05 '.' 0.1 ' ' 1
```

Table 4: Random Forest performance evaluation, indicating the percent variance explained by the Random Forest model.

```
Call:
 randomForest(formula = Time_V ~ ., data = df_rf, importance = TRUE)
               Type of random forest: regression
                     Number of trees: 500
No. of variables tried at each split: 2

          Mean of squared residuals: 174.6564
                    % Var explained: 76.69
```

Table 5: Random Forest variable importance table for most of the driver parameters with V-WSE as the response variable, indicating the significance of each driver.

	%IncMSE	IncNodePurity
BedSlopeCondition	35.218592	30281.441
RoughnessCondition	40.238381	30529.883
ChannelShape	1.191455	5763.810
FloodwaveShape	-7.260232	2674.613
FloodwaveIntensity	41.006127	43514.710
BackwaterCondition	25.012420	14232.631

Table 6: Summary of impacts to streamflow hysteresis as indicated in the momentum terms and flow variables, for each parameter in our sensitivity analysis. The parameters and characteristics are colored red for decreasing hysteresis signal and green for increasing hysteresis signal.

Parameter	Impact on Hysteresis (*Response: peak phasing time from V-WSE*)								
..and direction of change for impact	Fr	kin	gAS0	gASf	gA(dy/dx)	d(QV)/dx	Q	V	FSS
Increasing Bed Slope	↑ mag & ↓ timing	↑ mag & ↓ timing	↓ mag & ↓ timing	misc. mag & ↓ timing	↓ mag & ↓ timing	gen. ↓ mag & ↓ timing	= mag & ↓ timing	↓ mag & ↓ timing	↑ mag & ↓ timing
Increasing Roughness	↓ mag & ↓ timing	↑ mag & ↓ timing	↑ mag & ↓ timing	↑ mag & ↓ timing	↓ mag & ↑ timing	↓ mag & ↓ timing	= mag & ↓ timing	misc. mag & ↓ timing	= mag & ↓ timing
(nondirectional) Wave Shape	Generally, not much change with skewing, but multi-pulse waves show an interesting difference in hysteresis signal for each pulse (first hysteretic, second non-hysteretic), and MP are in scatter plots with large timing diffs								
Increasing Wave Intensity	↑ mag & ↓ timing	↑ mag & ↓ timing	↑ mag & ↓ timing	↑ mag & ↓ timing	= mag & ↑ timing	↑ mag & ↓ timing	↑ mag & ↓ timing	↑ mag & ↓ timing	= mag & ↓ timing
Increasing Backwater Effect	= mag & ↑ timing	↑ mag & ↑ timing	not much change...	= mag & ↑ timing	↑ mag & = timing	= mag & ↑ timing	N/A	= mag & ↑ timing	= mag & ↑ timing
(nondirectional) Channel shape	Generally, not much change with channel shape, expanding increases the loop (negative convective acceleration) while contracting decreases it (positive convective acceleration)... compound shape puts a kink in the loop but preserves hysteresis...								
More dynamic Q Estimation	ND entirely collapses the loop, HQRC misses loop too, but some forces remain active potentially due to backwater, IVRC captures the loop, phasing, and hysteretic mom term patterns, Johns & Fenton too								

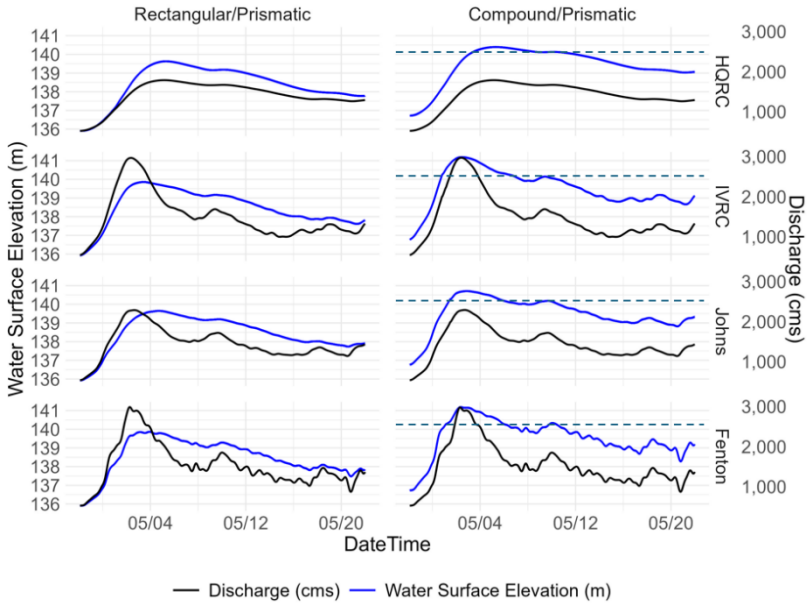

Figure 1: Flow and stage hydrographs for the discharge estimation method permutations (all) and two prismatic channel shape scenarios.

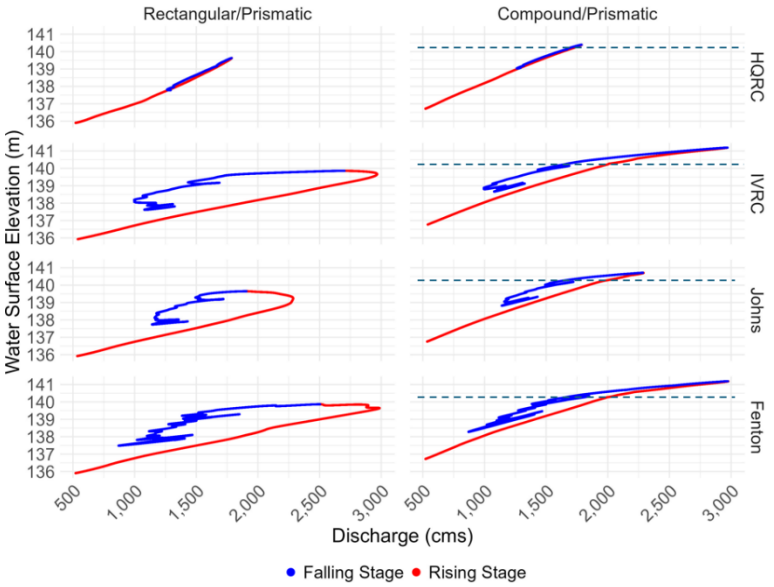

Figure 2: Stage-discharge loop rating curves for the discharge estimation method permutations (all) and two prismatic channel shape scenarios.

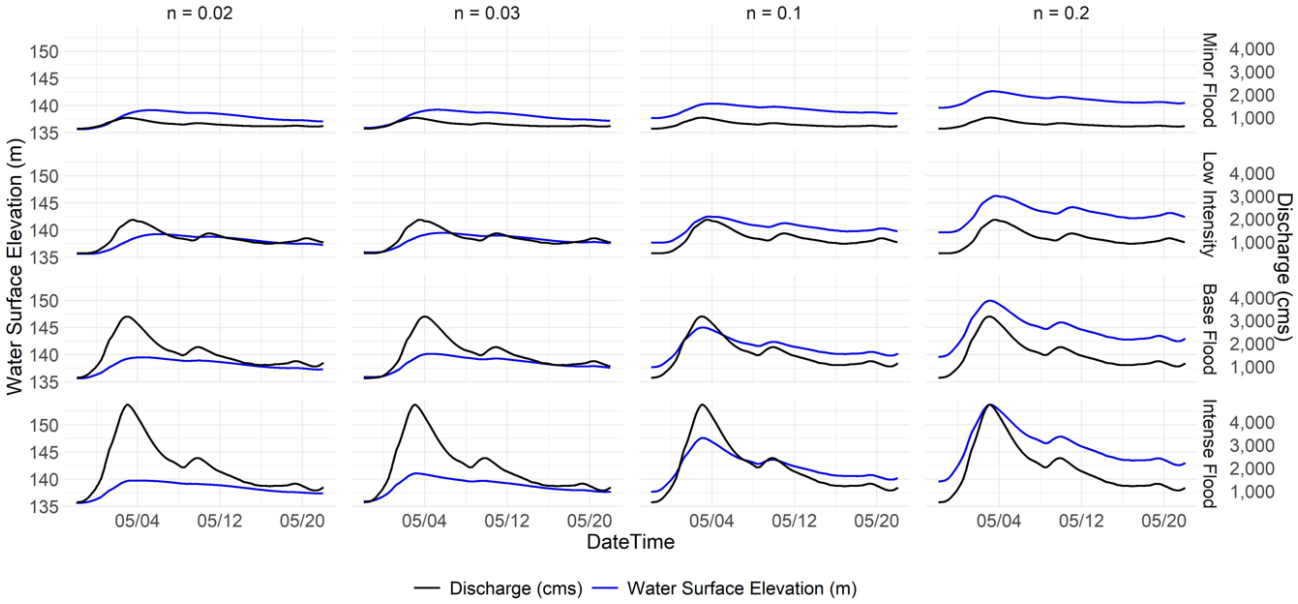

Figure 3: Flow and stage hydrographs for the roughness-event intensities permutations.

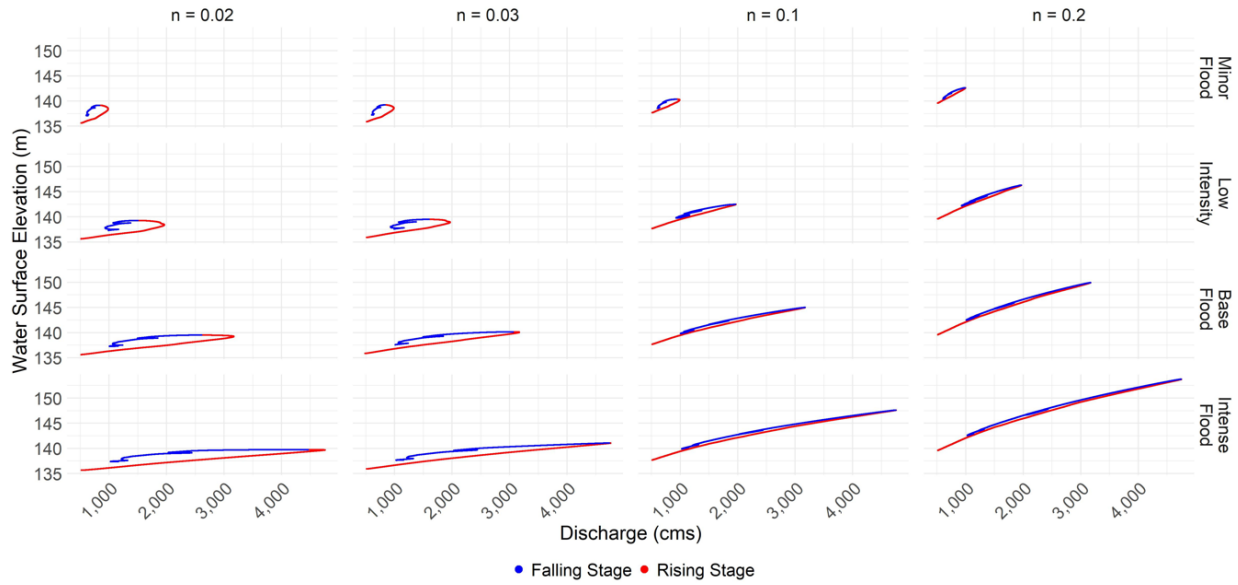

Figure 4: Stage-discharge loop rating curves for the roughness-event intensities permutations.

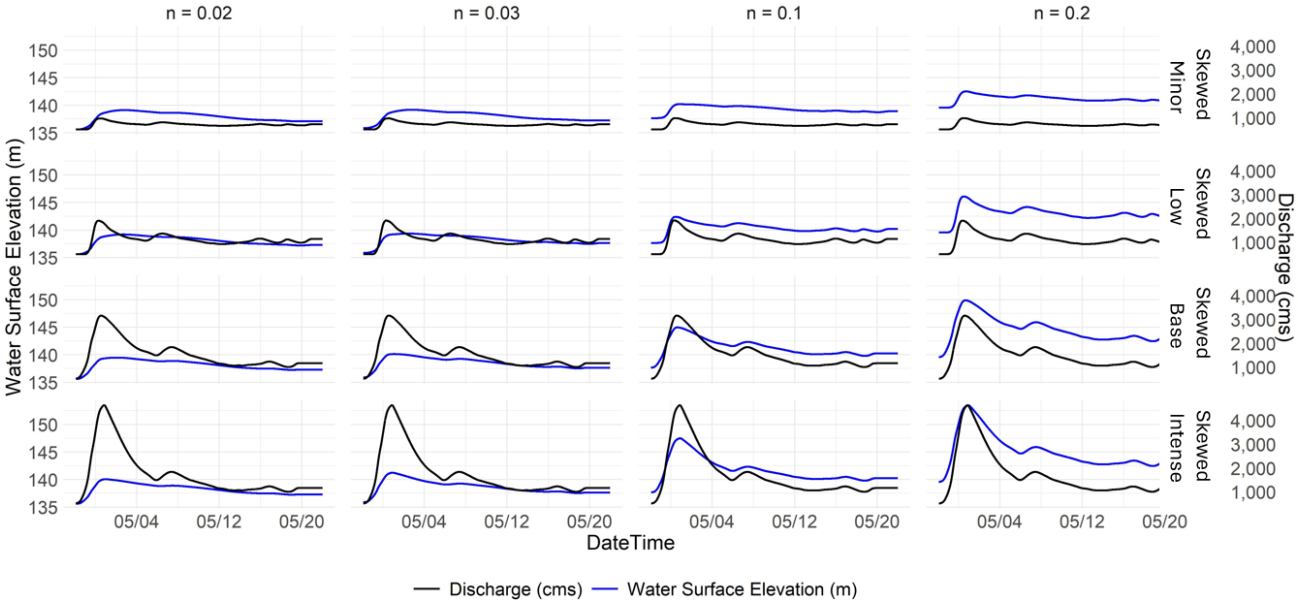

Figure 5: Flow and stage hydrographs for the roughness-skewed event intensities permutations.

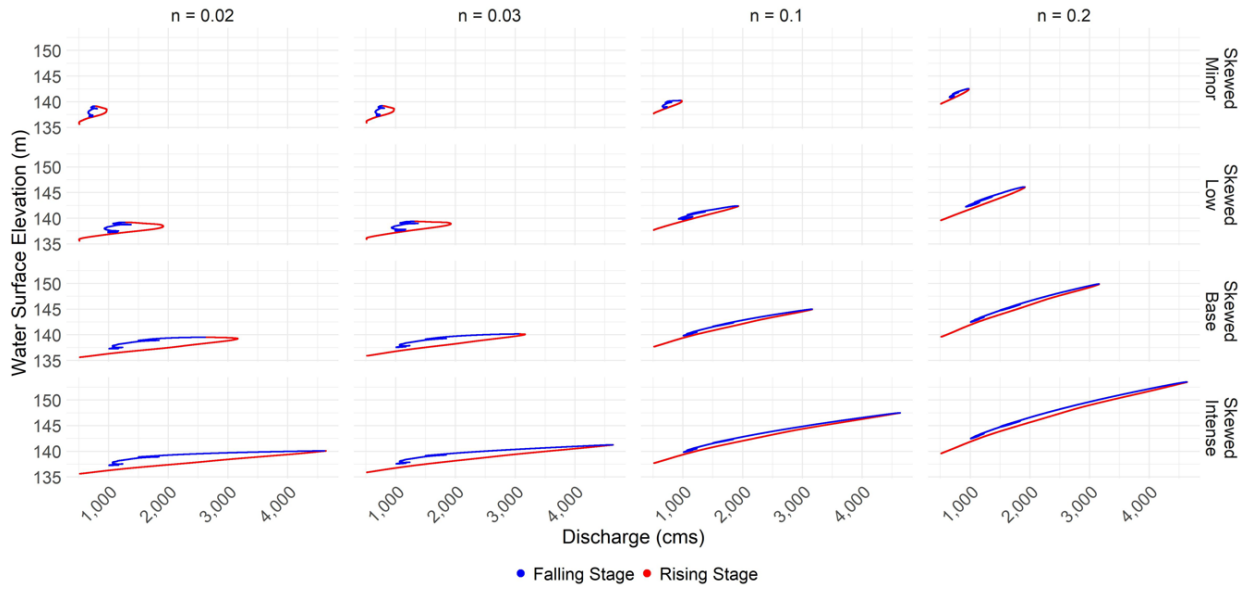

Figure 6: Stage-discharge loop rating curves for the roughness-skewed event intensities permutations.

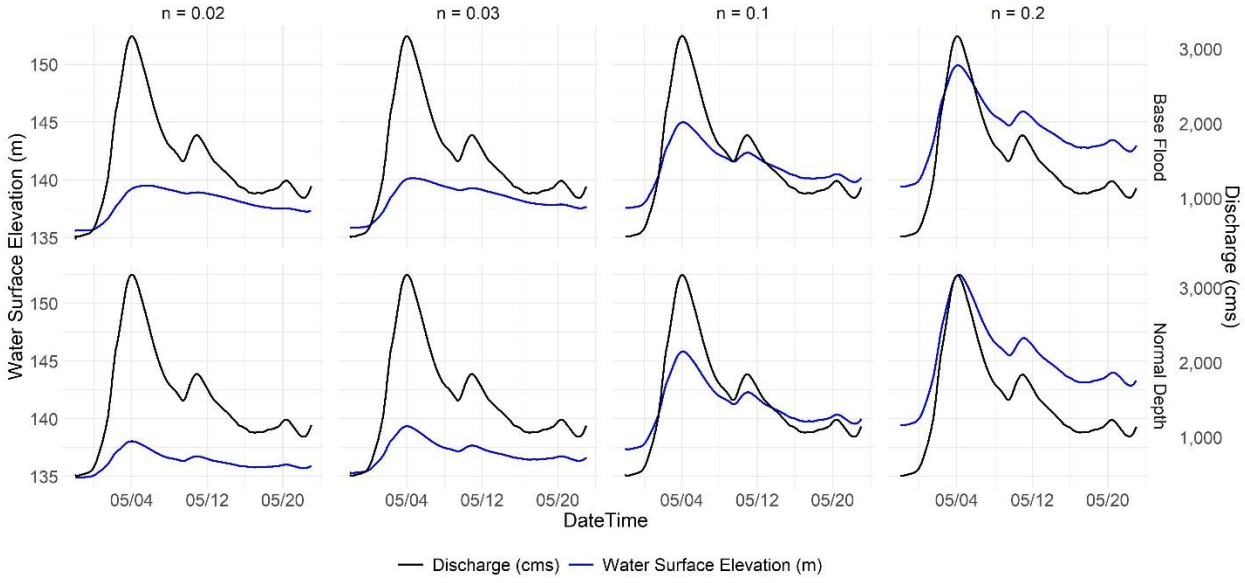

Figure 7: Flow and stage hydrographs for the roughness-normal depth permutations.

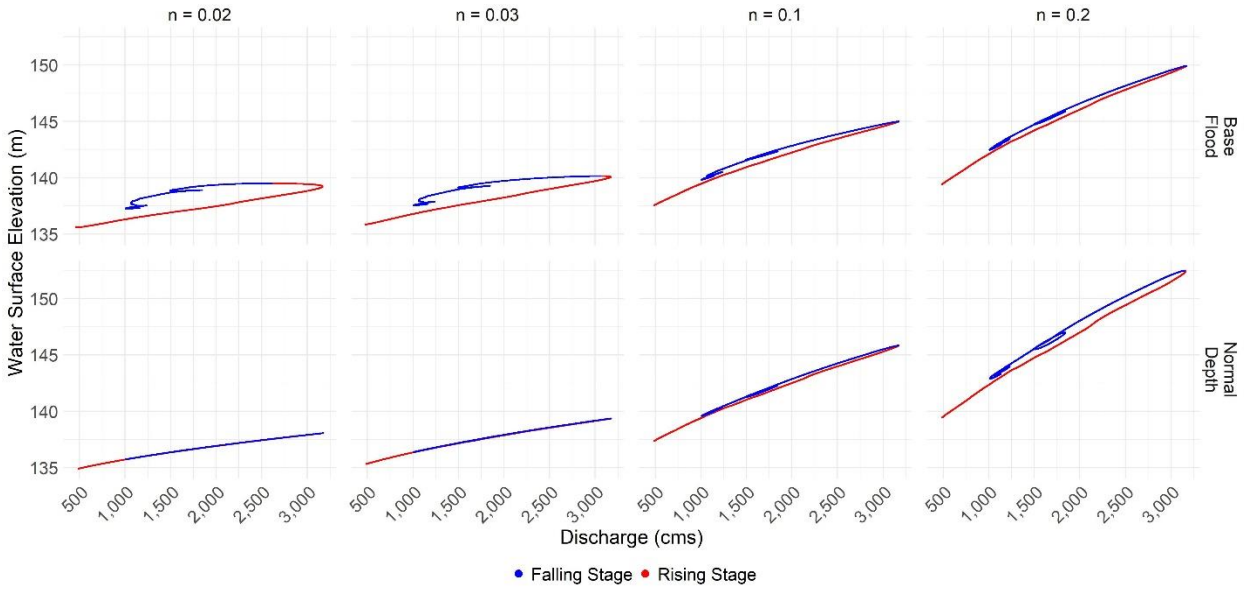

Figure 8: Stage-discharge loop rating curves for the roughness-normal depth permutations.

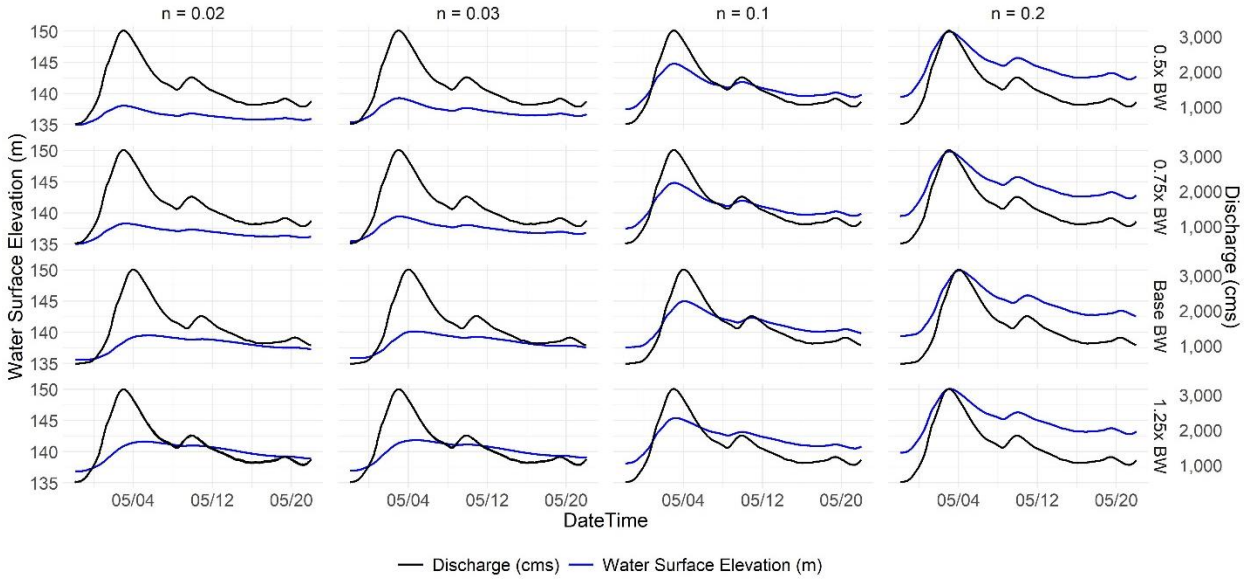

Figure 9: Flow and stage hydrographs for the roughness-backwater permutations.

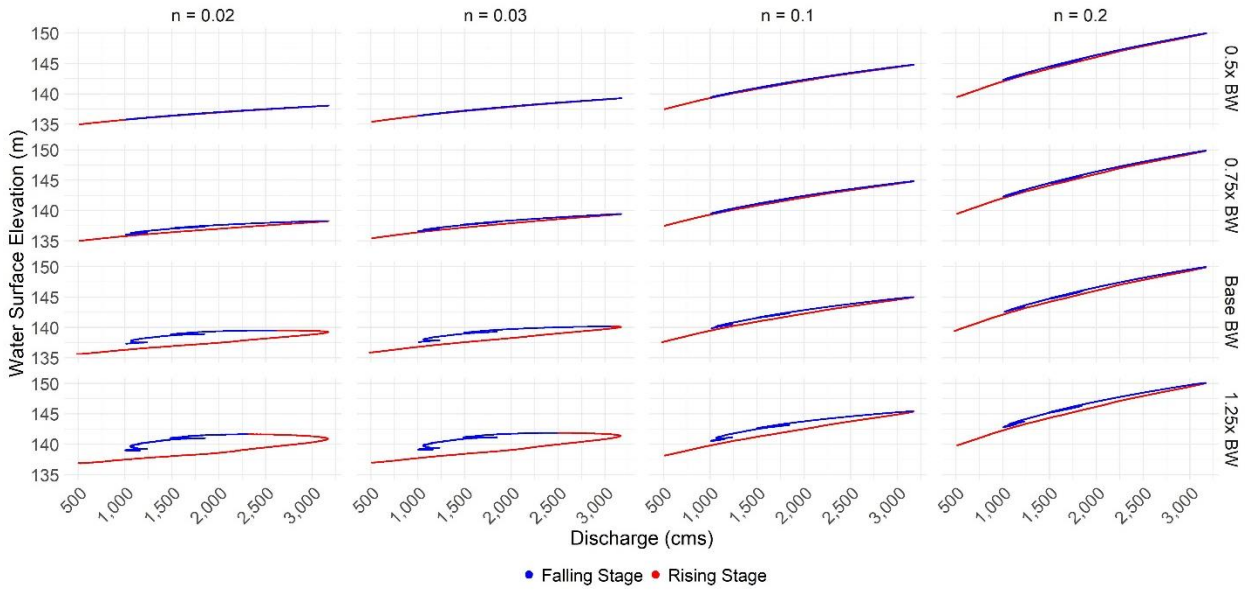

Figure 10: Stage-discharge loop rating curves for the roughness-backwater permutations.

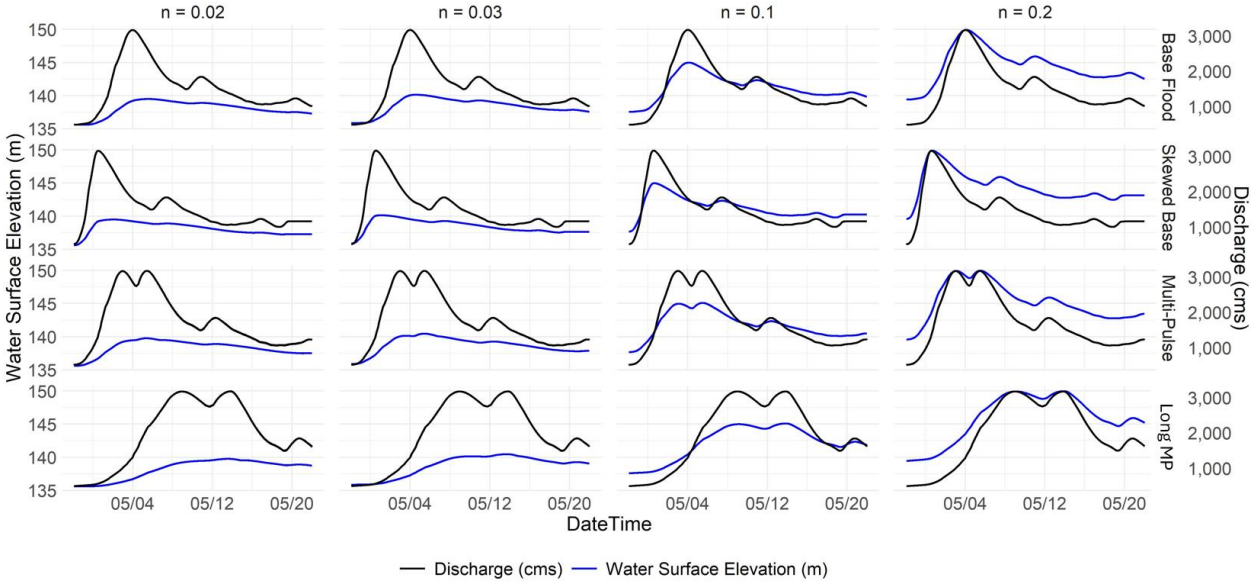

Figure 11: Flow and stage hydrographs for the roughness-hydrograph shape permutations.

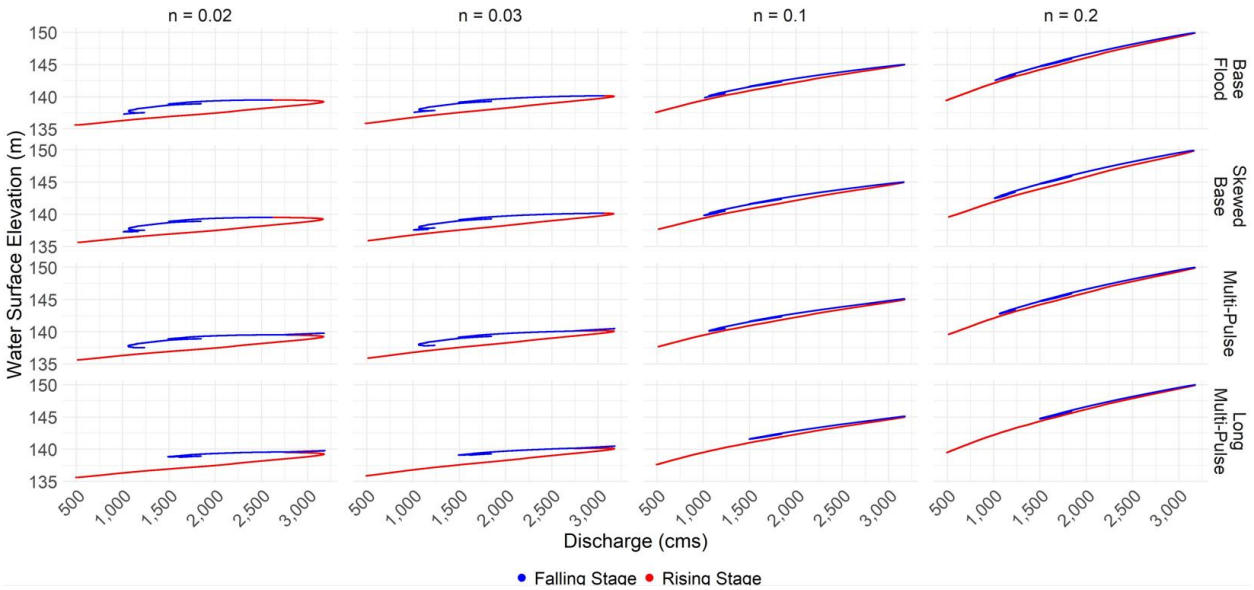

Figure 12: Stage-discharge loop rating curves for the roughness-hydrograph shape permutations.

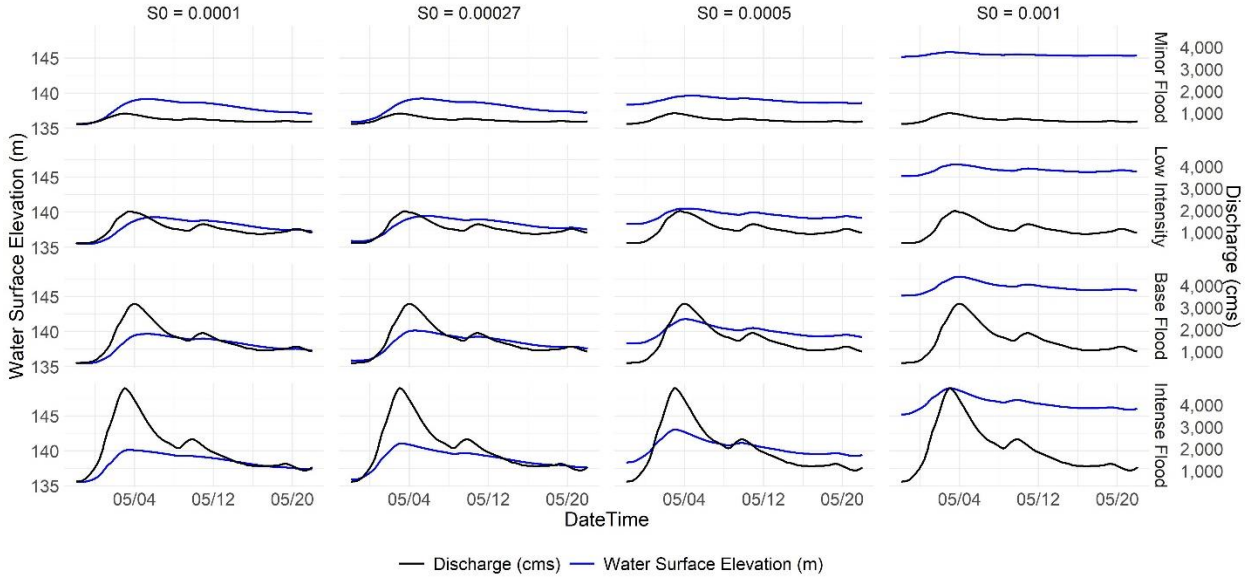

Figure 13: Flow and stage hydrographs for the bed slope-event intensities permutations.

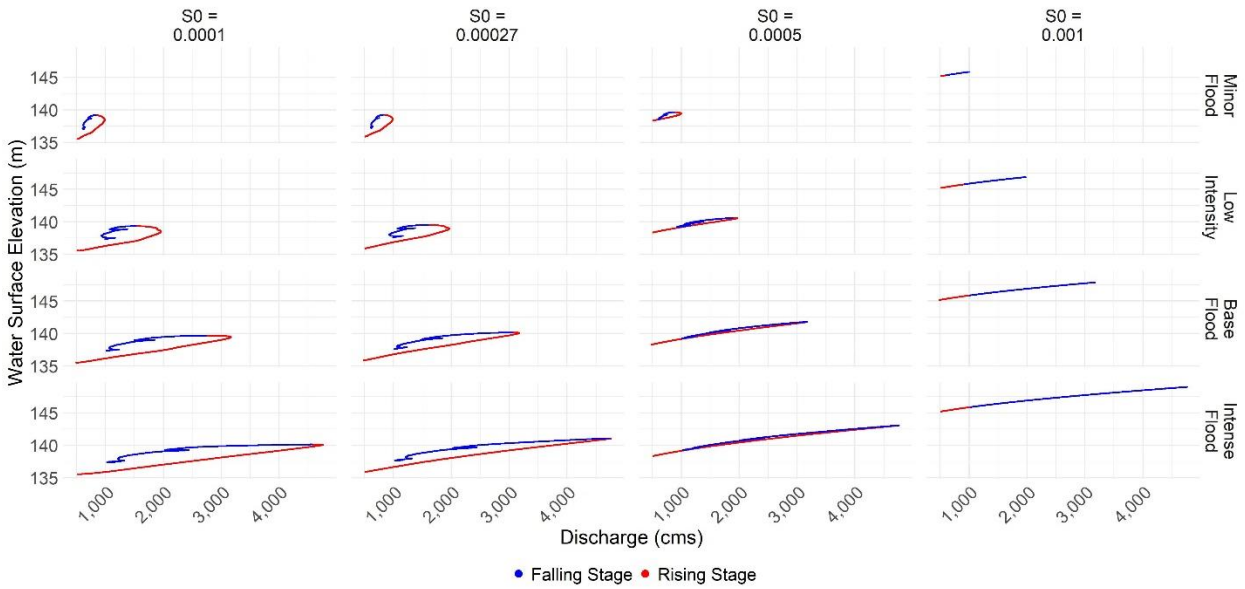

Figure 14: Stage-discharge loop rating curves for the bed slope-event intensities permutations.

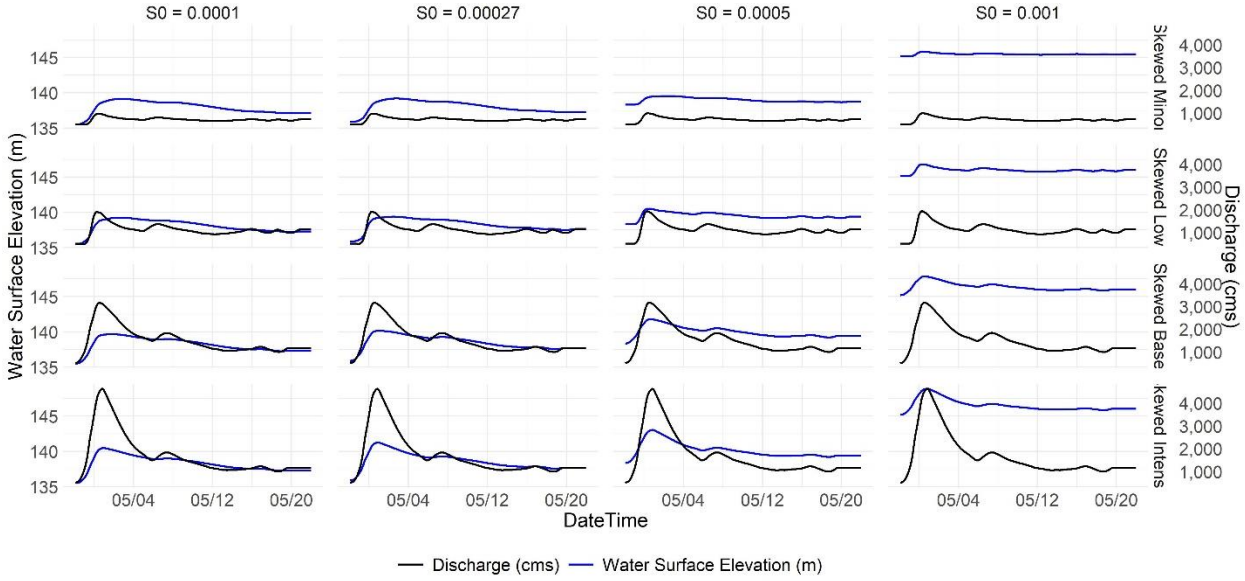

Figure 15: Flow and stage hydrographs for the bed slope-skewed event intensities permutations.

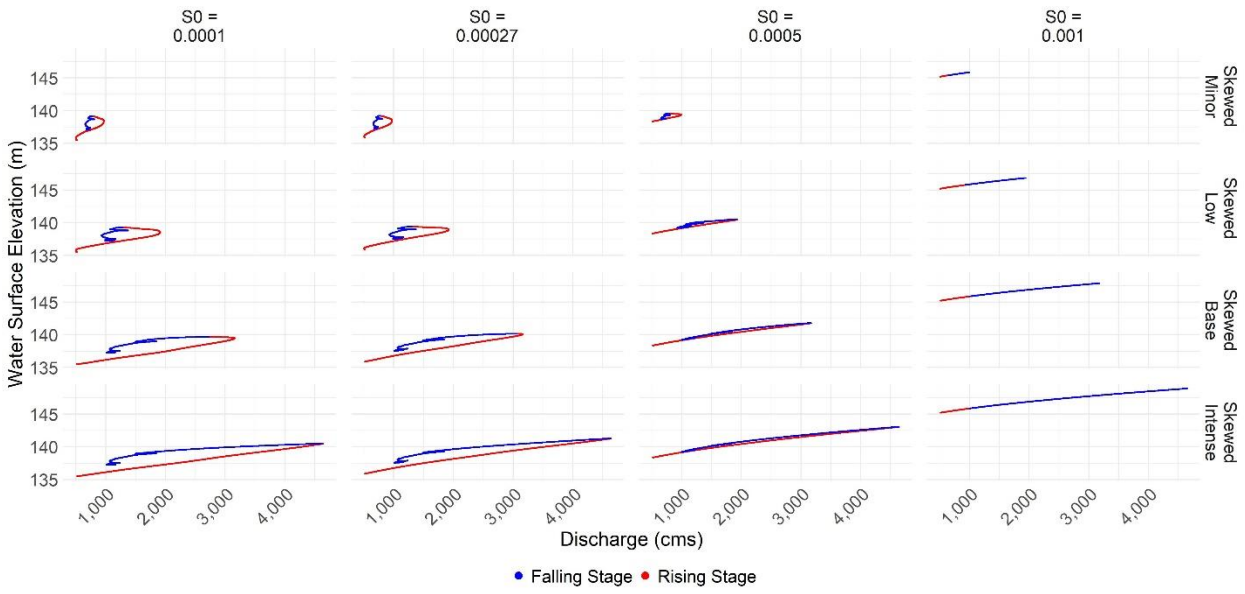

Figure 16: Stage-discharge loop rating curves for the bed slope -skewed event intensities permutations.

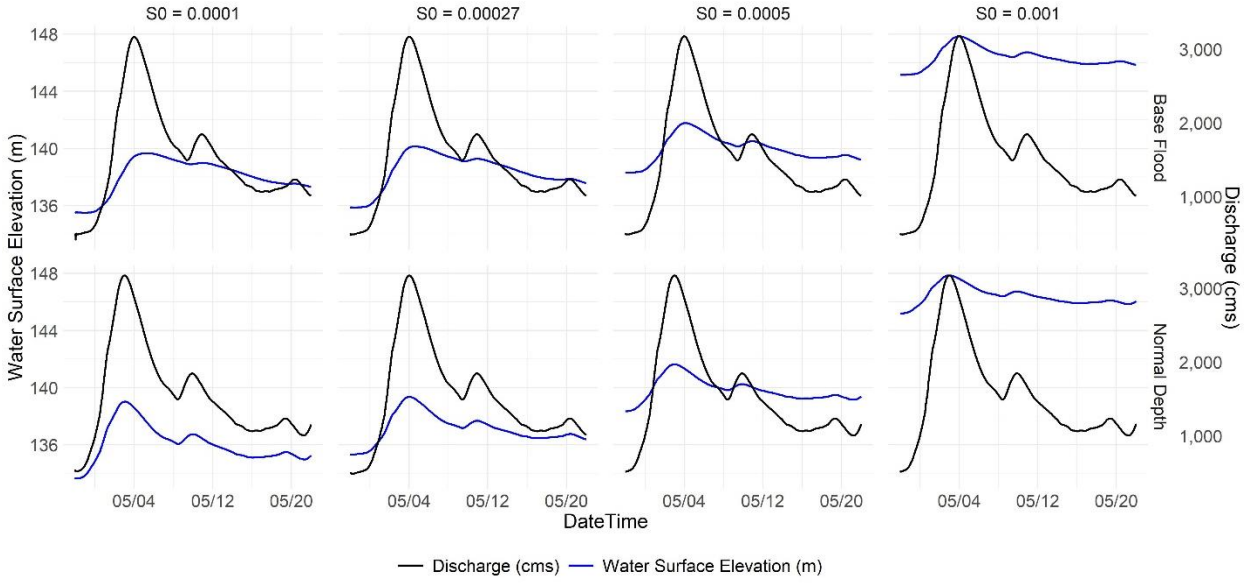

Figure 17: Flow and stage hydrographs for the bed slope -normal depth permutations.

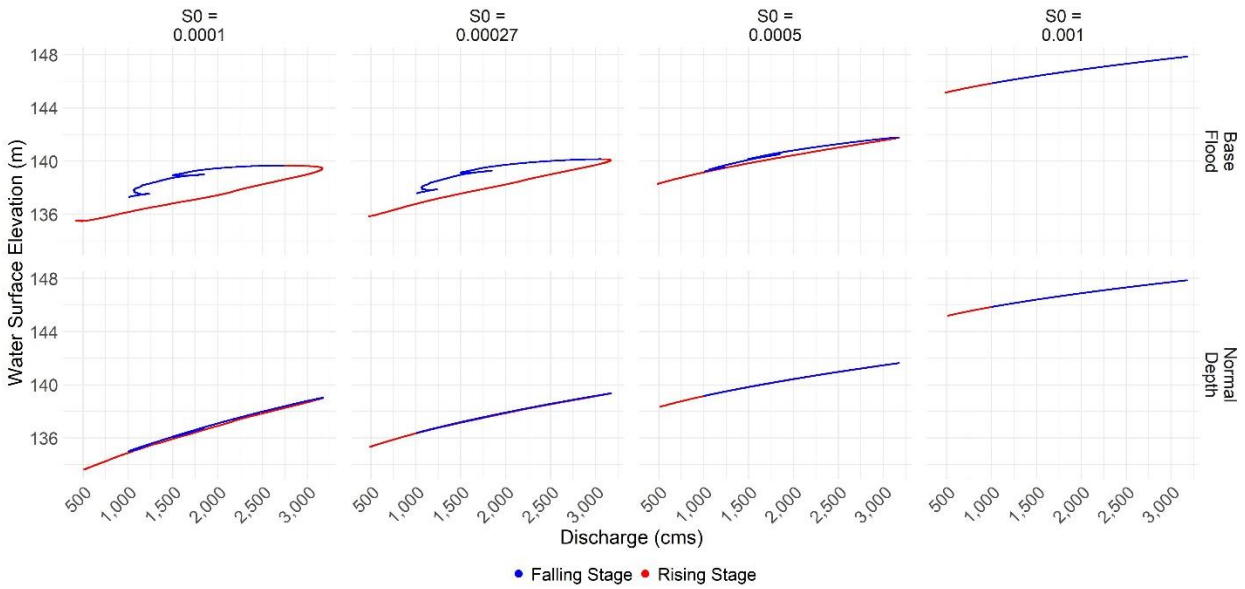

Figure 18: Stage-discharge loop rating curves for the bed slope -normal depth permutations.

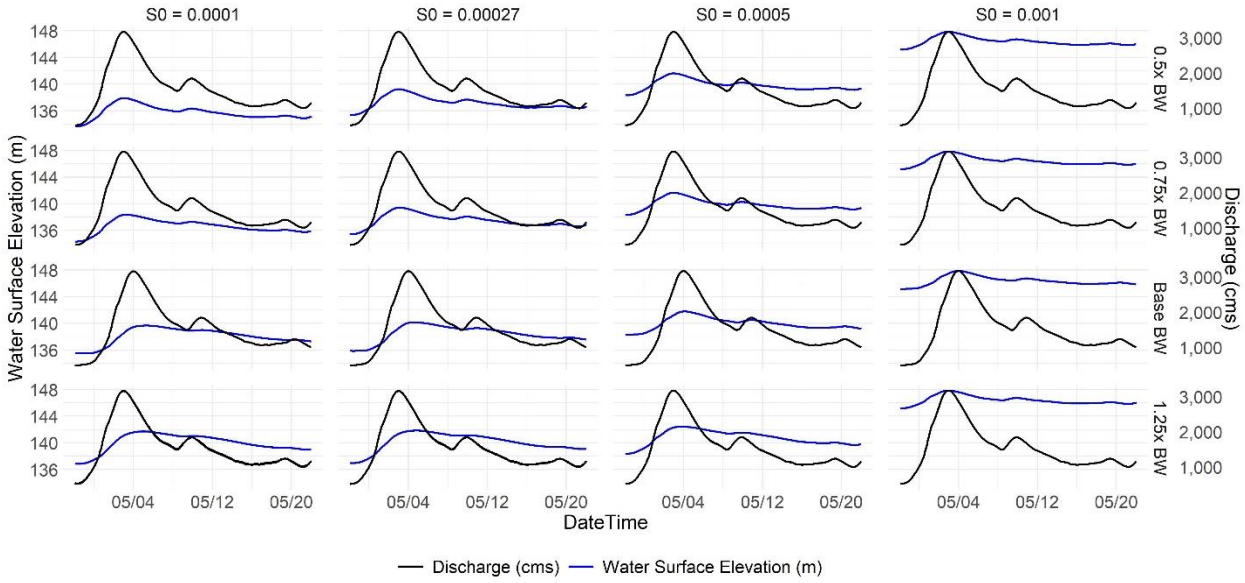

Figure 19: Flow and stage hydrographs for the bed slope -backwater permutations.

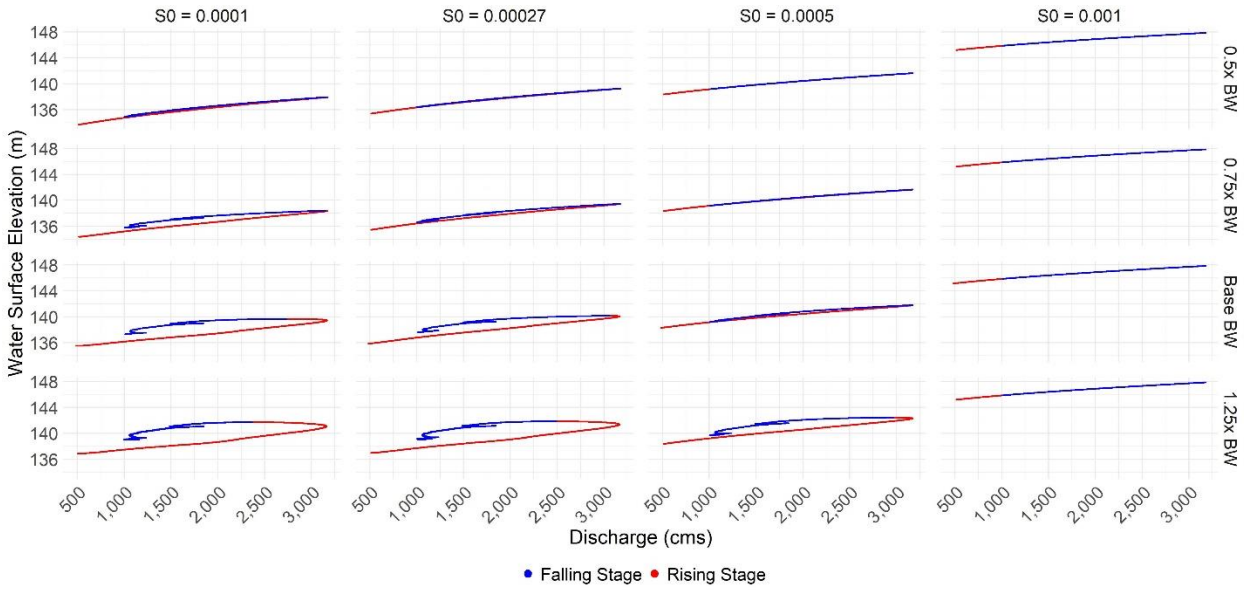

Figure 20: Stage-discharge loop rating curves for the bed slope -backwater permutations.

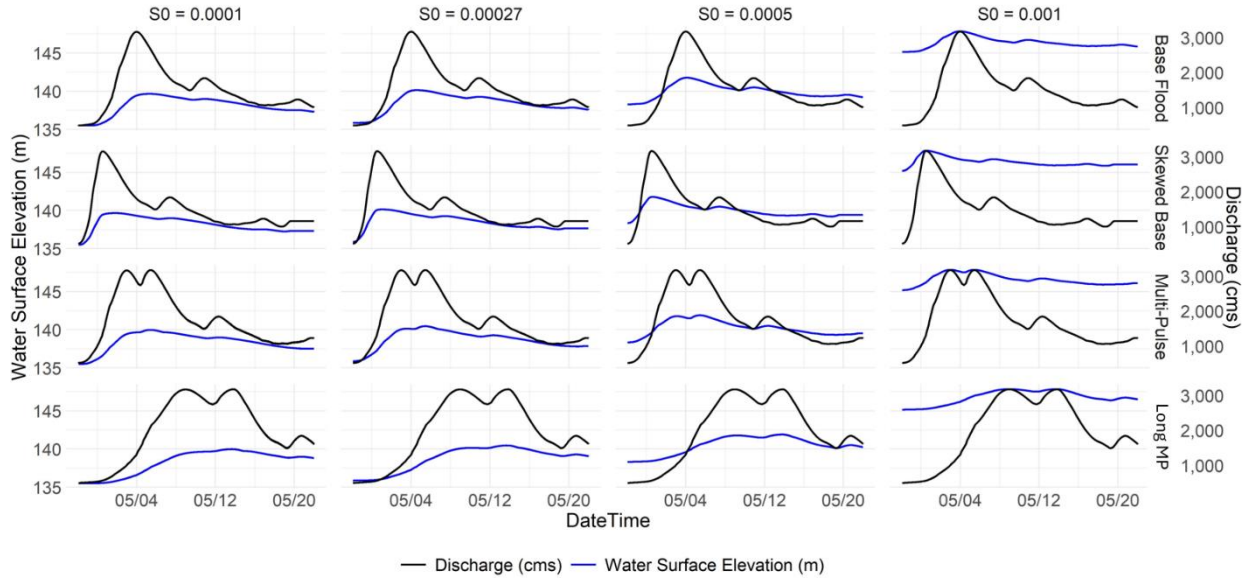

Figure 21: Flow and stage hydrographs for the bed slope -hydrograph shape permutations.

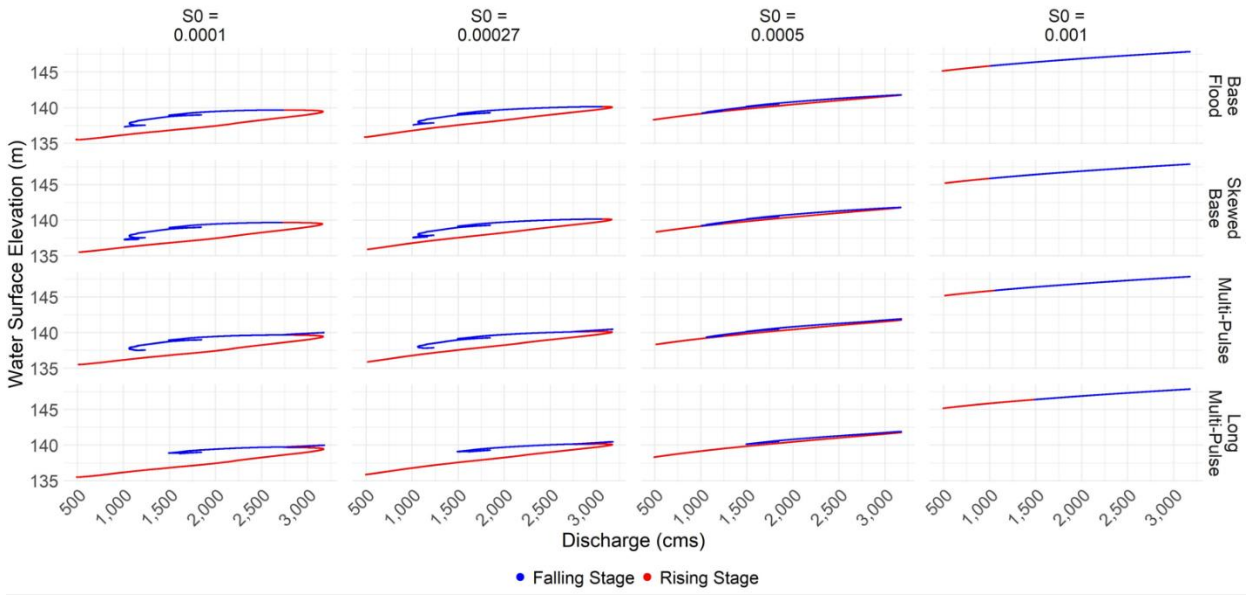

Figure 22: Stage-discharge loop rating curves for the bed slope -hydrograph shape permutations.

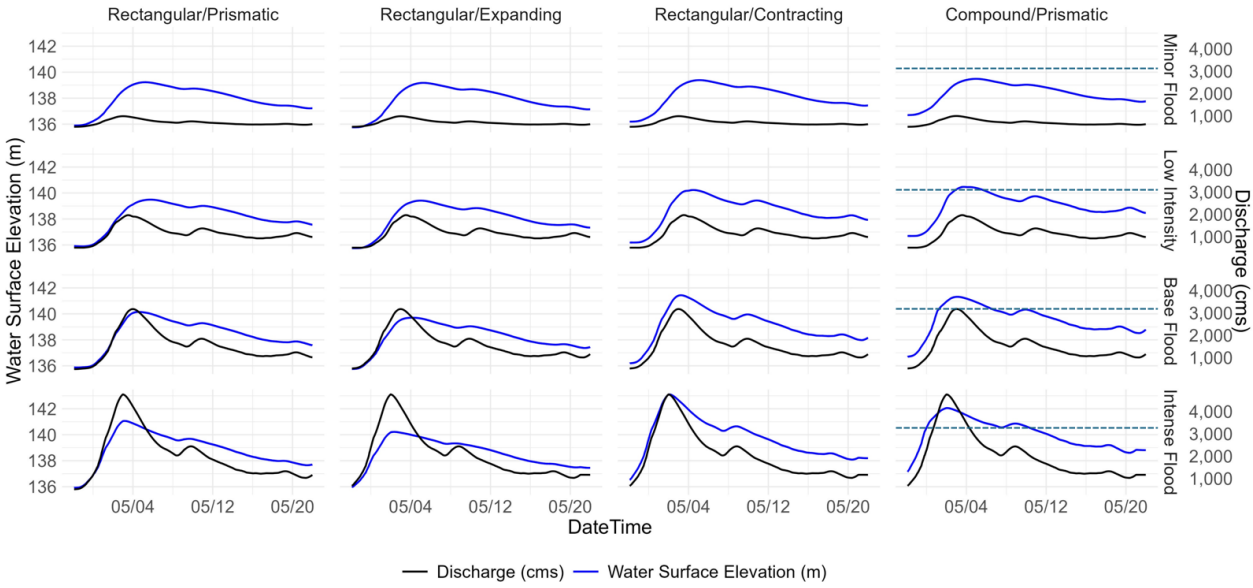

Figure 23: Flow and stage hydrographs for the channel shape-event intensities permutations.

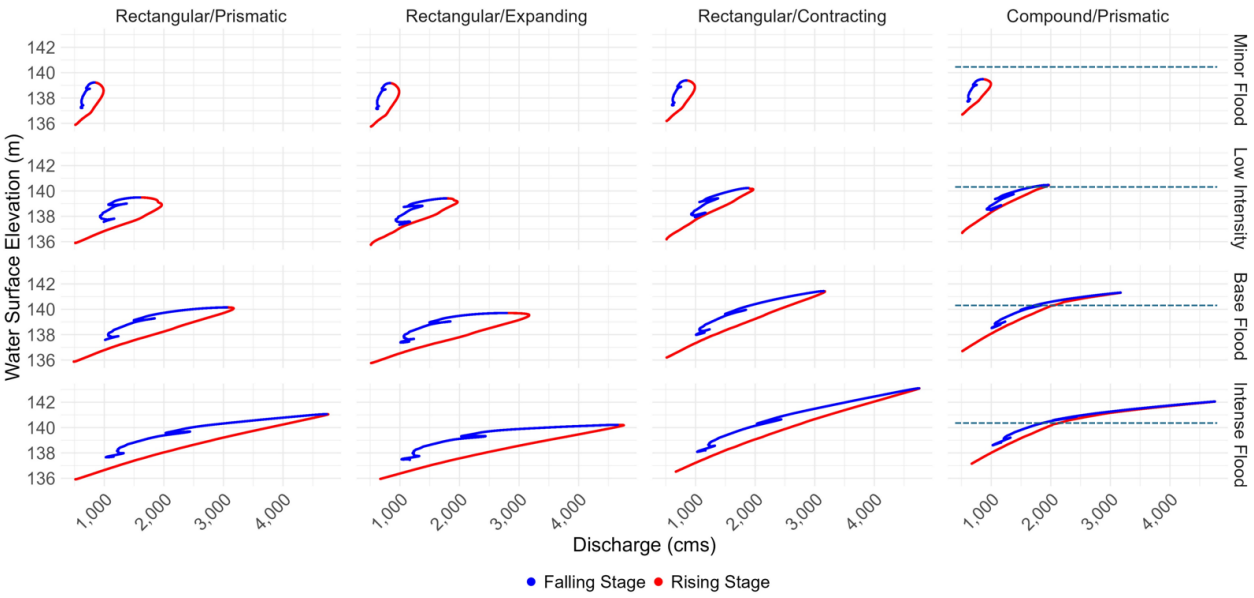

Figure 24: Stage-discharge loop rating curves for the channel shape -event intensities permutations.

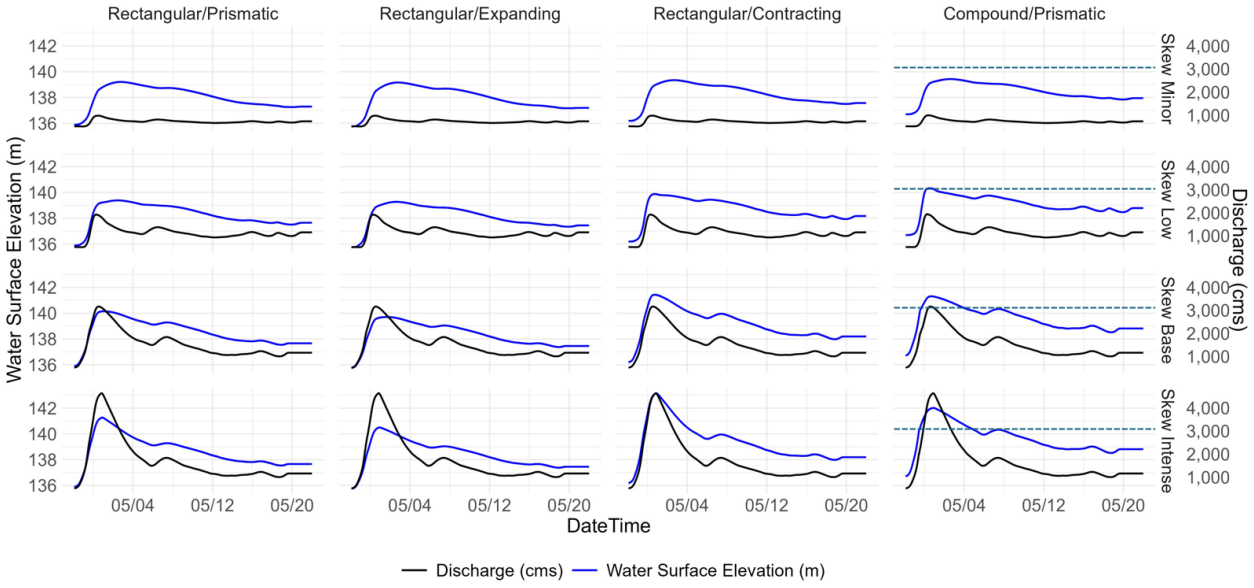

Figure 25: Flow and stage hydrographs for the channel shape -skewed event intensities permutations.

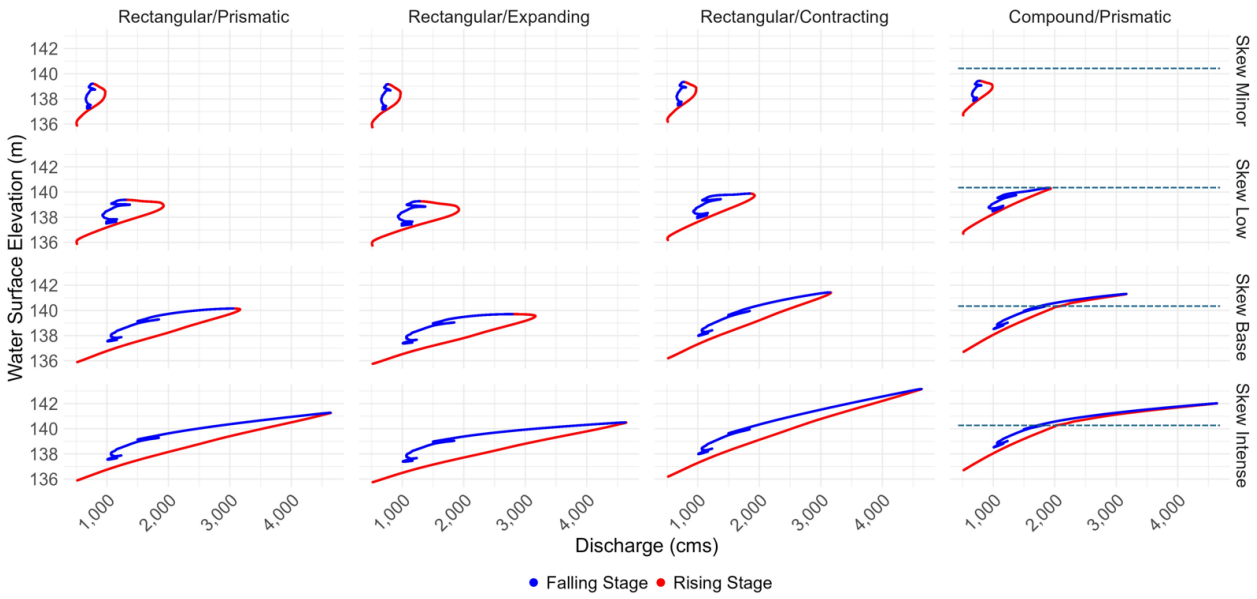

Figure 26: Stage-discharge loop rating curves for the channel shape -skewed event intensities permutations.

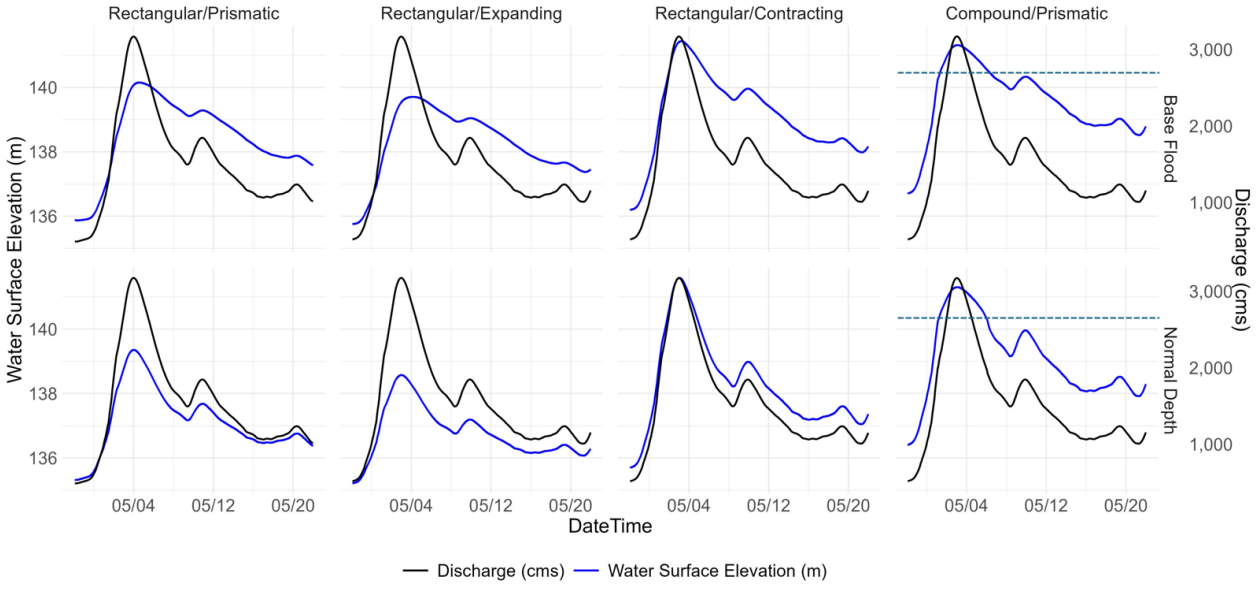

Figure 27: Flow and stage hydrographs for the channel shape -normal depth permutations.

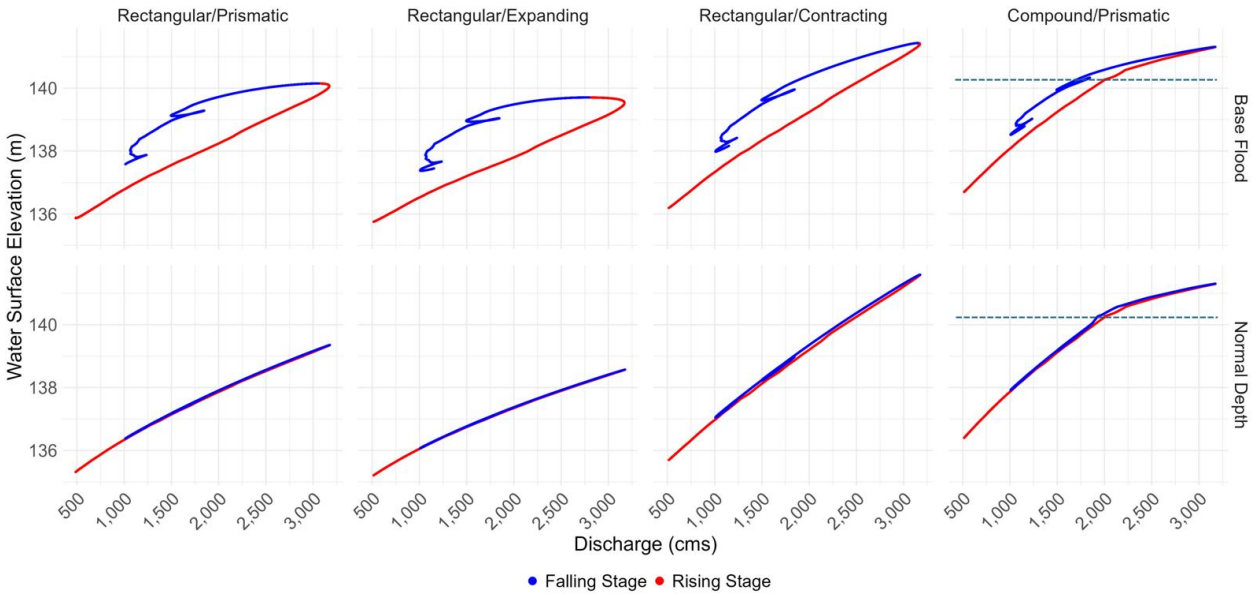

Figure 28: Stage-discharge loop rating curves for the channel shape -normal depth permutations.

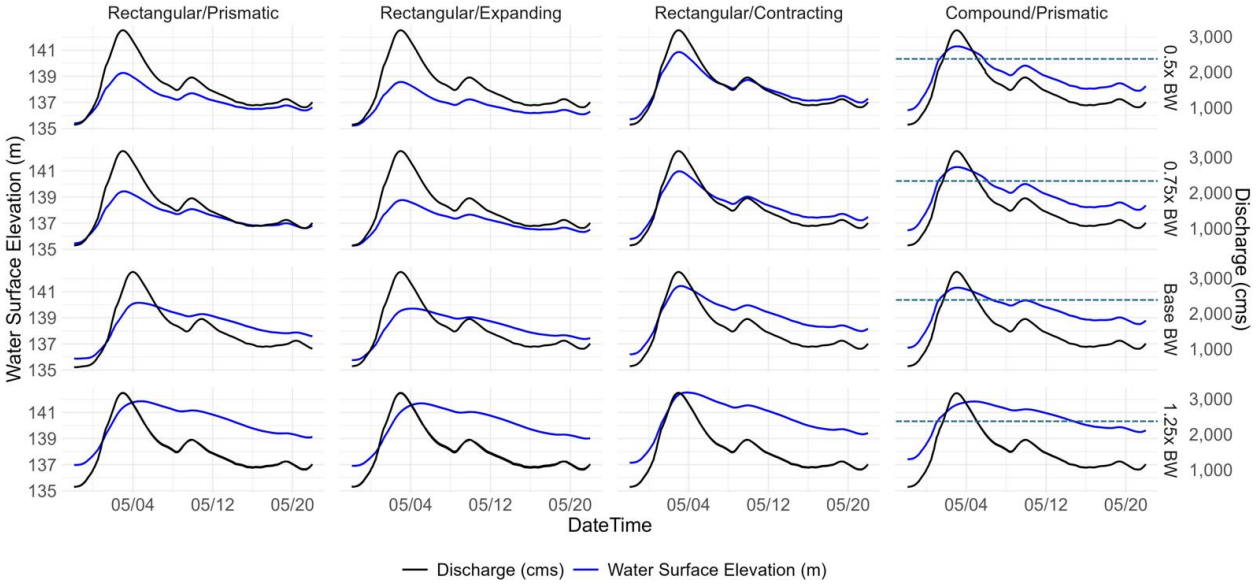

Figure 29: Flow and stage hydrographs for the channel shape -backwater permutations.

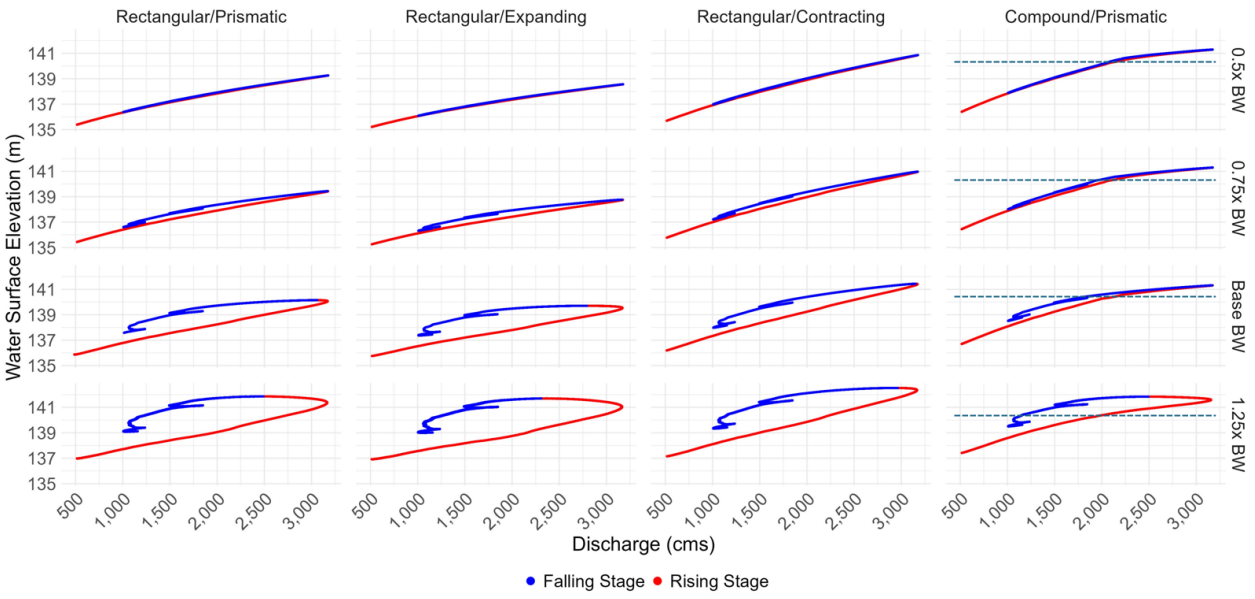

Figure 30: Stage-discharge loop rating curves for the channel shape -backwater permutations.

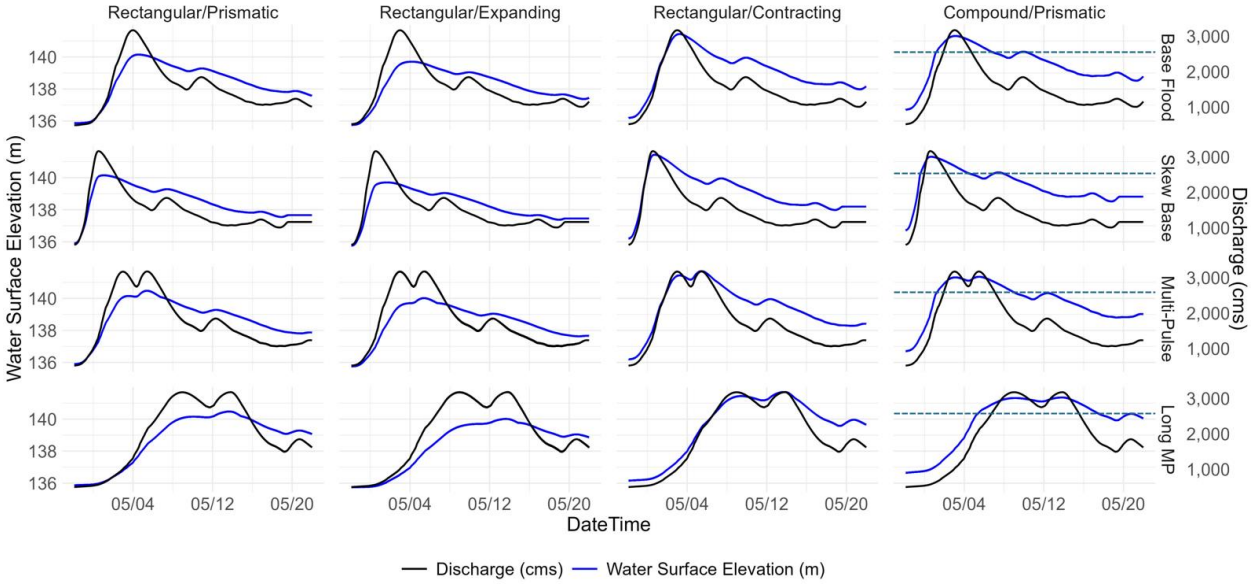

Figure 31: Flow and stage hydrographs for the channel shape -hydrograph shape permutations.

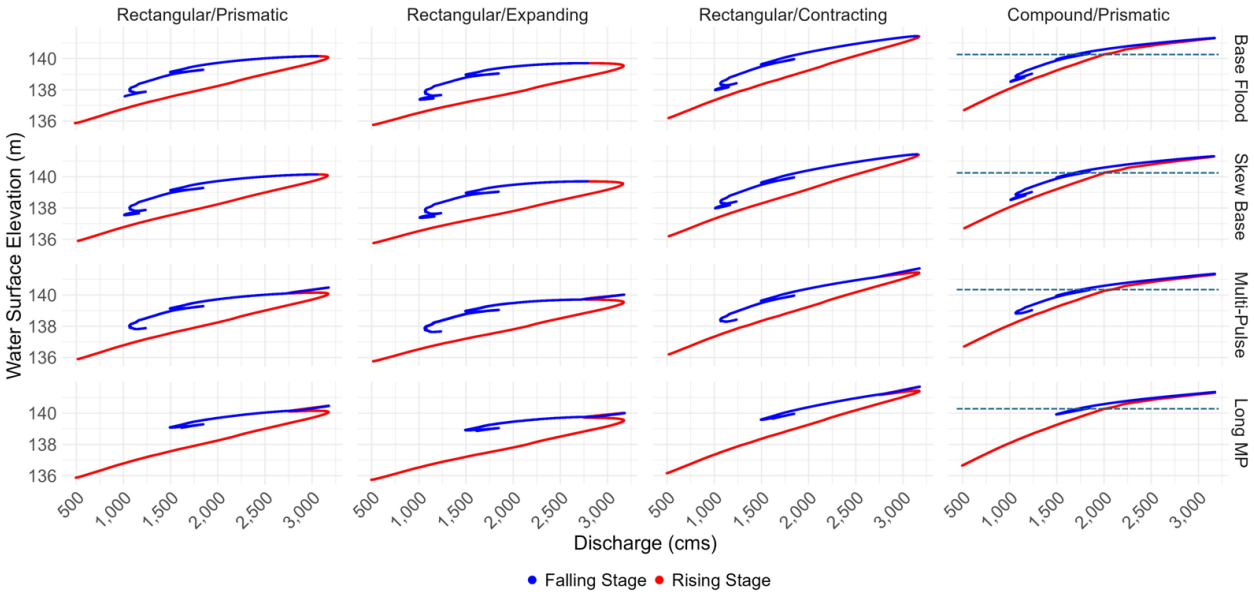

Figure 32: Stage-discharge loop rating curves for the channel shape -hydrograph shape permutations.

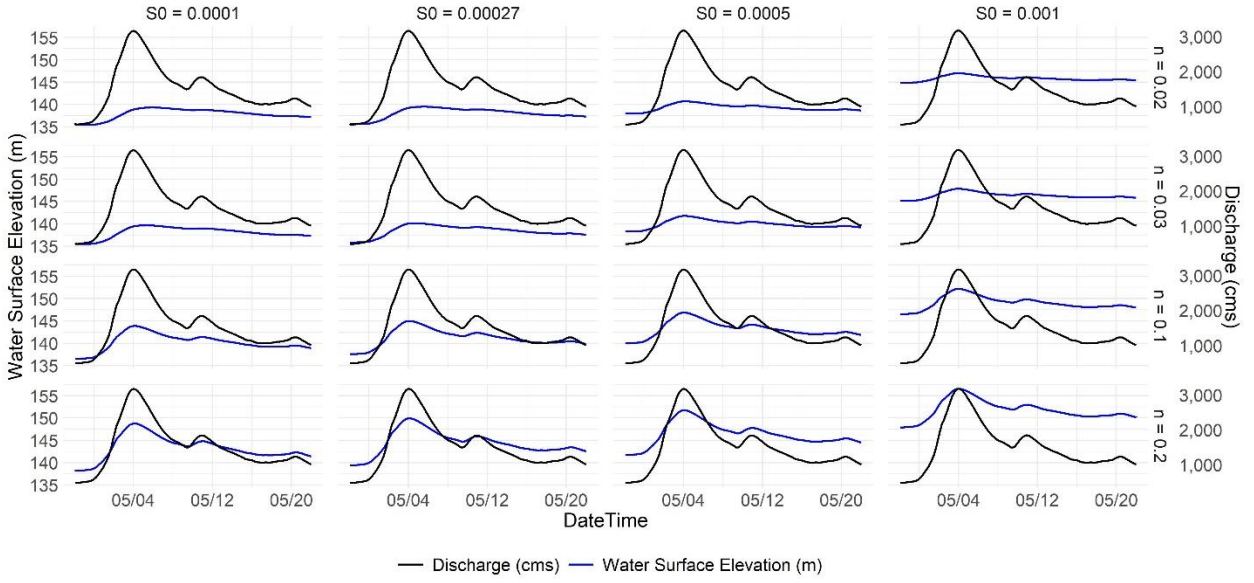

Figure 33: Flow and stage hydrographs for the bed slope-roughness permutations with the base event scenario.

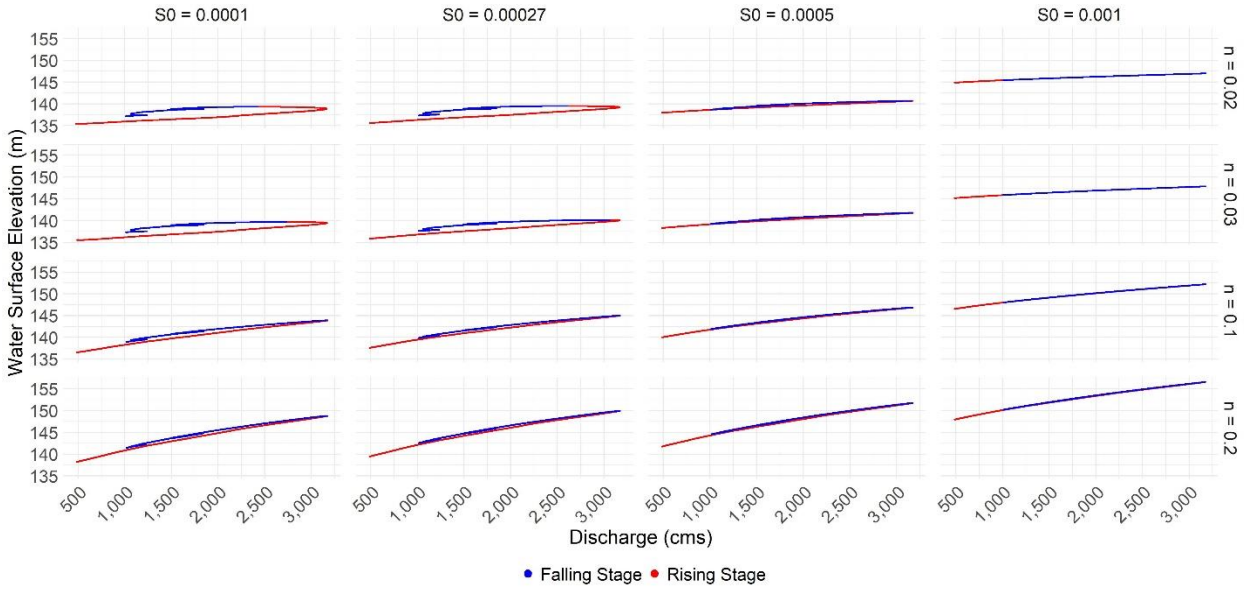

Figure 34: Stage-discharge loop rating curves for the bed slope-roughness permutations with the base event scenario.

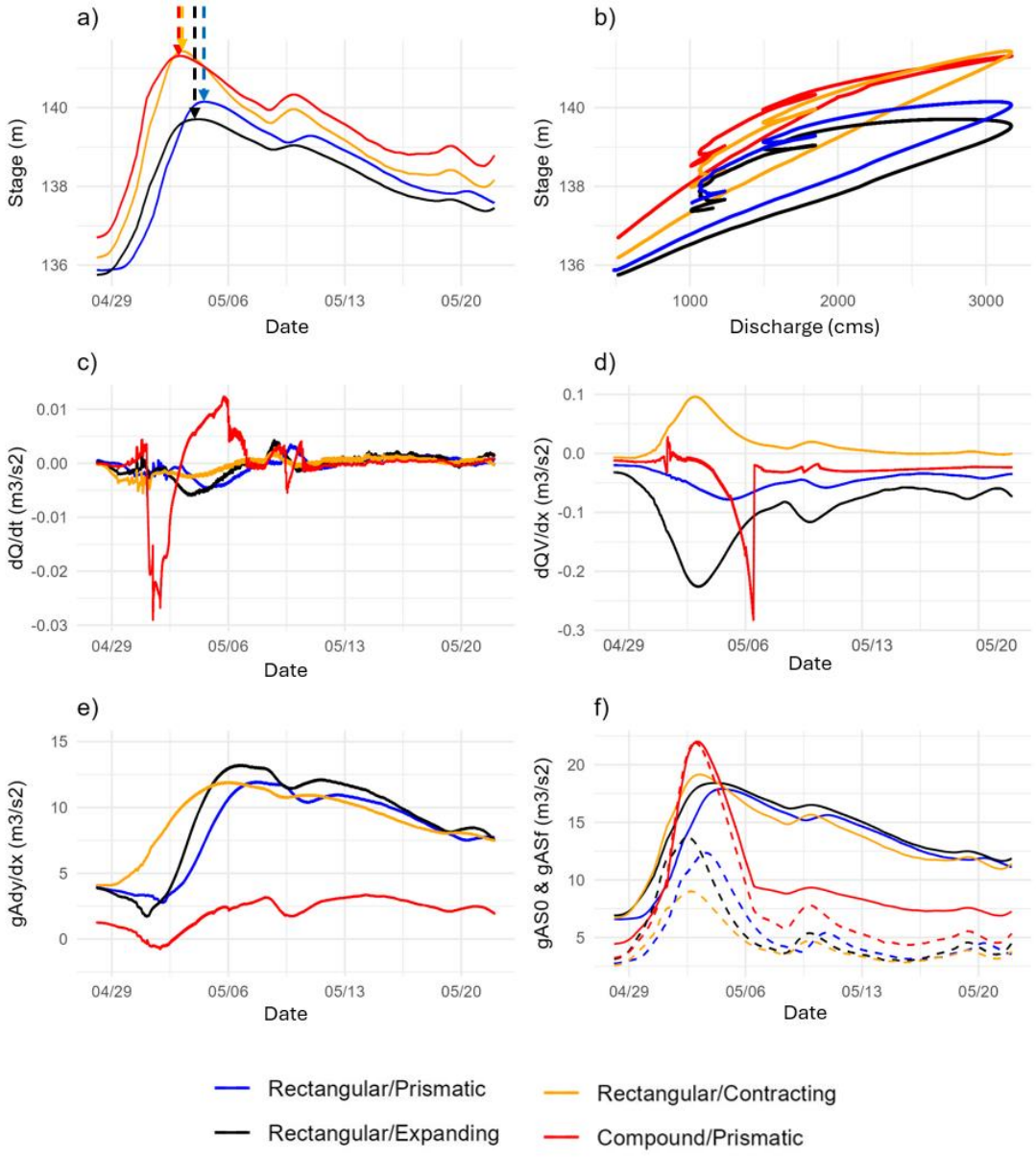

Figure 35: Gradient plots for varied channel shape permutations under base conditions for other parameters: a) stage hydrographs, b) stage-discharge rating curves, c) local acceleration term, d) convective acceleration, e) pressure gradient, and f) kinetic forces: gAS_0 shown with a solid line and gASf with a dashed line.